

**Development of a Cosmic Muon Trigger System  
for the Characterization of Tracking Detectors  
to be used in the the ATLAS Muon Detector Upgrade**

Wei Wu

Department of Physics

University of McGill, Montréal

June 2016

*A thesis submitted to McGill University in partial fulfillment  
of the requirements of the degree of  
Master of Science*

© Wei Wu 2016

## ABSTRACT

To better deal with the high instantaneous luminosity of the Large Hadron Collider at CERN and reduce the fake rate of muon events, the New Small Wheel detectors (NSW) will replace the present first stations in the forward regions of the Muon Spectrometer in ATLAS.

The ATLAS Canada group is involved in the manufacturing and testing of an important components of the NSW: the small-strip thin gap chambers (sTGC). One of the duties of McGill's ATLAS group is to complete the quality testing and performance assessment of the new sTGC units. To accomplish this task, a trigger system, a gas system, along with a slow control system and a data acquisition system, are built in our lab of McGill University. This Master's project focuses on the trigger system. It records the work done to maximize the efficiency of the trigger system in detecting cosmic muon events and to further our understanding of the performance of the trigger system via simulations.

## ABSTRAIT

Afin de mieux gérer la luminosité instantanée élevée du Grand Collisionneur de Hadrons au CERN et réduire le taux de faux événements muoniques, les détecteurs «New Small Wheel» (NSW) vont remplacer les actuelles premières stations dans les régions avant du spectromètre à muons d'ATLAS. Le groupe ATLAS Canada est impliqué dans la fabrication et les tests d'une composante importante du NSW : les «small strip thin gap chambers» (sTGC). Une des responsabilités du groupe ATLAS de McGill est de compléter les tests de qualité et des évaluations de performance pour les nouvelles unités sTGC. Pour accomplir cette tâche, un système de déclencheurs ainsi que des systèmes de gaz, de contrôle lent et d'acquisition de données sont construits dans notre laboratoire de l'Université McGill. Ce projet de maîtrise se concentre sur le système de déclencheurs. Il contient le travail effectué pour maximiser l'efficacité du système dans la détection de muons cosmiques et pour approfondir notre connaissance de la performance du système à l'aide de simulations.

## ACKNOWLEDGEMENTS

I would like to thank my supervisor, Dr. François Corriveau. This thesis would be nothing without his support and guidance. He is always so patient with all my silly questions during my degree. His deep understanding of experimental high energy physics helps lead me in the right direction whenever I feel confused. He has taught me how to think, how to ask the right questions, and how to make good assumptions as a researcher. He used to always say to me, "Wei, don't say 'I will try it', say 'I will do it'". I became more persistent and determined on the journey to a Master's degree under his supervision.

Also, I would like to thank everyone in my group: Prof. Brigitte Vachon, Prof. Steven Robertson, Prof. Andreas Warburton, Dr. Andr  e Robichaud-V  ronneau, Dr. Camille B  langer-Champagne, Robert Keyes, Kuhan Wang, Benoit Lefebvre, F  lix L  ger, L  vis Pepin, and many others. Everyone in the ATLAS group at McGill was enthusiastic in offering me help whenever I needed it. At the same time, they were all very professional, so I learned a lot from each of them. Similarly, I would like to thank one of our summer student, Lukas Adamek. The simulation used in Chapter 5 was based in part on code written by him in Python to solve the time difference.

Thanks also to Karuna Warriar, David Luong (he is the best!), and Ian Lam for reading through earlier drafts of this thesis, making suggestions, and correcting my grammar.

I must thank all my friends who are outside of McGill ATLAS group, who always encourage me whenever I feel confused. I especially thank Lisa Wu and Juno Ye, who always traveled from Toronto to Montreal to visit me during the past two years.

Last but most importantly, I must thank my parents. They have always been extremely supportive of me every day of my life. Though they live far from Canada and don't know too much about physics, they give me care and comfort whenever I need it. Thank you, my great Mom and Dad. “谁言寸草心 报得三春晖？”

---

# Contents

---

<b>1</b>	<b>Introduction</b>	<b>9</b>
1.1	The Standard Model . . . . .	9
1.2	CERN . . . . .	11
1.3	LHC . . . . .	12
<b>2</b>	<b>The Detector</b>	<b>15</b>
2.1	Detectors at the LHC . . . . .	15
2.2	ATLAS Detector . . . . .	17
2.3	Muon Spectrometer . . . . .	21
2.4	New Small Wheel Upgrade Project . . . . .	24
<b>3</b>	<b>Lab at McGill University</b>	<b>27</b>
3.1	Cosmic Muons . . . . .	27
3.2	McGill sTGC Lab . . . . .	28
3.3	The Trigger System . . . . .	29
3.3.1	PMTs and scintillators . . . . .	29
3.3.2	Electronics . . . . .	34
<b>4</b>	<b>Data Taking and Results</b>	<b>37</b>
4.1	PMT Performance Test . . . . .	37
4.2	High Voltage and Signal Threshold Voltage Measurements . . . . .	43
4.2.1	High voltage and threshold voltage measurement for PMT A and B . . . . .	44

4.2.2	High voltage and signal threshold voltage measurement for PMTs on the large scintillators . . . . .	47
4.2.3	Summary . . . . .	50
4.3	Scintillator Efficiency Measurements . . . . .	51
4.3.1	Efficiency vs. HV and signal threshold voltage measurements . . . . .	51
4.3.2	Efficiency vs. position measurements . . . . .	53
4.3.3	Efficiency vs. recording time measurement . . . . .	59
4.4	Time Difference Measurements . . . . .	60
<b>5</b>	<b>Crosstalk Measurements</b>	<b>63</b>
5.1	The Observation of Triple Coincidences . . . . .	63
5.2	Calculation of Number of Double Muons Events . . . . .	64
5.3	Crosstalk Measurement . . . . .	67
5.3.1	Method one: wire position . . . . .	67
5.3.2	Method two: HV on/off . . . . .	69
5.3.3	Method three: amplitude correlation study . . . . .	70
5.3.4	Method four: quadruple coincidence/triple coincidence . . . . .	72
5.3.5	Conclusion . . . . .	74
5.4	Potential Sources of Triple Coincidences . . . . .	75
<b>6</b>	<b>Simulation</b>	<b>77</b>
<b>7</b>	<b>Summary and Conclusion</b>	<b>83</b>
<b>A</b>	<b>Additional plots</b>	<b>87</b>
A.1	The HV curve and signal threshold voltage curve for PMT A and B . . . . .	87
A.2	The HV curve for all PMTs . . . . .	91
A.3	The signal threshold voltage curve for all PMTs. . . . .	94
A.4	Table for the HV setting up using LeCroy . . . . .	97
A.5	The efficiency vs. position measurements for NTWO. . . . .	98
<b>B</b>	<b>Calculation</b>	<b>99</b>

B.1 The calculation of uncertainty of the efficiency . . . . . 99

**Bibliography** . . . . . **101**



## Chapter 1

---

# Introduction

---

## 1.1 The Standard Model

The study of physics is the study of matter and the interactions that take place with matter. Since the "all is number" theory of the ancient Greek Pythagoras or the *qi* theory of Wang Chong in Han Dynasty (27-97 AD) [1] from ancient China, physicists have never stopped exploring the structure of matter.

Since the 6<sup>th</sup> century BC, philosophers like Democritus, Epicurus and Leucippus produced an embryonic form of the theory of atomism, which states that all matter is made of extremely small particles called atoms. In 1802, John Dalton transformed the idea into a scientific theory, known as the atomic theory, by using it to explain his experimental observations [2]. In 1897, Joseph John Thomson found that these atoms have substructure. From then on, more and more particles were found, and physicists tried to develop a theory to organize all the particles in a similar way to the periodic table of the elements. Physicists also studied the interactions between the particles. In 1961, Sheldon Glashow combined the electromagnetic and weak interactions into one interaction called the GSW model [3]. In 1967, the Higgs mechanism was introduced into Glashow's electroweak interaction by Peter Higgs [4]. In the early 1970, quantum chromodynamics (QCD) is developed by David Politzer, Frank Wilczek and David Gross to describe strong interactions between quarks and gluons [5].

All this work culminated in the development of the Standard Model in 1980. The Standard Model is a theory which describes all known particles and their interactions (except gravity). In the Standard Model, particles are divided into two classes: fermions and bosons. Fermions have half-integer spin while bosons have integer spin. All matter is formed from elementary fermions, which include three leptons (electron, muon and tau), their corresponding neutrinos, and six quarks (up, down, charm,

strange, top and bottom; bottom quarks are also called beauty quarks). All elementary fermions have spin 1/2. The structure of the Standard Model is shown in Fig 1.1.

Particles interact with each other through four different forces: the electromagnetic force, the weak force, the strong force, and gravity. Four elementary bosons, also known as gauge bosons, carry those four forces. Photons mediate the electromagnetic interaction between charged particles, while W and Z bosons mediate the weak interaction (which affects all particles). Gluons mediate the strong interaction between quarks. The force of gravity is hypothesized to be mediated by gravitons, but these have not been detected yet, meanwhile the energy scale of gravity is different by orders of magnitude from that of the other forces. Therefore, gravity is not included in the Standard Model. The mathematical foundation of the Standard Model is gauge theory. However, particles in gauge theory do not have mass, which is inconsistent with reality. To solve this contradiction, the Higgs mechanism

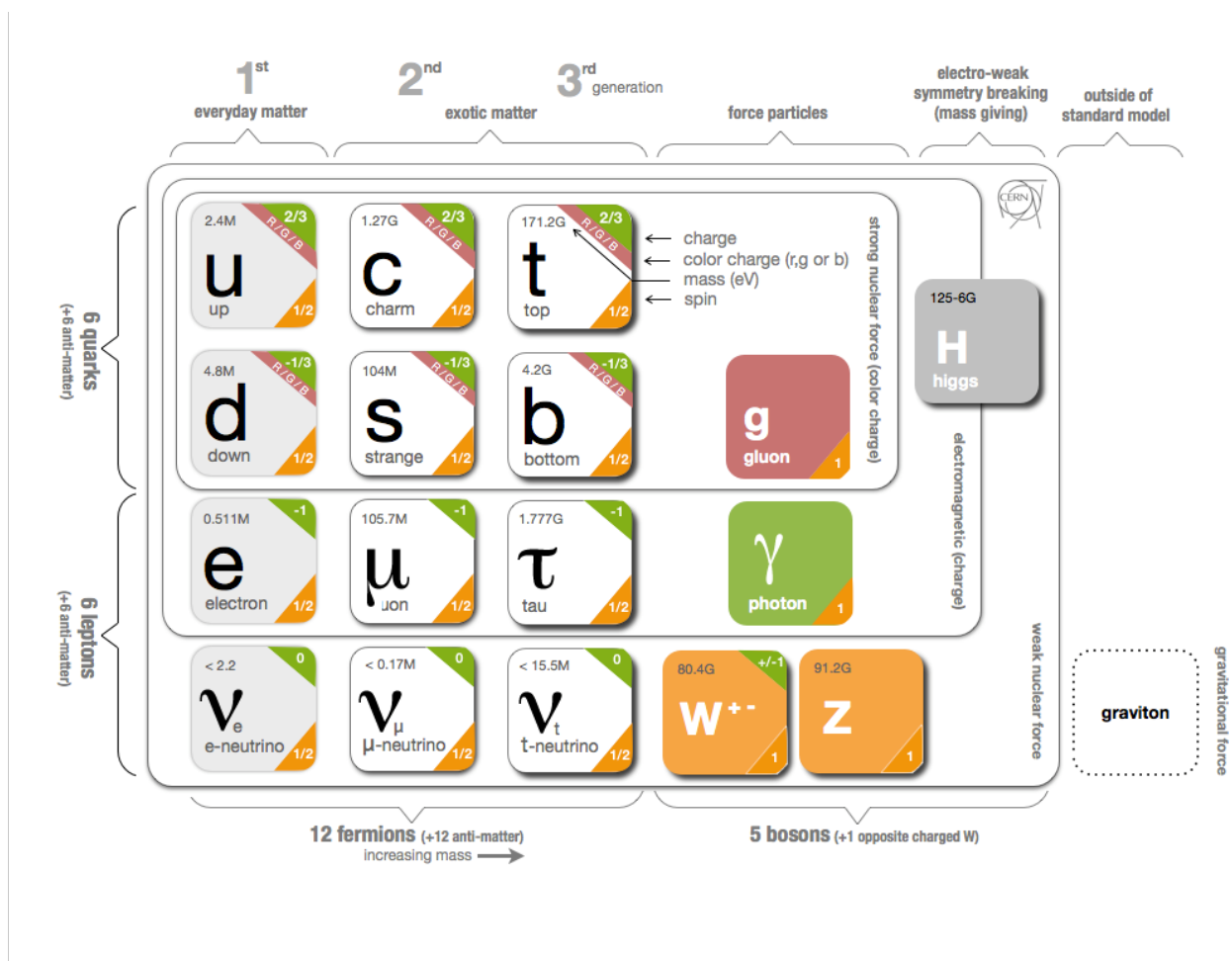


Figure 1.1: Six quarks, six leptons and five bosons, as elementary particles in the Standard Model, are introduced along with the information about their charges, color charges, masses, spins and the forces they interact with (taken from [6]).

introduces spontaneous symmetry breaking into gauge theory to provide mass. The Higgs mechanism also predicts an elementary boson called the Higgs boson [4].

The Standard Model fits most experimental results very well. For instance, we have discovered the W boson, the Z boson, gluons, and even the Higgs boson. However, there are still some questions that remain to be solved. For instance:

1. How do we include gravity and dark matter into the Standard Model?
2. Do the "elementary" particles have their own substructure?
3. What do the laws of physics look like in the early universe? Research on the quark-gluon plasma can help us understand the early universe better.
4. Why is there more matter than antimatter nowadays, though theorists predict that there should be equal amounts of matter and antimatter produced in the Big Bang?
5. The hierarchy problem: why is gravitation much weaker than other forces?
6. Are there only three generations of quarks and leptons?

The Standard Model is not a self-consistent theory yet. We still have a long way to go in order to find the theory of everything. Physicists have been working on theories such as supersymmetry, quantum gravity, and extra dimensions to solve these open questions in the Standard Model. Actual experimental results will show us the right direction to follow. Some elementary particles described in the Standard Model cannot exist by themselves under ordinary conditions, such as quarks. Therefore, it was necessary to build a large collider, such as the Large Hadron Collider, to create an extremely high energy environment, so we are able to better probe the Standard Model, and even theories of physics beyond the Standard Model.

## 1.2 CERN

The European Organization for Nuclear Research (CERN) is an organization that runs the largest particle physics laboratory in the world. It was established on September 29, 1954 in the northwest part of Geneva on the Franco-Swiss border. It has 21 member states with 2,523 staff and 13,142

fellows, associates, students, users, and apprentices of 113 nationalities, coming from 608 institutes and universities [7]. When CERN was first established, research on the structure of matter was on the level of the nucleus. Nowadays, we understand that nuclei have substructure. The main goal of CERN today is to understand the Standard Model. More precisely, it is to perform research on particles and the interactions between them. To achieve this goal, the Large Hadron Collider (LHC) was built underground at CERN.

## 1.3 LHC

The LHC is the largest and the most powerful particle accelerator in the world. From 1984 to 2008, scientists and technicians from over hundred countries working at CERN collaborated to build it. The LHC, contained in a tunnel whose circumference is 27 km, is located around the French-Swiss border near Geneva, Switzerland. Inside the tunnel, there are two adjacent parallel beamlines in ultrahigh vacuum. The beamlines contain protons, and they collide at extremely high energies. The proton bunches are restrained in a strong magnetic field produced by superconducting magnets. Liquid helium at 1.9 K is used to prevent the whole system from overheating as this may cause magnet quench [8]. In addition, in order to maximize the chances of the collision of two beams at the four intersection points, a total of 1,232 dipole magnets and 392 quadrupole magnets have been installed near those points to focus the beams in the nominal interaction regions [9, 10].

The LHC was planned to begin operations on September 10, 2008, but the first run was delayed from 2008 to 2009 due to a leakage of liquid helium in Sectors 3 and 4 of the LHC. The center-of-mass energy started at 7 TeV with a luminosity of  $6 \times 10^{33} \text{ cm}^{-2} \text{ s}^{-1}$ , and reached at 8 TeV in the first run. The first shutdown was from 2013 to 2015. During the shutdown period, technicians and scientists maintained both the hardware and the software of the LHC. In July 2016, the second run began. The goal is to double the energy of the first run by starting at 13 TeV then reach 14 TeV and have a luminosity of  $1 \times 10^{34} \text{ cm}^{-2} \text{ s}^{-1}$ . After that, the LHC will undergo a long term shutdown from 2018 to 2021. After the long term shutdown, the third run will begin with highly increased luminosity [11, 12].

The LHC produces extremely high energy conditions similar to those of the Big Bang. Experiments performed there may help us to understand the origin of matter. The general goal of the LHC is to explore unknown areas of physics, such as the essence of the Higgs mechanism, color confinement,

dark matter, even new particles and symmetries.



Figure 1.2: The aerial view of CERN and the LHC with its main experiments (from M. Brie, 2008) [13].



## Chapter 2

# The Detector

## 2.1 Detectors at the LHC

Corresponding to the four intersection points in the beams, the LHC contains four particle detectors to record data. Three of them are CMS, ALICE, and LHCb. The fourth one, which is related to the subject of this thesis, is called ATLAS.

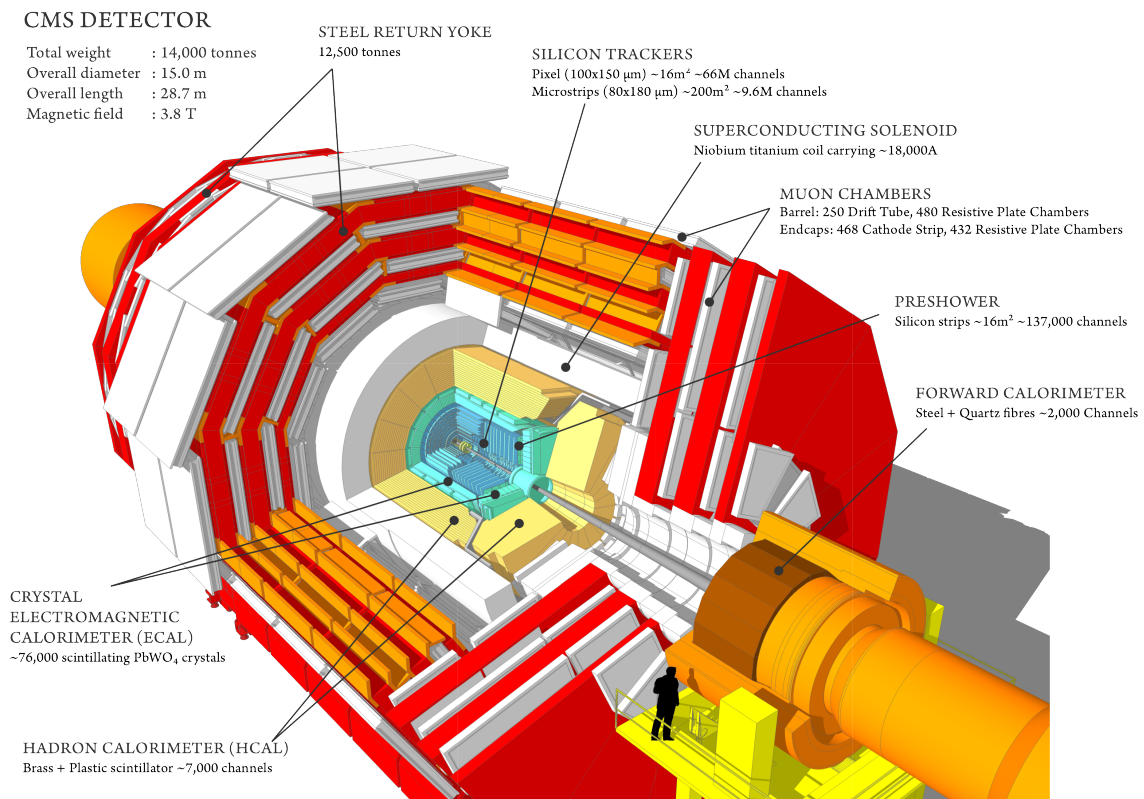


Figure 2.1: The Sectional View of the CMS Detector (from L. Taylor, 2011) [14]. The main components of the detector are identified.

The Compact Muon Solenoid (CMS) as ATLAS is a multifunctional detector which is shown in Figure 2.1. The goals of CMS range from the detailed search for the Higgs boson to physics beyond the Standard Model. The CMS has multiple layers, the innermost of which is a tracker made of silicon chips. It is surrounded by an electromagnetic calorimeter, which is used to measure the energy of electrons and photons. The outer layer is a sampling calorimeter which keeps hadrons from escaping from the detector. The CMS contains a solenoid that creates a magnetic field of 3.8 T which encircles the tracker and the calorimeter. The outermost layer is a large muon detector which is surrounded by the magnetic field of the solenoid. The overall diameter of the detector is 15.0 m and the overall length is 28.7 m. CMS is composed of fifteen sections which are all made on the ground and assembled in the cave afterwards [14, 15].

A Large Ion Collider Experiment (ALICE) is a heavy-ion detector. When Pb-Pb nuclei collide at a centre of mass energy more than 2.76 TeV per nucleon pair, a quark-gluon plasma may be created at very high energy densities and temperatures. In this state of matter, color confinement may be violated. ALICE is designed to study the strong interaction, which will contribute to a better understanding of QCD. ALICE consists of 18 subdetectors as shown in Figure 2.2. They measure the energy, the velocity and determine the identity of different particles [16, 17].

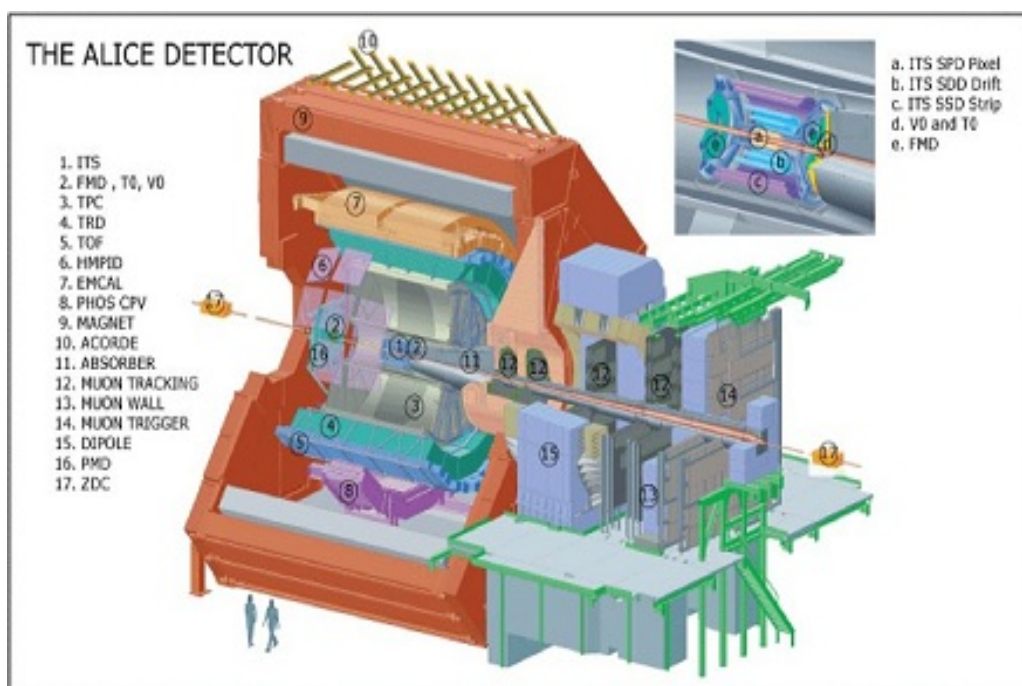


Figure 2.2: The View of the ALICE Detector (from LHCb Experiment, 2008) [18]. The sub units of the detector are shown in the figure.

A huge amount of B mesons, which contain beauty and anti-beauty quarks, are produced when particles collide in the LHC. The Large Hadron Collider beauty (LHCb) experiment aims to study the mass difference between the beauty and anti-beauty quarks. This may help explain CP violation. Decay products from the B mesons produced during collisions are emitted at a very small angle ( $\leq 10^\circ$ ) to the colliding proton beams. Therefore, unlike ATLAS or the CMS, the sub-detectors of the LHCb lie after each other within a 20 m longitudinally. The LHCb detector is shown in Figure 2.3 [19] [20].

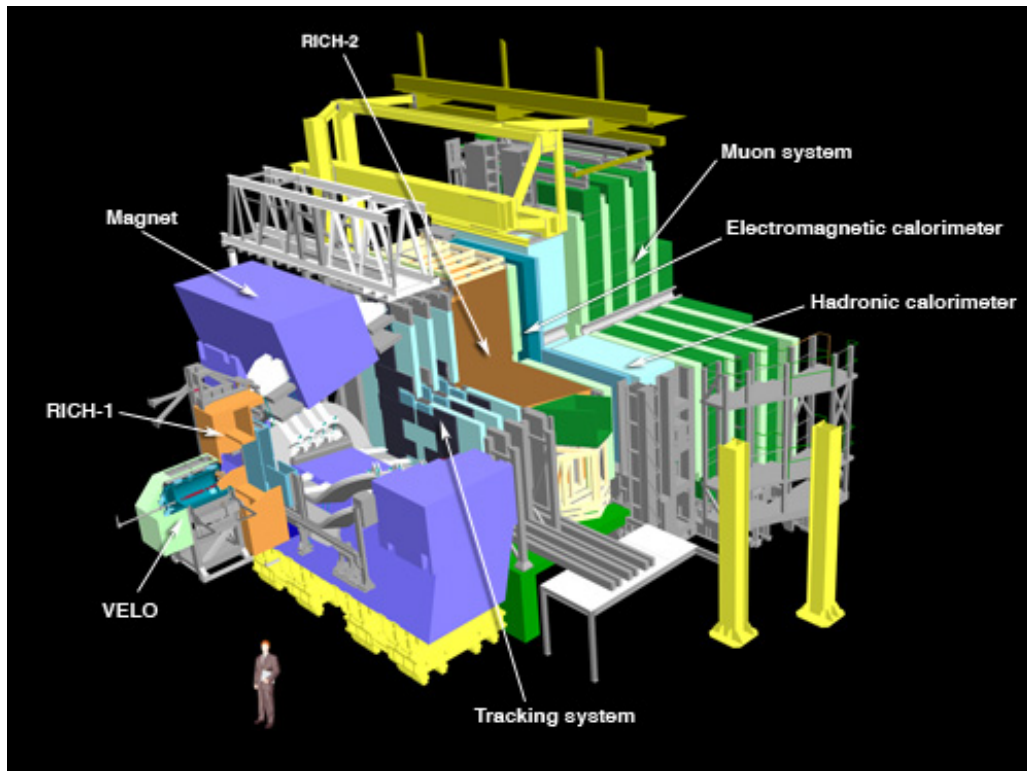


Figure 2.3: The View of the LHCb Detector (from LHCb Experiment, 2008) [21].

## 2.2 ATLAS Detector

A Toroidal LHC ApparatuS (ATLAS) (Figure 2.4) is one of four major detectors in the LHC and the one that this thesis will focus on. The main purpose of ATLAS is to provide high-precision data for any physical phenomenon observed in the high energy collisions at the LHC. One of its aims is to determine the parameters of the Standard Model, such as the mass of the Higgs boson, more precisely. Another aim is to discover new physics, such as new particles which have not been predicted in any theory. As the largest particle detector at CERN, ATLAS has a length of 46 m and diameter of 25 m.

Its total weight is 7000 tons. As in the CMS, the whole collision point is surrounded by multiple layers of sub-detectors. There are six layers of sub-detectors [22].

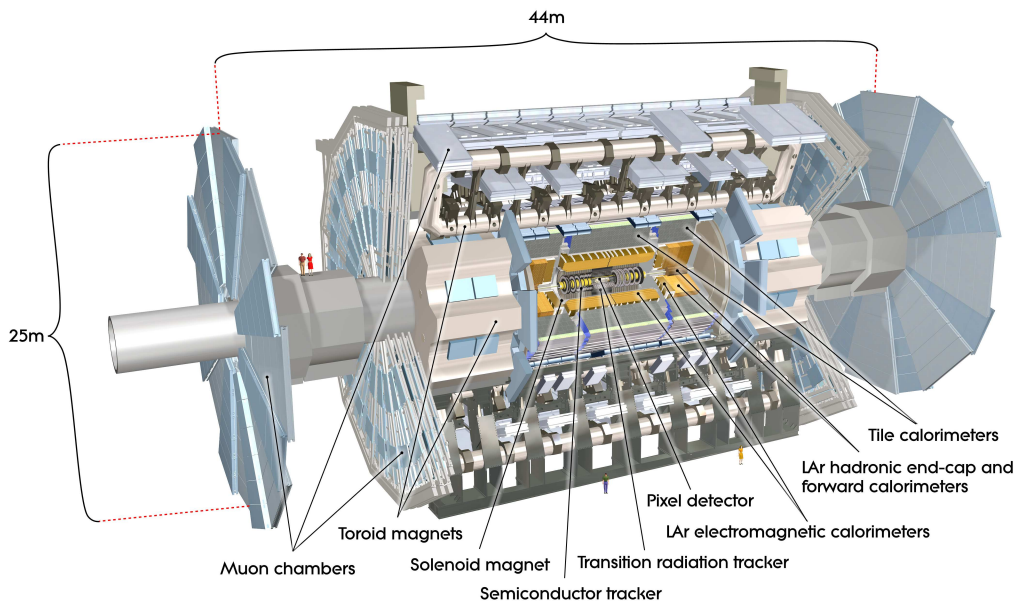


Figure 2.4: The View of the ATLAS Detector (from ATLAS Experiment twiki, 2008) [23].

From inside to outside, the inner detector (Figure 2.5) includes the Pixel Detector, the Semiconductor Tracker, and the Transition Radiation Tracker. Collision products, as well as the decay particles from collision products, interact with different parts of the detector and leave different types of traces. By measuring the hits in the detector that the decay products left as well as the path they follow, the momentum, the energy, the charge and even the identity of the particles can be revealed [24].

1. The barrel of the Pixel Detector has three layers and an endcap at each end. There are three pixel disks in each endcap. On the barrels and disks, there are a total of 1,744 modules with 46,080 readout pixels per module, totally 80,363,520 channels (1,456 modules on the three barrels, 288 modules on the endcaps). The Detector uses 15 kW of power. The size of each pixels is  $50 \times 400 \mu\text{m}^2$  with a resolution of  $14 \times 115 \mu\text{m}^2$ . Since the power is extremely high and the entire detector is close to the collision point, it is important to keep the temperature low ( $-7^\circ\text{C}$ ) to reduce damage from heat [26, 27].
2. The Semiconductor Tracker is a silicon microstrip detector. Its cylindrical barrel has four layers and nine planar discs per endcap. It consists of 4,088 modules and over 6.3 million readout channels (2,112 modules on the barrel, 1,956 modules on the two endcaps). Instead of small

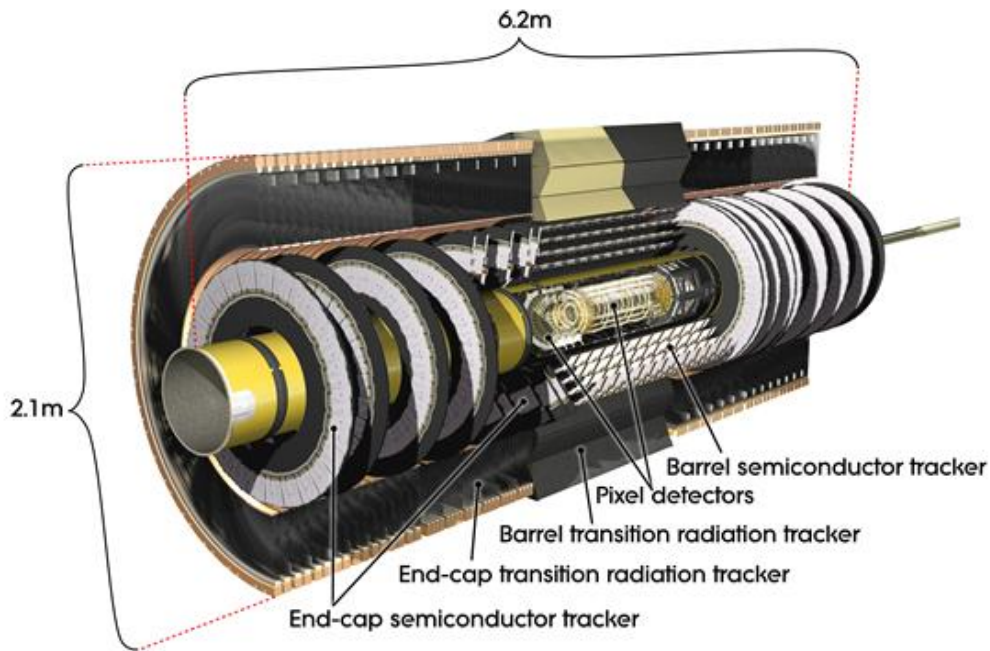


Figure 2.5: The Inner Detector Structure (from ATLAS Experiment twiki, 2008) [25].

pixels, long and narrow readout strips are used on the barrels, and trapezoidal strips are used on the discs. They provide the location of incoming particles with a resolution of  $17 \mu\text{m}$  per layer. The Semiconductor Tracker and the Pixel Detector are both cooled using liquid  $\text{C}_3\text{F}_8$  at  $-25^\circ\text{C}$ ; their target temperature is  $-7^\circ\text{C}$  [27–29].

3. The Transition Radiation Tracker has 350,000 readout channels and a volume of  $12 \text{ m}^3$ . The detector consists of a number of straw-like tubes, each with a diameter of 4 mm. Each straw on the barrel has a length of 144 cm, while each straw on the endcap is 39 mm long. Due to the large scale of the detector, the resolution is lowered (to 0.17 mm) to reduce the cost of the experiments. Each straw is a gaseous ionization detector filled with 70% Xe, 27%  $\text{CO}_2$ , and 3%  $\text{O}_2$ . When charged particles cross the straw, the gas is ionized. A gold-plated tungsten wire of diameter  $30 \mu\text{m}$  is located at the center. The straws are held at a voltage of  $-1500 \text{ V}$ , so electrons will move toward the wire and produce a signal [27, 30].

The ATLAS calorimeter (Figure 2.6) consists of the Liquid Argon Calorimeter (inner) and the Tile Hadronic Calorimeter (outer). They are both sampling calorimeters. They make measurements by absorbing most of the energy of the particles produced from collisions. When a particle hits the energy-absorbing material in the detector, made of a dense metal such as steel, the particle interacts

and produces a particle shower. Then the sampling material evaluates the shape of the particle shower. The ATLAS calorimeter absorbs most known particles, except muons and neutrinos.

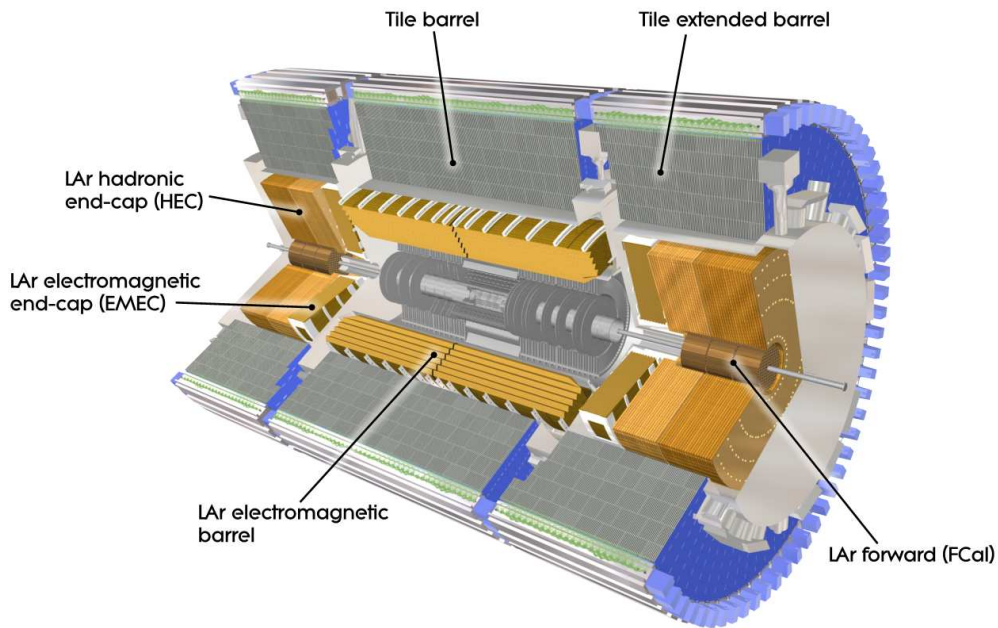


Figure 2.6: The Sectional View of the ATLAS Calorimeter System (from ATLAS Experiment twiki, 2008) [31].

1. The Liquid Argon Calorimeter (LAr) includes the Electromagnetic Calorimeter, the Forward Calorimeter, the Electromagnetic Endcap Calorimeter and the Hadronic Endcap Calorimeter. The Electromagnetic Calorimeter is located in the barrel region, while the other calorimeters are placed at each endcap. The LAr has a 6.4 m long barrel with 110,000 channels [32]. The endcap consists of the Electromagnetic Endcap Calorimeter with radius 2.077 m, the Hadronic Endcap Calorimeter with radius 2.09 m, and the Forward Calorimeter with radius 0.455 m [33]. For the Hadronic Endcap Calorimeter, the energy-absorbing materials are copper and tungsten. For the others, the energy-absorbing materials are lead and stainless steel. The sampling material of all three calorimeters is liquid argon, operating at  $-183^{\circ}\text{C}$  [34]. The LAr absorbs most of electrons and photons [35].
  
2. The Tile Hadronic Calorimeter (TILE) has a barrel made of 64 wedges with a length of 5.6 m per wedge. Its total weight is 20 tons. Each endcap has 64 wedges; each wedge has length 2.6 m. The energy-absorbing material is steel and the sampling material is a set of scintillator tiles.

In total, 500,000 plastic scintillator tiles are used on the TILE [32]. The scintillator tiles send light signals to the photomultiplier tubes (PMTs), which then send electric signals to the readout system. The Tile Hadronic Calorimeter essentially absorbs all hadrons [36].

## 2.3 Muon Spectrometer

The Muon Spectrometer (MUON in Figure 2.7) on ATLAS, which is related to the subject of this thesis, is used for measuring the momentum of muons, with the uncertainty varying from 3% at 100 GeV to about 10% at 1 TeV [37]. It is surrounded by three 8-coil air-core toroid magnets (one for the barrel region, two for the endcaps). Sub-detectors of the Muon Spectrometer include Thin Gap Chambers (TGCs), Resistive Plate Chambers (RPCs), Monitored Drift Tubes (MDTs) and Cathode Strip Chambers (CSCs). The Muon Spectrometer consists of three layers, called the inner, middle, and outer stations. MDTs and CSCs are placed in the barrel area (MDTs in all stations, RPCs only in the middle and outer stations), while MDTs, CSCs, and TGCs are placed in the endcaps. Functionally, MDTs and CSCs are precision chambers which provide high precision measurements of the momentum of muons by observing their traces. TGCs and RPCs are trigger chambers which trigger the muon event with high time resolution. Considering the huge volume of the MUON and high required spatial resolution, to reduce the cost, all the sub-detectors are gaseous detectors. The operation of gaseous detector is as follows: when charged particles cross a gas gap, the gas is ionized and the electrons move toward the mesh due to an electrical field  $E_1$  created by the high voltage applied on the detector. However, the electrical field  $E_2$  in the amplification gap (between the mesh and the readout strips) is much stronger than  $E_1$ . The electrons will then directly pass through the mesh and move to the readout strips to produce the electrical signal.

1. Monitored Drift Tubes (MDTs) are used for measuring tracks. There are a total of 354,240 80  $\mu\text{m}$ -long tubes in 1,171 chambers [39]. It determines the momentum of the muon by precision coordinate measurement in the bending direction of the air-core toroidal magnet. Each tube is made of aluminum and is 30 mm in diameter, with a central W-Re 50  $\mu\text{m}$  thick wire. In order to reduce diffusion and ionization fluctuations, the tubes are filled with a nonflammable gas composed of Ar (91%), N<sub>2</sub> (4%), and CH<sub>4</sub> (5%), at 3 bar absolute pressure [40]. The tubes are

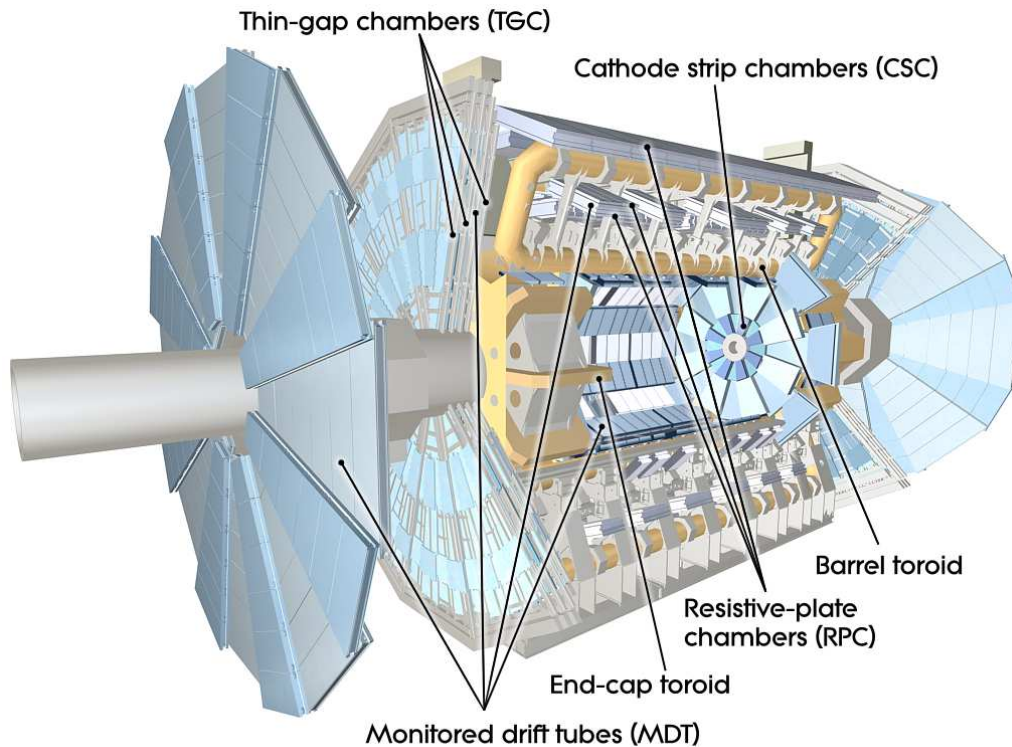


Figure 2.7: The Sectional View of the ATLAS Muon Spectrometer (from ATLAS Experiment twiki, 2008) [38].

held at 3,270 V.

2. Cathode Strip Chambers are placed at the the innermost plane of the two endcaps with good high single-layer track, two-track and timing resolutions. Due to the high rate of events in the forward calorimeters, the two endcaps have the highest background rate in the muon spectrometer. CSCs are four-layer chambers with 70,000 channels which provide a spatial resolution of  $60 \mu\text{m}$ . They are used to determine the precise coordinates of muon tracks. CSCs are multiwire proportional chambers with a 5.08 mm cathode readout pitch. The chambers contain symmetric cells in which the anode wire pitch is equal to the anode-cathode spacing. The anode wire is made of gold-plated tungsten (with the addition of 3% Re) and is  $30 \mu\text{m}$  in diameter. The composition of the gas that fills the CSCs is 30% Ar, 50%  $\text{CO}_2$ , and 20%  $\text{CF}_4$ ; this was chosen to provide low neutron sensitivity [41].
  
3. Due to the high background rate, it is necessary to build an independent and low-occupancy chamber trigger system in the Muon Spectrometer. Resistive Plate Chambers are triggered when muons pass through, and provide second coordinate (azimuthal coordinate) measurements with

a resolution of 5–10 mm in the barrel region. RPCs are gaseous parallel-plate detectors under an electric field of 5,000 V/mm [39]. Two resistive parallel Bakelite electrodes are separated by insulating spacers. The RPCs in the MUON contain a total of 380,000 channels. The digital readout has a space-time resolution of  $1 \text{ cm} \times 1 \text{ ns}$ . When charged particles cross the detector, the gas in the detector is ionized. The gas consists of 94.7%  $\text{C}_2\text{H}_2\text{F}_4$ , 5%  $\text{C}_4\text{H}_{10}$ , and 0.3%  $\text{SF}_6$ ; this composition was chosen to keep the detector working in avalanche mode which will reduce wear of the RPCs. For the same reason, the applied voltage is 9.6 kV [41, 42].

4. Similarly, the Thin Gap Chambers measures the second coordinate of muon events tracks at the endcaps of the detector to complete the bending coordinate measured by the MDTs. 7 layers of TGCs are placed in the middle station of the endcaps; Two layers of TGCs are placed in the inner station. There are 3600 TGCs in all the wheels of ATLAS with 440,000 channels [39]. The structure of a TGC is similar to that of a CSC, but the anode-to-anode distance (1.8 mm) is longer than the cathode-to-anode distance (1.4 mm). For such trigger chambers, high time resolution and high efficiency under a high background rate ( $1 \text{ KHz/cm}^2$ ) are required for in TGCs. The high gap resolution ( $\leq 100 \mu\text{m}$ ) and efficiency ( $\geq 99\%$ ) comes from the high voltage ( $3.1 \pm 0.1 \text{ kV}$ ) applied across the TGCs and the small distance (1.8 to 2.5 mm) between wires [43]. The high-rate capability of the TGCs is up to  $20 \text{ kHz/cm}^2$ . The gas is a mixture of 55%  $\text{CO}_2$  and 45% n-pentane, which leads to good time resolution by achieving saturated mode. This also prolongs the life of the detector [41].

The magnet system of ATLAS is used to provide a strong magnetic field which influences the paths that particles take through the various detector structures. The momentum of each particle is evaluated by its trace, which is determined by the Lorentz force due to the magnetic field. The magnet system includes a central solenoid magnet, a barrel toroid, and endcap toroids. The central magnet is a conduction-cooled superconducting solenoid. It produces a 2 T magnetic field which covers the central tracking area. It has a length of 5.3 m, a thickness of 4.5 cm, a diameter of 2.4 m, and a weight of 5 tons. The barrel toroid consists of eight separate coils with 1.08 GJ of stored energy. The toroid produces a 4 T magnetic field. Each coil is 25.3 m long and has a diameter of 5 m. One endcap toroid is placed at each end of the central solenoid. They both produce a 2 T magnetic field, and each contains

eight superconducting race-track coils. Each coil is 5 m long and 1.5 m wide. The barrel toroid and the endcap toroids are used to provide magnetic field for the Muon Spectrometer [44].

## 2.4 New Small Wheel Upgrade Project

To obtain more precise data results for the Higgs sector, a higher luminosity of  $5 \times 10^{34} \text{ cm}^2\text{s}^{-1}$  is required for the third run of the LHC (2021). Under such conditions, the particle rate through the MS's Small Wheel area (the inner stations of the endcaps) will reach  $15 \text{ kHz/cm}^2$  [45]. Meanwhile, the fake trigger rate is significant ( $> 90\%$ ) in the endcap region due to background low energy particles [46]. In order to provide effective trace data, minimize fake triggers, and improve the transverse momentum  $p_T$  resolution in the presence of such a high background rate, the New Small Wheel will be installed during the long term shutdown (2018 to 2021) to replace the original one.

The New Small Wheel (NSW) consists of eight layers of small-strip Thin Gap Chambers (sTGCs) and eight layers of Micromegas (MM) detectors. Each wheel is composed of sixteen sectors (eight small and eight large sectors). For each sector, four quadruplets MM wedges are placed between two sets of two quadruplets sTGCs. The structure of NSW is shown in Figure 2.8.

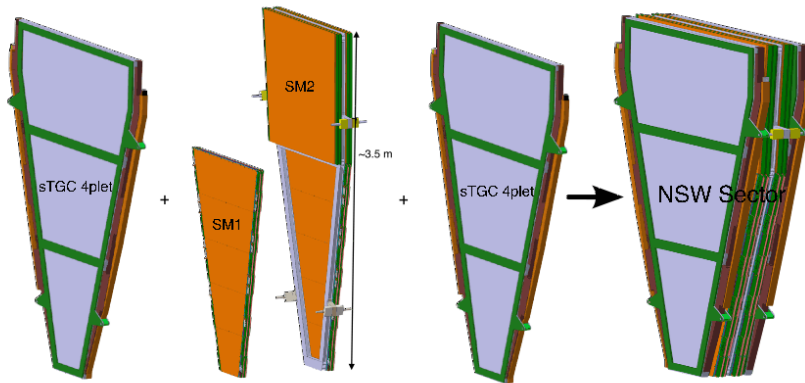


Figure 2.8: NSW structure (from K. Ntekas, 2014) [47]. The SM1 and SM2 are two different sizes of MM detectors.

The MM detectors are micropattern gaseous detectors. A MM detector consists of a planar electrode, a gas gap (filled with 97% Ar and 3%  $\text{CO}_2$ ), a metallic mesh, readout stripes and resistive strips. The resistive strips are installed above the readout stripes to provide a higher tolerance to electric

charge and avoid sparks which would damage the detector. Therefore, the MM detector will be functioning well in high background rate conditions [47].

Like TGCs, sTGC detectors are triggered by muon events. In the lab, the hodoscope triggers the sTGC. The structure of the sTGC is an improvement on that of the TGC, as shown in the Figure 2.9. One side of the anode plane contain copper pads which trigger faster; the other side is made of copper readout strips which is used to measure the transverse momentum. Apart from the addition of pad readout for the high luminosity conditions, the differences between TGCs and sTGCs are the resistivity of cathode plane and the size of the readout strip pitch. To increase the rate capability, the resistivity of the cathode plane is changed from 1 M $\Omega$  to 100–200 k $\Omega$ . The readout strip has a 3.2 mm pitch, reduced from 2 cm in the present TGCs, to obtain a higher spatial resolution of 100  $\mu$ m (hence the name small-strip Thin Gap Chambers). The operational gas is still a mixture of CO<sub>2</sub> and n-pentane [48].

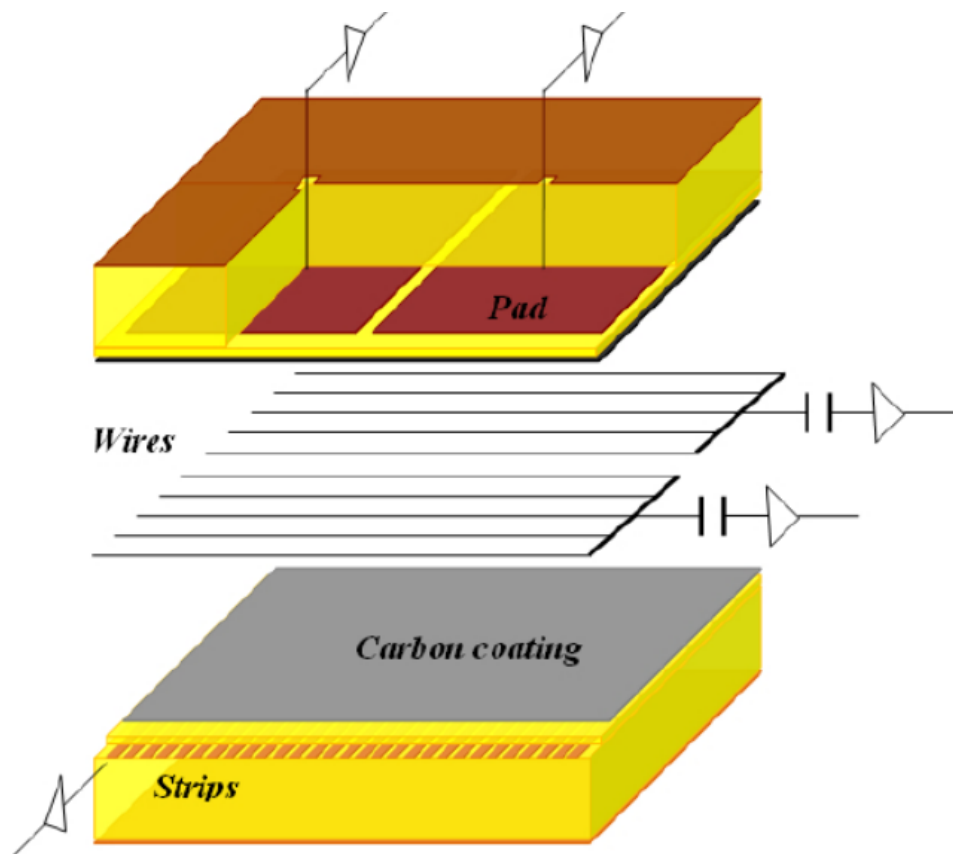


Figure 2.9: A schematic cross-section of a sTGC detector (from A. Klier, 2014) [48]

The readout chip on both sTGC and MM detectors is a frontend ASIC called VMM. It provides the pulse height and timing. The first version of VMM (VMM1) has been successfully tested (the one

equipped on the sTGC in McGill lab currently). However, the VMM1 has no digitization logic. Every functionality, such as analog circuitry, will be on the VMM2, except for the redundant storage of the register content which helps reduce the sensitivity to radiation for the configuration data. The VMM3 will be the final version used on the NSW [49].

Canada, as one of non-member states with co-operation agreements with CERN, is involved in the ATLAS program at CERN. There are over 150 scientists from 9 universities and one institution (University of Alberta, Carleton University, McGill University, University of Montréal, Simon Fraser University, University of Toronto, TRIUMF, University of British Columbia, University of Victoria, York University) in Canada to work on the ATLAS program. ATLAS Canada was constituted in 1992 and is supported by the Natural Sciences and Engineering Research Council of Canada (NSERC). The main activities of ATLAS Canada are studying the Higgs bosons, searching the SUSY with jets, leptons and Higgs bosons, studying top-quark physics and so on. Contributions from ATLAS Canada include designing and building components of the ATLAS detector, such the cryogenic feedthroughs for the liquid argon calorimeters (Victoria) and the liquid argon hadronic end-cap calorimeters (TRIUMF and University of Alberta), making contribution to the software, or for example hosting a Tier 1 Computing Centre (TRIUMF) and providing the High Level Trigger (McGill) [50]. One of the main tasks of ATLAS Canada, which related to this thesis, is to build and test one third of the sTGCs which will be used in the New Small Wheel, together with ATLAS groups in Israel, China, Russia and Chile. TRIUMF prepares graphite-coated cathode planes. The speed of the conveyors, the temperature of supply air and humidity have influence on the quality of the coating, therefore, TRIUMF has the duties to optimize all the parameters to make sure that the graphite has very uniform resistivity [51]. Carleton University is responsible for the assembly and wiring of the sTGC quadruplets. A multichannel system is operated by Carleton University to check the electrical response and characteristics of the hundreds of readout channels on a sTGC detector. McGill University is in charge of testing their performance, such as detector characterization, quality control and acceptance with cosmic muons. The details are presented in the following chapter 3.

## Chapter 3

---

# Lab at McGill University

---

### 3.1 Cosmic Muons

The main type of particles we observe in our measurements to test the efficiency of the trigger system or the sTGC are cosmic muons. The sources of cosmic muons are cosmic rays, which have very high energies (normally between 100 MeV and 10 GeV) [52]. Cosmic rays mostly come from outside the solar system. Astrophysicists suspect high energy cosmic rays come from supernovae and the lowest energy cosmic rays come from the Sun [53]. Particles, such as electrons, protons, helium, and other nuclei synthesized in stars, when emitted from astrophysical sources, are called primary cosmic rays [54]. When primary cosmic rays interact with atoms of the upper atmosphere, they produce so-called secondary cosmic rays. Pions, muons, electrons and positrons count among secondary cosmic rays.

In the atmosphere, cosmic rays include all stable charged particles and nuclei, which mostly have lifetimes in the order of  $10^6$  years or longer. 79% of primary cosmic rays are free protons [55]. When they reach the atmosphere of the earth, they collide with atoms in the atmosphere and produce secondary particles, such as mesons, pions and kaons. Because muons have much longer lifetime (2.197  $\mu$ s) than pions (26 ns), at sea level, muons are the most numerous charged particles left over from charged mesons decay [55]. The decay process happens in the atmosphere (typically 15 km). Due to interactions with particles in the atmosphere, the muons generally lose about 2 GeV when they reach the ground. The measurements of the energy and angular distribution of muons are usually made near ground level. The results show that the mean energy of muons at the ground level is about 4 GeV

and the angular distribution of muons is proportional to  $\cos^2(\theta)$  where  $\theta$  is the angle between the muon path and the vertical. Muons at sea level have an approximate average flux of  $1 \text{ cm}^{-2}\text{min}^{-1}$  [55].

### 3.2 McGill sTGC Lab

One of the responsibilities of the McGill ATLAS group is testing the quality and assessing the performance of the new Canadian-made sTGC detectors. To do this, a hodoscope equipped with a scintillator trigger system, a gas supply system, and associated services have been built in the McGill sTGC lab. A custom-made gas system is installed there, containing five pentane-CO<sub>2</sub> mixture lines and five CO<sub>2</sub> lines. It is used to provide the CO<sub>2</sub> that cleans away the air from the chambers before the n-pentane-CO<sub>2</sub> gas mixture is fed in. Since n-pentane is an explosive and highly flammable gas, the safety regulations of the McGill facility and of CERN require that a Slow Control System (implemented in LabVIEW) be installed to acquire and record data from the gas system and high voltage supply, as well as to control all the gas lines and provide alarm signals. The block diagram for the frame of the measurement is shown in Fig 3.1.

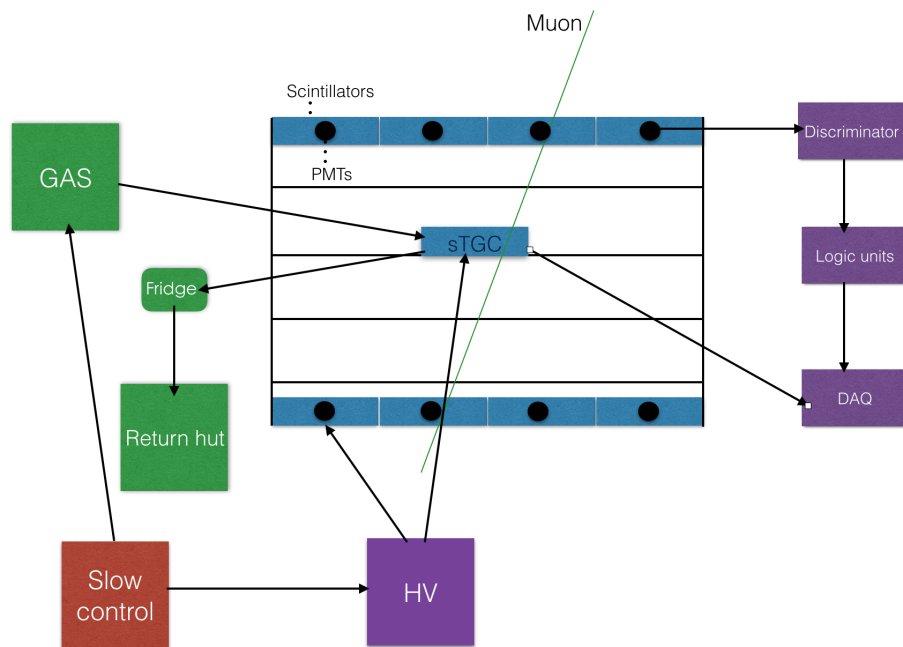


Figure 3.1: The block diagram for TGC Lab in McGill. The working principle is shown above. The blue parts represent the scintillators (8), The blacks parts represent the PMTs (8) from the front view. For clarity, duplicate arrows to each PMT are not shown.

The muon triggering system provides a trigger signal to the detector's front end electronics, essential

for the measurement of muon passage through the sTGCs. Finally, the sTGC electronics readout is recorded by a data acquisition system.

The TGC lab is shown in Figure 3.2.



Figure 3.2: The TGC Lab in McGill. From right to left: gas system, construction where triggering system and sTGC detectors are placed, lifting jack, slow control system– work space with computers and accessories.

## 3.3 The Trigger System

The part which the thesis was involved in is the trigger system. The trigger system is made of eight scintillators and sixteen PMTs. My main work is to ensure the efficiency of the trigger system, which maximizes the accuracy of measurement when the muon passes through the system. The structure of the trigger system is shown in Figure 3.3.

In the lab, there are logic units, fan in/out, counters, and discriminators to analyse the signals from the PMTs. The lab is also equipped with an oscilloscope. It provides a visual display of the signal to understand its shape, and helps us to distinguish between crosstalk and real signal. This will be discussed in subsequent chapters. In this chapter, the physical principles of all the components are introduced.

### 3.3.1 PMTs and scintillators

A scintillator is a material that emits an amount of photons when excited by charged particles. The scintillators used in our lab are manufactured by Eljen (EJ-200). Their refractive index is 1.58 and their wavelength of maximum emission is 420 nm [56].

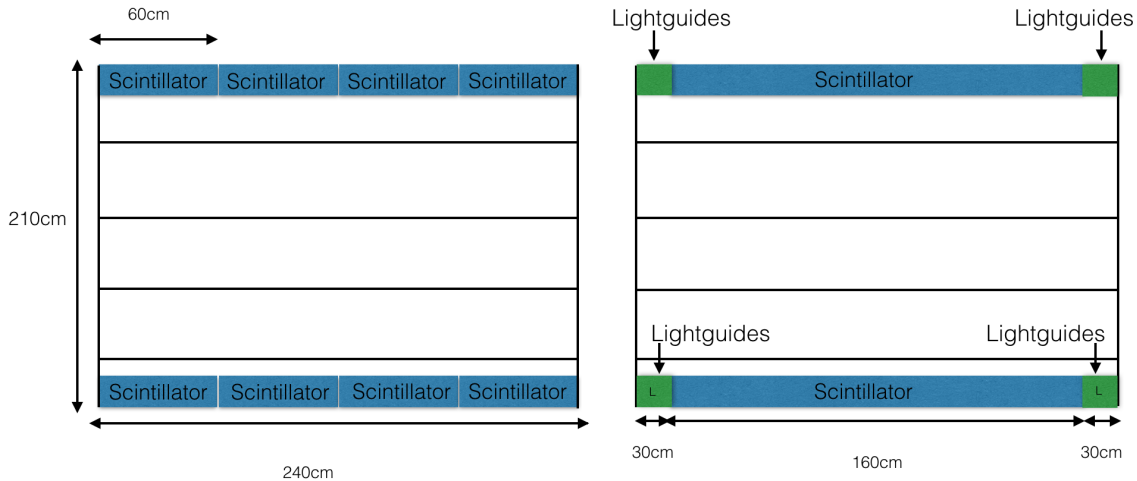


Figure 3.3: The geometry of the trigger system with structural parameters. The left part is the front view. The right part is side view. The blue parts represent the scintillators. The green parts represent the lightguides. The black lines represent construction where sTGCs will be place. Up to 4 sTGC chambers can be inserted on the shelved for measurements.

The PMTs are extremely sensitive to light signals. They work as follows. When photons reach PMTs, they eject electrons from the photocathode material at the front of PMTs (the glass part). Those electrons are called primary electrons. These then encounter a series of dynodes, each of which multiplies the electronic signal until it becomes strong enough to be easily detected. The PMTs used in our lab are from Hamamatsu Photonics. The diameter of the photocathode is 51 mm. (It is slightly bigger than the interface to the lightguide, but this won't affect the results since the whole thing is covered with seven layers of black tape to make sure all photon signals remain in the system.) The PMTs have a peak efficiency at 420nm, which is a match with the emission wavelength of the scintillator. The maximum voltage (anode to cathode) which may be applied on the PMTs is 2700 V [56].

Due to the rectangular shape of the scintillators, lightguides are used to connect the scintillators to the PMTs. The sizes of scintillators are 160 cm  $\times$  60 cm  $\times$  2.5 cm. The lightguide's shape is that of an isosceles trapezoid with same thickness as scintillators'. The length, the topline and the baseline are 30 cm, 6 cm, and 60 cm respectively. The baseline (60cm) matches the width of the scintillator (60cm). Since we install two PMTs on each scintillator, we require two lightguides on each. The index of refraction of the lightguides is 1.502 at a wavelength of 426 nm (which is close the wavelength of maximum emission for the scintillators) [57]. This is also reasonably close to the index of refraction of the scintillators (1.58). This causes less refraction at the interface, which simplifies our simulation (as

we will see later in Chapter 6).

The wrapping material includes black vinyl, black tape, and Tyvek. The black vinyl and the black tape are used to cover the whole scintillator. Tyvek is formed from high-density polyethylene fibers which reflect most of the light by diffused reflection. In our case, it also helps to reduce the air gap between the black vinyl and the scintillators.

In the fall of 2015, we started to build the trigger system. It works as follows. When a muon crosses the scintillator, it produces a certain amount of photons. When these photons reach a PMT, the PMT creates an electrical signal.

Before gluing them, 400 grit sandpaper are used to sand the contiguous surfaces of the scintillators and lightguides. This increases the effective surface area by grinding defect, which will help the gluing process. Glue is prepared by using the 3:1 volume ratio as follows: 3mL of resin and 1mL of hardener. After mixing the glue, it takes approximately three hours and fifteen minutes for it to be sticky enough to apply on the lightguides. We then apply three-centimeter-long stripes of glue onto five equally-spaced points on a lightguide. After this, the lightguide is pressed onto the scintillator. Using a flashlight, we need to check the shape of the glue from the other side of the scintillator (to make sure the glue isn't bubbling). Then we repeat the same process for the other side of the scintillator. The whole thing is held in a gluing structure (Figure 3.4) to prevent it from falling apart. After 36 hours, the glue becomes hard enough to hold the scintillators and lightguides together permanently.

From this point on, we will refer to the scintillator-lightguide system simply as “the scintillator” for convenience, unless otherwise indicated.



Figure 3.4: The gluing structure of scintillator and PMT.

Before gluing, Tyvek is used to cover the scintillator. After gluing, the scintillators are wrapped in black tape and black vinyl. The high reflectivity of the Tyvek prevents photons produced within the scintillator from escaping the system. Following that, the whole system was furthered encased in black vinyl to prevent outside photons from leaking into the system. The scintillator with lightguide are shown in Figure 3.5.



Figure 3.5: The structure of the scintillator and lightguide after wrapped in black vinyl. The size of the scintillator is  $160\text{cm} \times 60\text{cm} \times 2.5\text{cm}$

Finally, we glue the PMTs to the lightguide assembly. The process of gluing the PMTs to the scintillator is irreversible. As such, the PMTs have to be tested in advance to ascertain they are in working order. The method of testing as well as the results of the tests are given in Chapter 4.

The scintillators are used as trigger system to test the detectors. We build a structure with four layers to place accommodate up to 4 sTGC detectors simultaneously. It is shown in Figure 3.6.

Considering the size of sTGC detector, we place 4 scintillators on top and four at the bottom, side by side (Figure 3.3). The scintillators are labelled according to by their geographical position. As shown in Figure 3.7, they are classified according to three parameters: West/East, Outer/Inner, Top/Bottom. Since there are two PMTs on each scintillator, one is on the north side of the scintillator and the other is on the south side of the scintillator. PMTs are labelled based on which scintillator, as well as which side of the scintillator they are glued on, For example, the PMT which is placed at the north of the TWO scintillator would be called NTWO.

There are two cable connectors on each PMT. One of connectors is the HV cable, used to power the PMT. Another one is the signal cable which transmits the output signal. The setting of impedance



Figure 3.6: The four layers structure picture of the hodoscope.

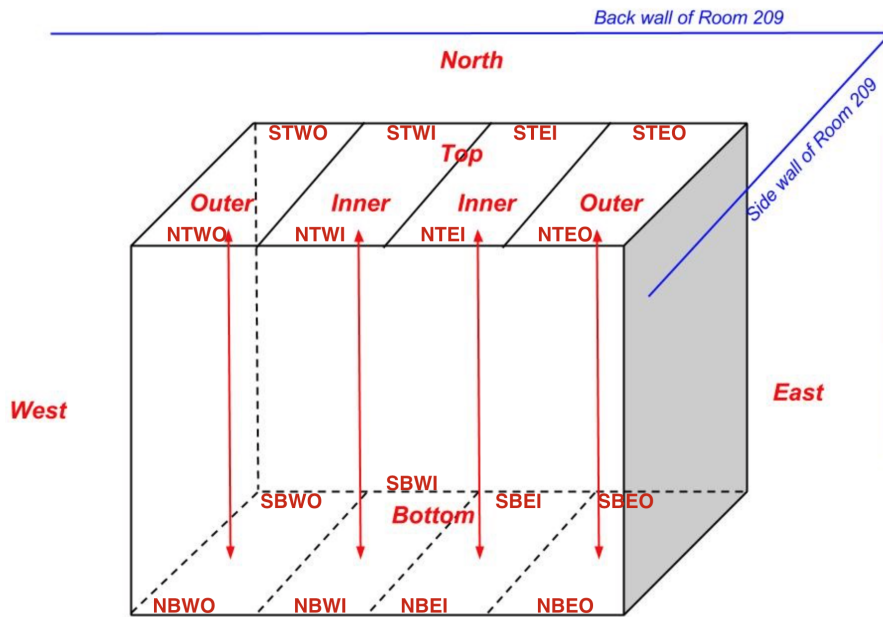


Figure 3.7: the PMTs are labelled according to their geographical position in the trigger system structure, the North/West/South/East are correlated to the geographic orientation.

on both discriminators (LeCroy 623A and CAEN N843) is  $50 \Omega$  for most our measurements [58, 59]. To maintain the stability of the signal, before we install the cables to the PMT, we need to put the  $50 \Omega$  connector on the signal cable of PMT. We also install the cable tray in order to reduce the crosstalk signal, which will be discussed in Chapter 5.3.

### 3.3.2 Electronics

The high voltage for the PMT is supplied by a CAEN SY4527 power supply [58]. Only the sections with negative outputs can be utilized due to the characteristic polarity of the PMTs. Each section has sixteen channels; each channel can connect with one high voltage cable to supply one PMT. Some parameters that can be controlled include maximum current, maximum voltage, rate of increase and decrease of voltage, etc. There are two ways to control the power supply system. One is to manually regulate the parameters using the system's touch screen; the other is to create a HV panel on the computer. The HV panel in our lab is written in LabVIEW. Its simple interface makes the panel easy and convenient to work with. The HV panel, rather than the touchscreen, is mainly used in all our measurements.

The electronics system includes discriminators, logic units, fan in/out, and counters. The discriminator takes the original electrical input signal and converts it into a stable digital signal that can be used by the other electric units.

There are two kinds of discriminators : the threshold triggering discriminator and the constant fraction discriminator. The working principle of the threshold triggering discriminator is as follows: once the input signal exceeds a certain threshold voltage, the discriminator will produce a digital square signal with a certain length. The advantage of this kind of discriminator is that it is easy to adjust the threshold voltage to the level we require. The threshold triggering discriminator used in our lab is the LeCroy 623A octal discriminator. It has eight channels, with one input and three outputs each. A precise screwdriver (1.2 mm) is needed to adjust the threshold voltage and width for each channel. From the previous results, the maximum threshold voltage of the LeCroy 623A discriminator is -30 mV. This discriminator has a response time of 11 ns which is sensitive enough for our measurements [59].

However, this type of discriminator is vulnerable to a problem called time walk. An example is the case of two input sinusoidal signals with the same frequency and starting point, but different amplitudes (both exceeding the threshold voltage). One expects the same output from both signals. However, the signal with lower amplitude will produce a significantly delayed output signal, since the two signals reach the threshold voltage at different times. To solve this issue, another kind of discriminator is available: the constant fraction discriminator (CFD). The one used in our lab is the CAEN N843 [58]. The CFD can transform an input signal into two intermediate signals: an attenuated

version of the input signal and a delayed version of the input signal. The delayed signal is the same as the original input signal with a delayed time. The attenuated signal reduces the original signal by a constant fraction. The delay is set on the discriminator and there are three full scale settings (20 ns, 50 ns and 100 ns). For each scale, there are five jumper steps. For example, if we choose the 20 ns as the full scale, the delayed time will jump among 4 ns, 8 ns, 12 ns, 16 ns, or 20 ns depending on the rise time of the input signal. The CFD will choose the delay time on the jumper scale which is closest to the calculated delay time as shown in Fig 3.8 [58, 60].

$$T_{delay} = T_{risetime} \times (1 - F) \quad (3.1)$$

$F$  is the constant fraction value (20% in CAEN N834). The smaller the difference between the actual and calculated delay times, the smaller the walk time. If the crossing point of the attenuated and delayed signals exceeds the threshold voltage, the CFD will produce the output signal at the time of crossing.

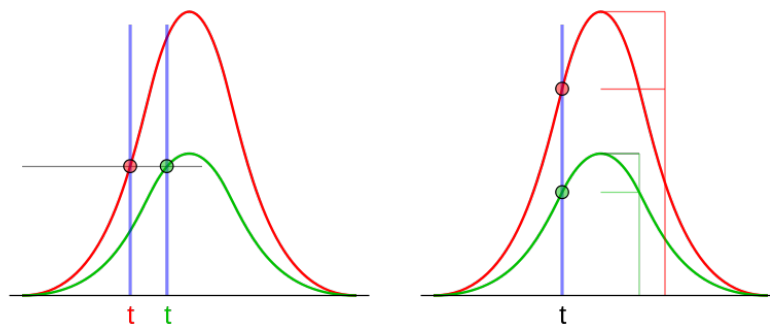


Figure 3.8: Comparison of threshold triggering (left) and constant fraction triggering (right) (from Dschwen, 2006) [61]. The latter reduces greatly the dependence on the signal amplitude.

Although the principle of the CFD is not trivial, the CAEN N834 is very easy to use. The threshold voltage can be adjusted from 0 mV to -255 mV in 1 mV increments. The width of output range can be changed from 18 ns to 318 ns in 1 ns increments. There are two switches: the Upper switch and the Lower switch. The Upper switch is used to determine the parameter that we want to change the threshold voltage, the width of output or the dead time (the parameter is not important in our measurement). The Lower switch controls whether the discriminator is unlocked or locked to the value we set on the parameter. The black rotary handle allows us to set up the value we need for the

parameter. An important fact to be mentioned is that we need to lock the parameter every time we choose the final value for the parameter. There are 16 input channels and 48 output channels which can be selected by pushing the “or” button. The maximum value of input cannot be more than 2 V without causing damage to the discriminator. The width of output signal from discriminator is set up as 37 ns, considering the maximum time difference of two PMT signals for one muon even due to the size of the structure, ignoring the individual difference of the rise times.

The fan in/fan out is CAEN model N625. This device takes an input signal and outputs multiple copies of it. It can output up to four copies of one input signal.

The logic unit is CAEN module N405. This device performs logical operations on its input signals. There are three independent sections. For each section, there are four input channels and four output channels (including one anti-output). There are two logic functions for each section: "or", "and". An input channel can be disabled by switching the button on the front panel. Any input signal will trigger an output signal if the "or" function is on. Two input signals with at least 2 ns overlap will produce one output signal when "and" logic is used to measure the coincidences [62].

The device used for counting muon events is the CAEN module N1145 quad scaler and preset counter/timer. The events, which are chosen to be counted, depend on the measurements. They are single muon events, double muon events and so on. There are four channels to record separate data. There are two ways to collect data. One method is counting how many events happened in a fixed time period; another method is counting how much time is required for a certain number of events to occur. It provides the information about the rate of the event required. The block diagram of operating principle for the data acquisition system is shown in Fig 3.9.

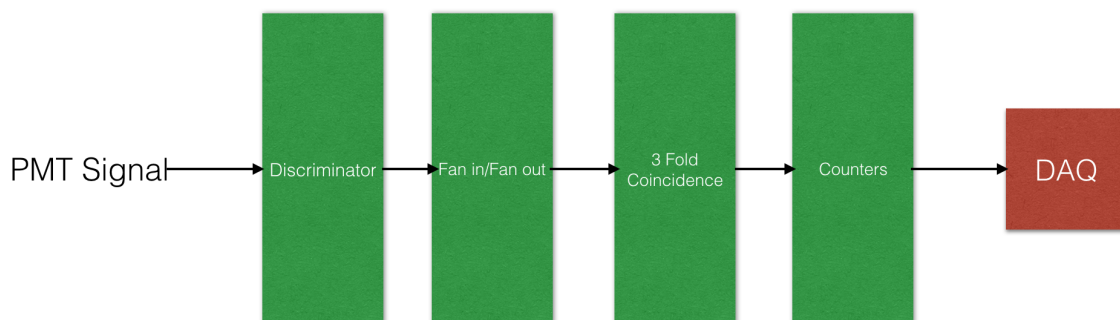


Figure 3.9: The block diagram for the data acquisition system.

## Chapter 4

---

# Data Taking and Results

---

In this chapter, all the test measurements taken in the TGC lab are presented.

### 4.1 PMT Performance Test

Since the process of gluing PMTs to scintillator is irreversible it is important to test a PMT's performance before gluing it. Due to the high light sensitivity of PMTs, we require an environment without external light. Once the PMT is powered on, any high intensity external light source, such as room lights or sunshine, would damage it permanently.

The setup of the measurement is shown in Figure 4.1. We use a cardboard box to build a test box. A LED, a LED driver, the PMT, and a photodiode are installed inside. The LED provides low intensity photons. The LED driver regulates the power to the LED. The photodiode (it converts light into current) is supposed to provide an independent signal to check if the LED is working. However, the photodiode in our lab is quite noisy. Therefore, it is not used for the following test, which won't actually affect the result in the normal cases where the PMT catches the signal from the LED. Whenever the PMT is powered on, the box is sealed with black tape and covered with two layers of black plastic packaging. The LED and the PMT are set up on opposite sides of the box. To make sure that the PMT receives the maximum number of photons from the LED, the head of the LED is placed toward the photocathode of the PMT. The position of the LED is as high as the axial wire of the PMT. Two cables are connected to the PMT, the high voltage cable and the signal cable. The high voltage cable is connected with our power supply system (CAEN SY4527). The signal cable is connected with the oscilloscope. Similarly,

the LED is powered by the LED driver.

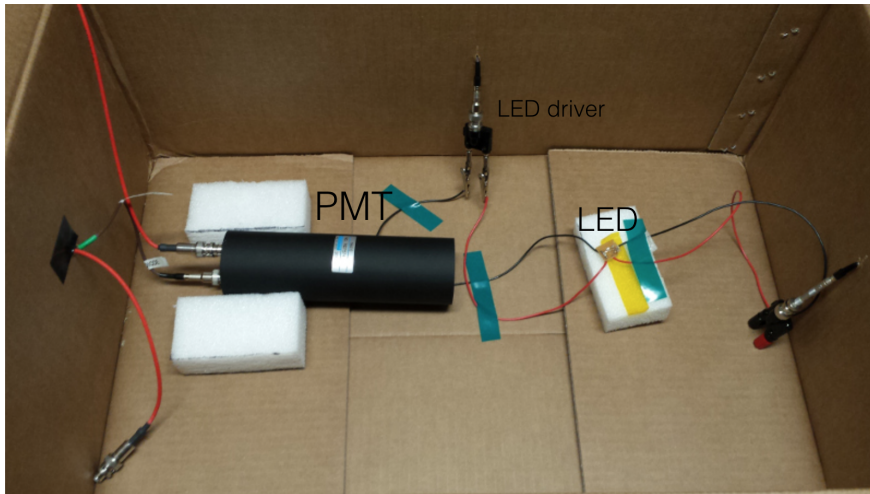


Figure 4.1: PMT performance test setup.

All 18 PMTs are tested to make sure that they function properly by quantifying the amplitude and the width of the PMT signals. The optimal voltage of the PMTs and LED are known (from the manual, 1500 V for the PMTs, 2.65 V for the LED). The only unknown parameters are the frequency and the width of the LED signal. They are chosen to make sure that the PMT response looks like that of a genuine muon signal. The rise edge of the PMT signal for any individual event should be sharp (the slope depends on the rise time), and the fall edge should be gentle (normally two or three times longer than rise edge) [63]. The expecting shape of PMT responding signal is shown in Figure 4.2.

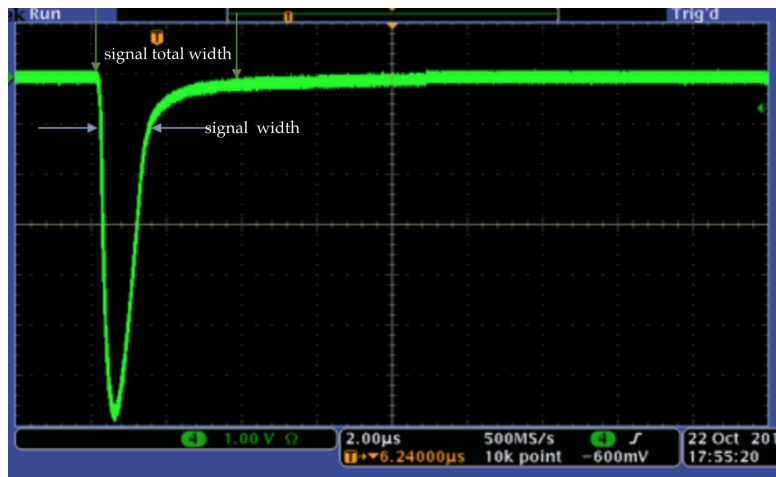
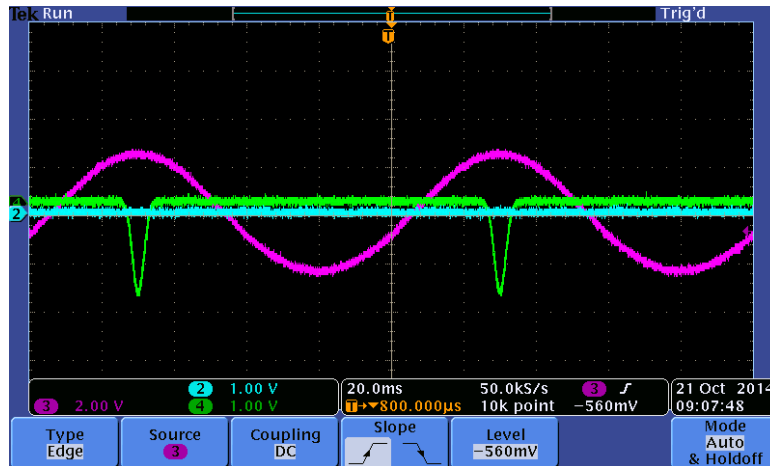
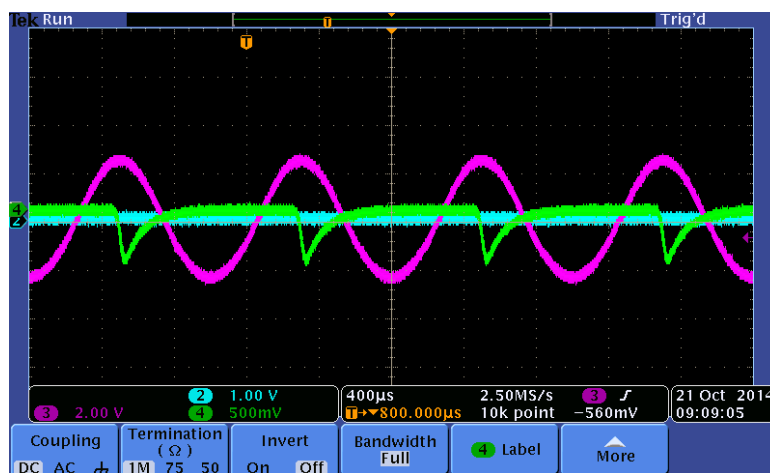


Figure 4.2: The expecting shape of the PMT signal. The PMT signal width is the width between the signal rising edge and falling edge at approximately 15% of the signal height. The PMT signal total width is the width of the signal at approximately 2% of the signal height when it falls into the noise.

The first measurement is to determine the frequency of the LED signal. The chosen frequencies



(a) the frequency is 10 Hz



(b) when the frequency is 1 kHz

Figure 4.3: The green color line identifies the PMT signal, the pink color line identifies the LED signal.

of the signal are set to 10 Hz and 1 kHz. Since it is our first measurement, we set the termination on the oscilloscope to 1 M $\Omega$ , which is the original setting. This does not have much influence on the test results, because the output cable of the PMT is not connected with any device with 50  $\Omega$  impedance (ignoring the influence of the cable itself). However, to insure consistency, we chose 50  $\Omega$  termination for all subsequent measurements. Also, in the first measurement the signal of the LED was sinusoidal (Figure 4.3). But for later measurements, it was decided that the LED signal should be a narrow pulse, similar to the one of real muon events. The choice of the shape of the LED signal also won't affect the test results about the frequency of the LED signal.

As shown in Figure 4.3, when the frequency is 10 Hz, the signal from the PMT (channel 4 green line) is a symmetrical pulse. However, when the frequency is 1 kHz, the signal has a sharp rise edge and a gentle falling edge. It is clear that the 1 kHz setting gives results that fit what is expected of the

PMT signal.

The purpose of the second measurement is to decide the width of the LED signal. The pulse width of the LED is increased by steps from 100 ns to 9  $\mu$ s. As shown in Figure 4.4, a full PMT signal could not be observed until 9  $\mu$ s is reached. Therefore, 9  $\mu$ s is chosen as the width of the LED signal.

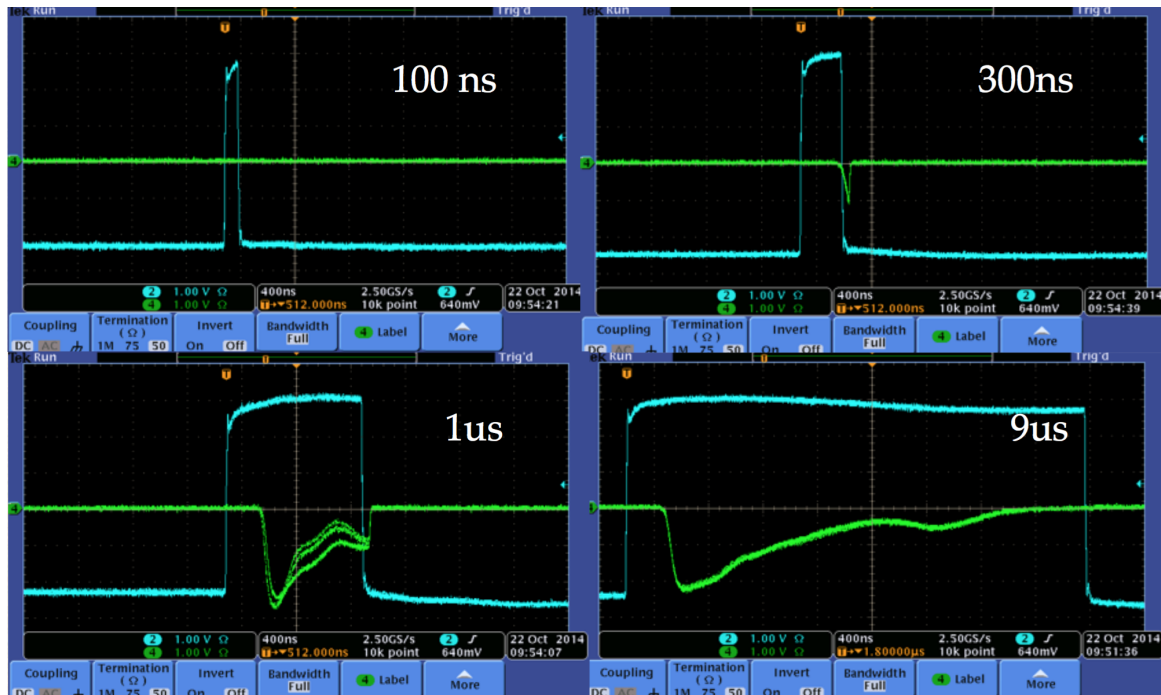


Figure 4.4: The shape of PMT signal changed along with the width of the LED signal. The green color line identifies the PMT signal, the blue color line identifies the LED signal.

As shown in Figure 4.5, we observe that when we connect the LED driver to the oscilloscope and try to read the LED and PMT signals at the same time, the signals become unstable. We therefore decided to measure the LED and PMT signals separately. The explanation of the phenomenon is unclear and could be due to some ground loop. Since the LED signals are always the same, we only need one diagram for it.

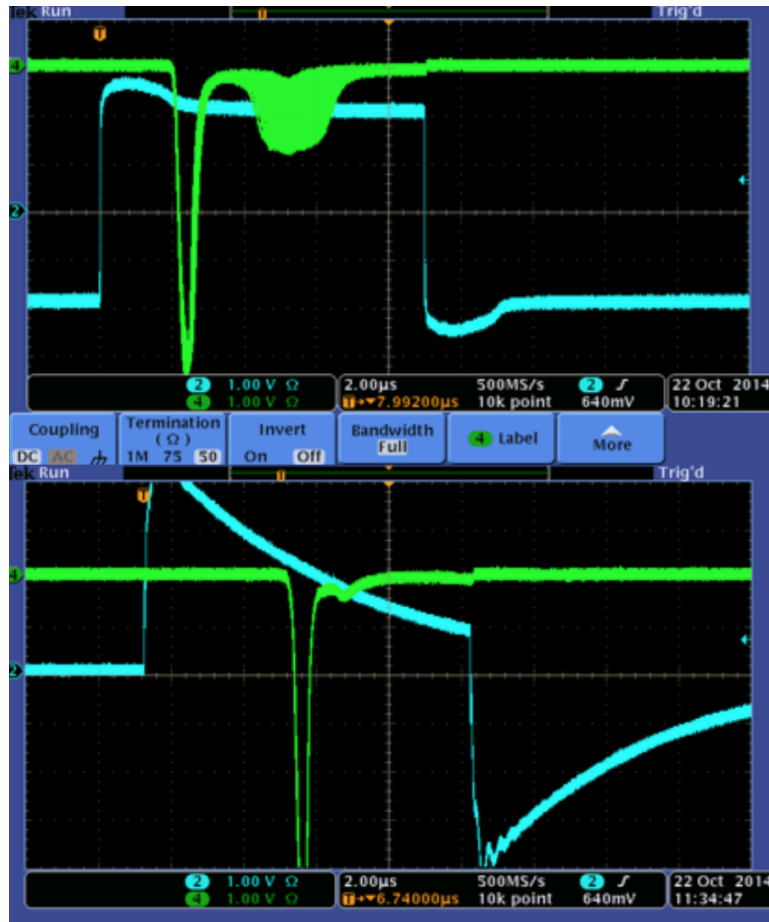


Figure 4.5: Unstable PMT signals (top) and unstable LED signal.

Up to now, two parameters for testing the PMT performance are decided. The setting is as follows in Table 4.1.

LED	Shape	LED volt	Frequency	Width of Pulse	Termination
	Narrow pulse	2.65 V	1kHz	9 $\mu$ s	50 $\Omega$
PMT	I0set(max current)	PMT volt			
	600 $\mu$ A	1500 V			

Table 4.1: The common parameters for all PMT and the LED.

Results are shown in Table 4.2 for all 18 PMTs: the current, signal amplitude, signal width, and signal total width are studied. As shown in Figure 4.2, the PMT signal width is the width between the signal rising edge and falling edge at approximately 15% of the signal height. The PMT signal total width is the width of the signal at approximately 2% of the signal height when it falls into the noise. There are some individual differences among the PMTs, however they are not significant. As a conclusion, the behaviors of the PMTs remain consistent. 16 out of 18 PMTs are chosen to be glued on

the scintillators. PMT RD7695, PMT RD7686 and PMT RD7693 have lowest output signal amplitudes among all PMTs. Compared with PMT RD 7693, PMT RD7695 and PMT RD7686 are not chosen due to their small signal widths.

PMT label	PMT number	PMT current ( $\mu\text{A}$ )	PMT signal amplitude (V)	PMT signal width ( $\mu\text{s}$ )	PMT signal total width ( $\mu\text{s}$ )
SBEO	RD7648	391	5	1.6	3
NBEO	RD7677	390	5	1.6	3
NTEI	RD7574	390.5	5	1.6	3
STWO	RD7689	390.5	5	1.2	2.4
NTWO	RD7693	385.5	3	2	3
STEI	RD7688	395.5	6.5	1.4	4
STEO	RD7697	391	5.5	1.6	2.8
NTEO	RD7649	397.5	5.5	2	4
SBEI	RD7639	395.5	5.5	1.8	3
NTWI	RD7702	393.5	6.8	1.8	4
STWI	RD7703	392.5	6.8	1.6	3.6
NBWO	RD7644	400.5	7	1.6	4.1
SBWO	RD7651	389	4.5	2	4
SBWI	RD7665	393.5	6.2	1.5	2.9
NBEI	RD7682	393.5	6.8	1.6	3
NBWI	RD7692	394	5.2	1.7	4.1
	RD7695	384	3	1.8	2.8
	RD7686	384.5	3	1.2	2.4

Table 4.2: It is the table for PMT performance. All PMTs are tested under a high voltage of 1500 V.

The findings are, first of all, that the PMTs do respond to input light. Secondly, the shapes and widths of the signals are consistent across all PMTs with some reasonable variations. Finally, PMT RD7648 is touched to the lightguide with black tape. It responded with a nice 20 ns pulse to a real muon signal from the scintillator in Figure 4.6.

The shape of the signal fits our expectation as shown in Figure 4.2. The signal have a nice sharp raising edge and a gentle falling edge. The second pulse on the signal is due to the internal reflection in the scintillator (see later in Chapter 6). As a conclusion, the behavior of PMT RD7648 is satisfactory and can be glued onto the scintillator.

Unfortunately, there is no straightforward way to conduct more realistic tests on our PMTs before they are glued onto the scintillators. But the tests described above allow us to conclude that the PMTs

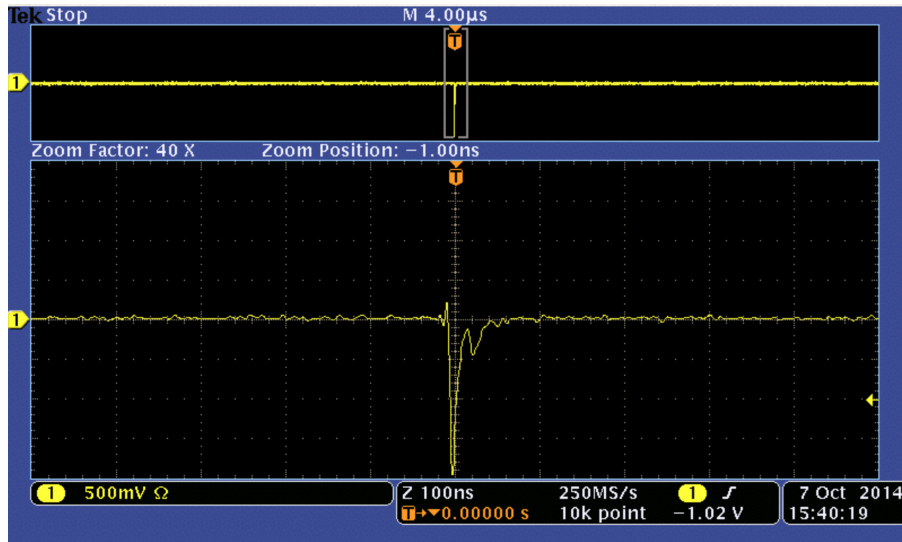


Figure 4.6: PMT RD7648 response pulse. The top and bottom signals are the same except for the enlarged scale of the bottom one.

would most likely behave correctly once glued. Also, they will be further tested with cosmic muons once glued.

## 4.2 High Voltage and Signal Threshold Voltage Measurements

The high voltage (HV) measurement and the signal threshold voltage measurement are the core measurements for a high-efficiency trigger system. The resulting HV and threshold voltage will influence the efficiency of muon detection. To be specific, if the chosen HV is higher than the value which will be best for our setup, the PMT has a higher chance of recording electrical noise. If the chosen HV is lower, the PMT is unable to detect some low energy muons. Similarly, the higher the threshold voltage value is, the less muon events are recorded; the lower it is, the more noise we record. Therefore, the purpose of the measurement is to choose the optimum values for both HV and threshold voltage.

The experimental instruments include two small scintillators (with one same model PMT each), eight big scintillators (with sixteen PMTs), all the devices introduced at the section 3.3.2. The sizes of two small scintillators are both  $25\text{ cm} \times 12.5\text{ cm} \times 2\text{ cm}$ . As mentioned in Chapter 3, the sizes of the large scintillators are all  $160\text{ cm} \times 60\text{ cm} \times 2.5\text{ cm}$ .

## 4.2.1 High voltage and threshold voltage measurement for PMT A and B

### High voltage measurement for PMT B

Measurements with the PMT A and PMT B are done first to get the optimum high voltage and discriminator threshold for each. After determining the setting parameters (HV and discriminator threshold) for PMTs A and B, the triple coincidence signals between PMTs A and B and the PMTs on the large scintillator will be measured. The HV and discriminator threshold can then be decided for the "large" PMTs to maximize the efficiency of muon counting.

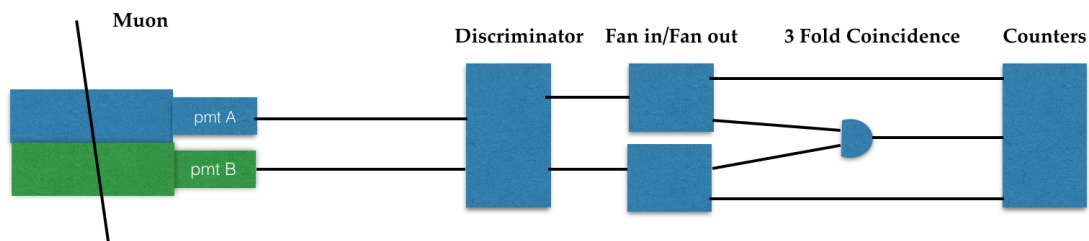


Figure 4.7: The setup for testing the high voltage settings and the threshold voltages for PMT A and B. Both PMTs are connected with the CAEN discriminator using the logic unit to create the double coincidence signal of the PMTs. The double coincidence events, PMT A events and PMT B events are counted.

The two small scintillators are laid on top of each other as shown in Figure 4.7. A double coincidence signal from PMTs A and B indicates that the signal is most likely a muon signal. Due to geometry constraints, the fraction of those cases where a muon crosses only one of the scintillators is low (estimated to be 0.4% of the total rate). Therefore, the first step is to measure the appropriate high voltages and discriminator threshold voltages for PMTs A and B. To measure the optimum HV for PMT A, PMT B's HV is fixed. Then the plot of the rates of double coincidence (PMTs A and B) is done as function of PMT A's HV. The same is done for PMT B's HV plot. The discriminator threshold voltage measurements follow the same logic. Both PMTs are connected with the CAEN discriminator using the logic unit to create the double coincidence signal of the PMTs, and then the double coincidence events are counted. Each data point takes 2 minutes to record. The result for PMT B is used as example in this section with the HV of PMT A fixed at 900 V. Notice that, the type of PMT A and PMT B is Hamamatsu R464, which are different from other 16 PMTs (Hamamatsu R329-02) on the large scintillators. The results for PMT A are in Appendix A.1.

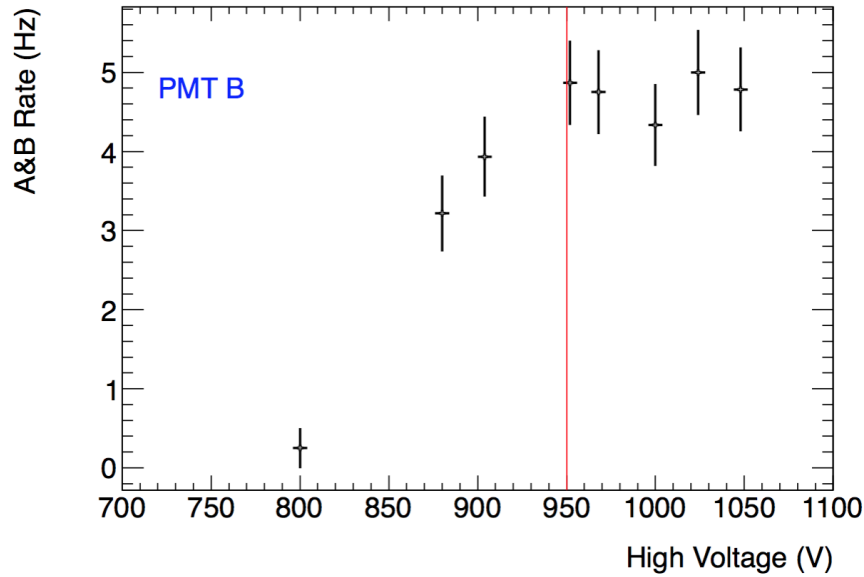


Figure 4.8: The HV curve for PMT B. The red line shows the chosen high voltage for PMT B.

As shown in Figure 4.8, for the HV measurement of PMT B, there is a turn-on curve in the plot. The value is chosen at the beginning of the plateau as our appropriate high voltage. In this case, the optimum high voltage for PMT B is 950 V as marked by the red line. Once the HV reaches 950 V, the curve reaches a plateau and the rate of the PMTs reaches and hovers around 5 Hz. Considering the size of the small scintillators ( $25 \times 12.5 = 312.5 \text{ cm}^2$ ) and the rate of the muon at sea level ( $1 \text{ min}^{-1} \text{ cm}^{-2}$ ), the measurement rate result is reasonable and convincing.

### The measurement of PMT B's HV at various values of HV for PMT A

In the previous measurements about the HV of PMT B, 900 V is chosen as fixed HV value for PMT A. To prove that the chosen fixed HV of one PMT does not influence the choice of optimum HV value for another PMT, another measurement of the rate of double coincidence at various values HV for PMT A is done. The setup of the measurement is same as before.

As shown in Figure 4.9, there are four HV curves in the plot. When the HV of PMT A is fixed at 800 V, the power is too low for PMT A to respond to some muon events, therefore the rate of double coincidence remains low in this case (0.5 Hz). For the other three curves when the HV of PMT A is above 900 V, the beginning values of the plateau are 950 V. Under the condition that the chosen value of HV for one PMT is high enough to reach the expecting rate of double coincidence (5 Hz in this case) for different values of the HV value of another PMT, the chosen fixed HV value of one PMT

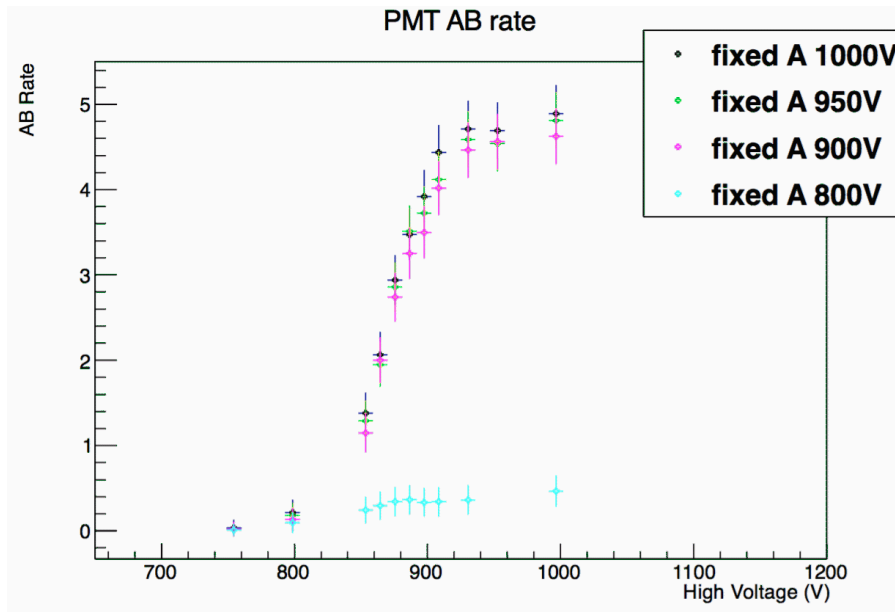


Figure 4.9: The HV curve for PMT B at different HV values for PMT A.

does not affect the result of optimum HV value for another PMT.

### The threshold voltage for PMT B

Similar to the HV measurement, for PMT B's threshold voltage, the threshold voltage of PMT A is fixed at three different values (1 mV, 5 mV, 7 mV), based on possible noise levels.

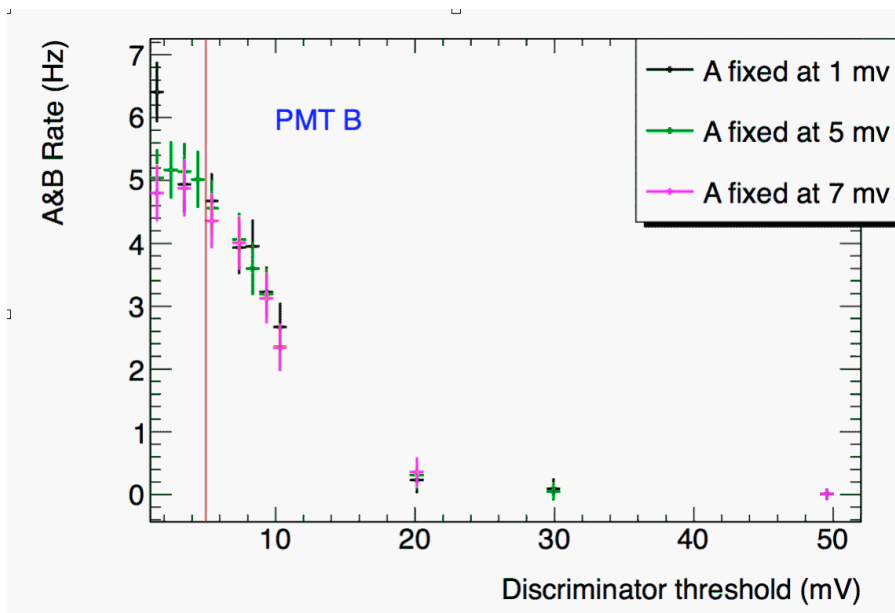


Figure 4.10: The threshold voltage curve for PMT B at different threshold voltages for PMT A.

As shown in Figure 4.10, the chosen value of threshold voltage for PMT A has no significant

influence on the threshold voltage curves of PMT B. The choices about fixed threshold voltage value of PMT A won't affect the result of threshold voltage for PMT B. Similarly, the plot of discriminator thresholds starts with a flat curve with a rate of about 5 Hz, and then begins to decrease after the 5 mV point. The value at the end of the plateau is chosen as our appropriate discriminator threshold voltage. In this case, the discriminator threshold for PMT B is 5 mV. The same process as for PMT B is applied on PMT A. The HV and discriminator thresholds for PMT A are 1000 V and 5 mV respectively. The result for both PMTs is shown in Table 4.3.

PMT	HV(V)	Threshold Voltage(mv)
A	1000	5
B	950	5

Table 4.3: The HV and threshold voltage results for PMT A and B.

#### 4.2.2 High voltage and signal threshold voltage measurement for PMTs on the large scintillators

Once the appropriate high voltage and discriminator thresholds for PMT A and PMT B are chosen, we apply the same method of measurement for all the PMTs on the large scintillators. As shown in Figure 4.11, during this measurement, the two small scintillators are placed on top of a large scintillator. The block diagram for the measurement is shown in Figure ??, the double coincidence of PMT A and B is used as reference for the muon signal. the triple coincidence of PMT A and B and one PMT in the large scintillator are measured. The spacing between room ceiling and top scintillators, as well as the spacing between the bottom layer of the hodoscope and bottom scintillators are small (see Figure 3.2 and Figure 3.6). Therefore, because of space constraints in the lab, it was not practical to place two small scintillators above the middle portion of the large scintillator (except for PMT NTWO and PMT STWO).

For the discriminator threshold test, we use PMT NTWO and PMT STWO as examples. Since the scintillator these PMTs are attached to is on the edge of the structure, two small PMTs can be placed

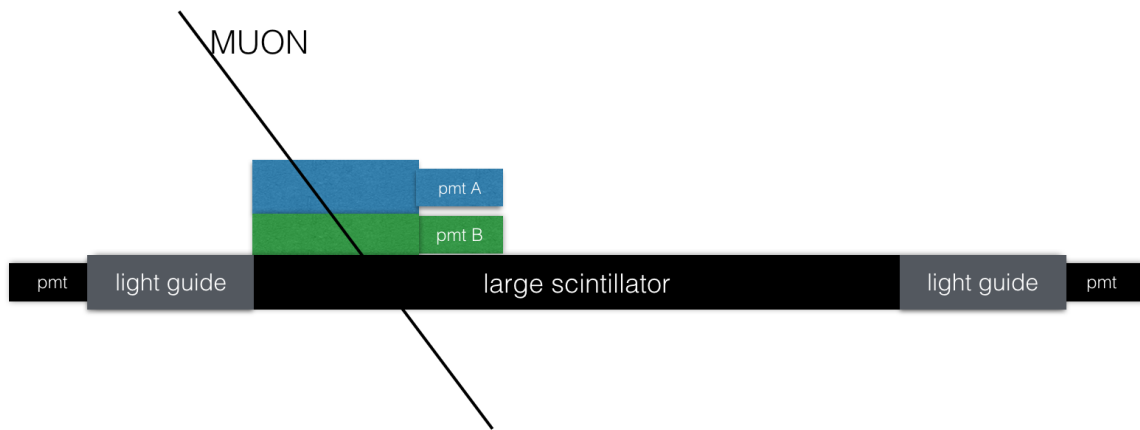


Figure 4.11: The sectional view of the setup for high voltage and threshold voltage measurements for the PMTs of the large scintillators. The figure is used to present the relative positions and is not to size. The PMT is slightly thicker than the lightguide in the lab.

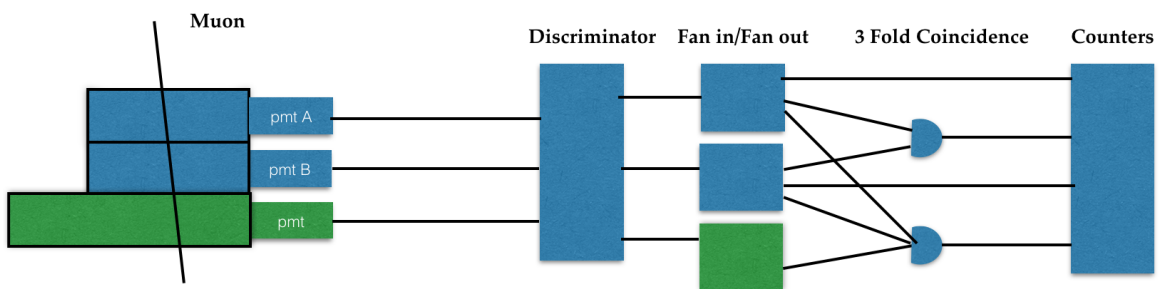


Figure 4.12: The block diagram shows the operating principle for high voltage and threshold voltage measurements for the PMTs of the large scintillators.

on three different positions (both ends and middle) on the scintillator for the threshold voltage. The results are shown in Figure 4.13.

The result shows that there is no significant difference for the discriminator threshold curve as a function of the position of two small PMTs. To be specific, though the chosen measured area of the scintillator influences the rate of triple coincidence, it has no influence on the shape of the appropriate discriminator threshold curve. In this case, the red line refers to the threshold voltage for PMT A and B, both set at a 5 mV. NTWO has 5 mV threshold voltage and STWO has a 7 mV threshold voltage. The same method are applied on the other PMTs. The full results are shown in Appendix A.1.

For all HV tests, the two small scintillators were placed at two different positions on the large

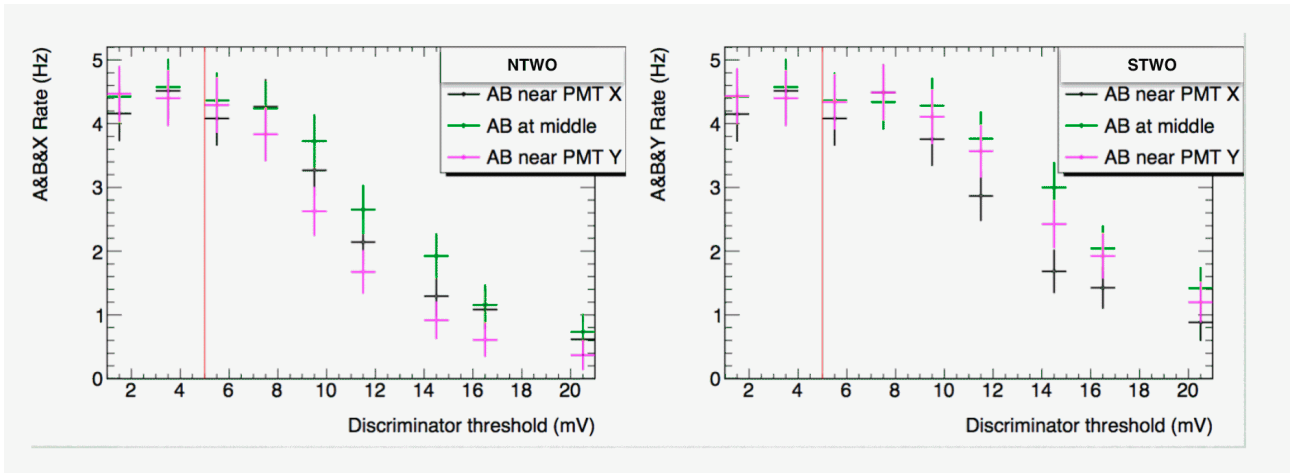


Figure 4.13: The discriminator threshold plots for NTWO and STWO. The red lines refers to the discriminator threshold voltages for PMT A and B.

scintillator (north edge and south edge).

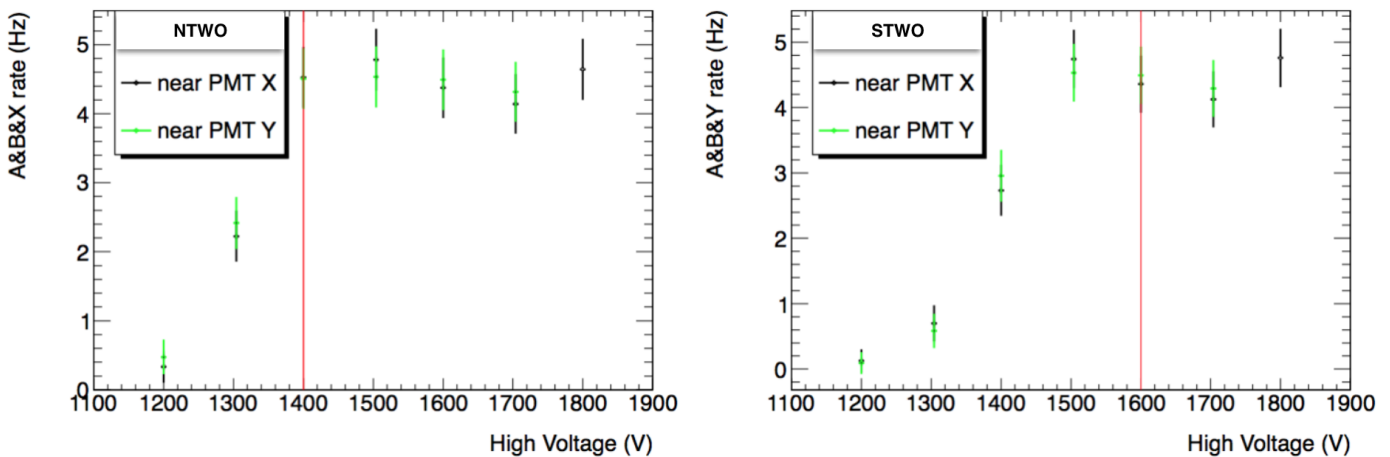


Figure 4.14: The HV plots for NTWO and STWO. The red lines indicate the initial chosen values.

As shown in Figures 4.14, similar to the HV plots of PMT A and B (Figure 4.8), a turn-on curve is followed by a plateau. In this case, the red line refers to the chosen HVs for NTWO and STWO where the plateau starts. The final high voltage and discriminator thresholds of the 16 PMTs are shown in Table 4.4. Since fluctuations are small and to be consistent, 5 mV is chosen for all PMTs. Results for all PMTs are attached in Appendix A.2 (HV) and A.3 (threshold).

The uncertainty in the plots is defined as following. Each time PMTs detect a muon event, the number of muons that actually reacted with the scintillator to produce that event follows a Poisson distribution. If  $N_A$  stands for the counts of double coincidence "PMT A and PMT B" events (or triple

Location	Scintillator	Lightguide location	Lightguides	PMTs	HV	discriminator(mv)
Top West Outer	#6003-01-07	South	#6003-02-07	RD7589	1500	5
		North	#6003-02-08	RD7693	1700	5
Top West Inner	#6003-01-06	South	#6003-02-04	RD7703	1600	5
		North	#6003-02-03	RD7702	1400	5
Top East Inner	#6003-01-05	South	#6003-02-16	RD7688	1600	5
		North	#6003-02-15	RD7574	1600	5
Top East Outer	#6003-01-08	South	#6003-02-12	RD7697	1600	5
		North	#6003-02-11	RD7649	1600	5
Bottom East Outer	#6003-01-04	South	#6003-02-01	RD7648	1700	5
		North	#6003-02-02	RD7677	1700	5
Bottom East Inner	#6003-01-03	South	#6003-02-06	RD7639	1600	5
		North	#6003-02-05	RD7682	1600	5
Bottom West Inner	#6003-01-02	South	#6003-02-09	RD7665	1500	5
		North	#6003-02-10	RD7692	1500	5
Bottom West Outer	#6003-01-01	South	#6003-02-14	RD7651	1700	5
		North	#6003-02-13	RD7644	1400	5

Table 4.4: The operation HVs and threshold voltages for all PMTs.

coincidence "PMT A, PMT B and large scintillator PMT" events) and  $N_B$  stands for the counts of single hit "PMT A or PMT B" (or double hits "PMT A and PMT B"), the uncertainty of the counts are  $\sqrt{N_A}$  and  $\sqrt{N_B}$ . The calculated uncertainty of the rate is  $(\frac{\sqrt{N_A}}{t_A})$ , where  $t_A$  refers to the time interval. The efficiency is  $\frac{N_A}{N_B}$ , therefore, the uncertainty of the efficiency is  $\sqrt{\frac{N_A}{N_B^2} + \frac{N_A^2}{N_B^3}}$  (see Section 4.3). The details are shown in the Appendix B. However, when  $N_A$  is close to  $N_B$ , the uncertainty of efficiency can not be described by  $\sqrt{\frac{N_A}{N_B^2} + \frac{N_A^2}{N_B^3}}$ . therefore, the Bayesian statistics way to calculate the uncertainty of the efficiency is applied [64].

$$\sigma\left(\frac{Rate_A}{Rate_B}\right) = \sqrt{\frac{(N_A + 1)(N_A + 2)}{(N_B + 2)(N_B + 3)} - \frac{(N_A + 1)^2}{(N_B + 2)^2}} \quad (4.1)$$

### 4.2.3 Summary

All PMTs have been successfully tested; they operate well. Cross checks were performed for different positions along the scintillator and for different discriminator thresholds. The HV and discriminator threshold values for all PMTs were determined to achieve the maximum efficiency. The trigger system of the hodoscope is ready for work.

## 4.3 Scintillator Efficiency Measurements

### 4.3.1 Efficiency vs. HV and signal threshold voltage measurements

Because of electrical damage, the CAEN discriminator was disabled from December 2014 to June 2015. During this time, we used the LeCroy 623B discriminator. The efficiency vs position measurements and efficiency vs time measurements were both done with LeCroy 623B discriminator.

Since the discriminator is changed from CAEN to LeCroy 623B, the HV and threshold voltage measurements in subsection 4.2.2 needed to be redone. The setup table is shown in the Appendix A.4.

After the CAEN discriminator was repaired in June 2015, all the PMTs were re-tested again. To lower the uncertainty for each data point, runs of 5 minutes instead of 2 minutes were taken to record the amount of the triple and double coincidence events. The efficiency is defined as follow.

$$\text{Efficiency} = \frac{\text{The triple coincidences signal (ABX)}}{\text{The double coincidence signal (AB)}} \quad (4.2)$$

The X refers to one of the PMTs from the large scintillators. The rate of incident muon is considered as constant ( $1/\text{cm}^2/\text{min}$ ) with small uncertainty, The triple coincidence rate is influenced by the exact rate of muon events during the measurement period. Since the triple coincidence and the double coincidence are correlated. From Equation 4.1, it is easily proved that the uncertainty in the efficiency is smaller than the correlate uncertainty  $\sqrt{N_A}/N_A$  in rate of events.

Higher numbers of data points with threshold voltage between 0 and 20 mV are also chosen in the new discriminator threshold voltages measurements. Two small PMTs (PMT A and PMT B) were attached to the upper and lower surfaces of the large scintillator. The previous placement method 4.1.1 caused a loss of muon events at large angles. Some muons may cross the small scintillators without passing the large scintillator. Instead of placing both two small scintillators on the top surface of the large scintillator, one small scintillators is placed on the top surface of the large scintillator, another one is touched to the bottom surface of the large scintillator. The setup is shown in Figure 4.15. The new method avoids this situation, improving the accuracy of the data. However, due to the inconvenience of this setup, we only use this setup for the efficiency test vs. HV measurement at one position.

The other steps of the measurement are the same as for the HV and threshold voltage measurements in Section 4.2.1. The results from Figure 4.16 for the PMTs on the TWO scintillator is used as example:

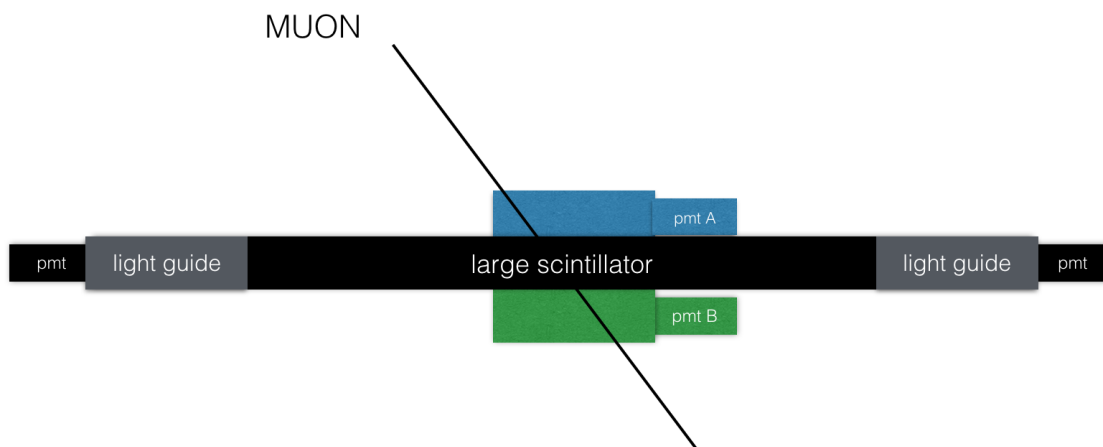


Figure 4.15: The scintillator efficiency vs. HV and threshold voltage measurements for TWO. The block diagram for the measurement is the same as in Figure 4.12.

the results for other PMTs are in the Appendix A.

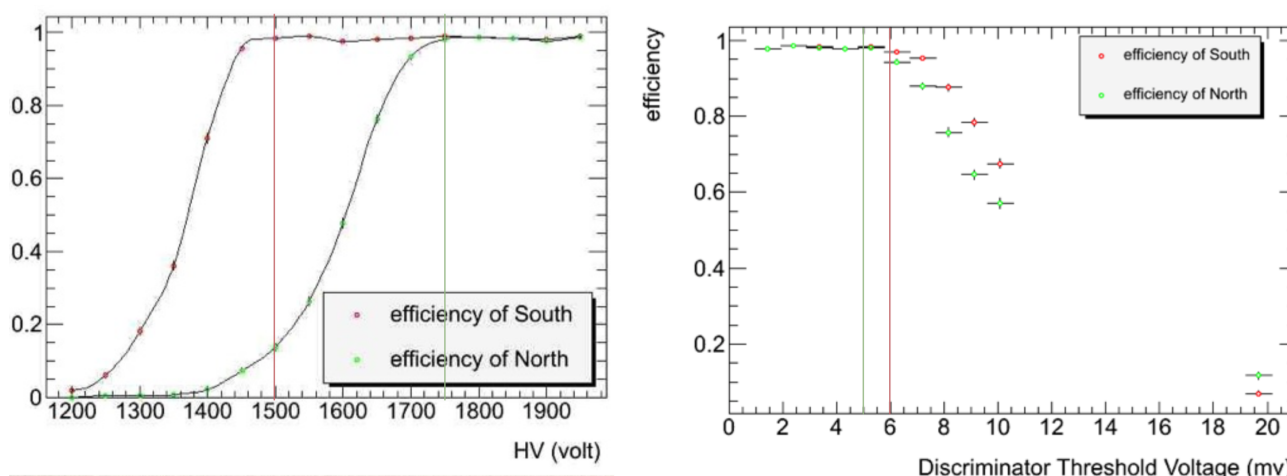


Figure 4.16: The efficiency vs. HV and threshold voltage measurements for the PMTs on the TWO scintillator.

The results for HV and threshold voltage of all PMTs are shown in Table 4.5. Comparing Table 4.5 with Table 4.4, there is no significant difference in the high voltage setting. For some PMTs, the high voltage setting have been increased by 50V or 100 V. For some other PMTs, the high voltage setting have been decreased by 50V. The variations may be caused by the aging of the PMTs in the 4 months or the improvement of the measurement method for the position of PMTs A and B. According to the results of this new measurement, the discriminator thresholds are only slightly different for each PMT. As shown in Figure 4.16, the discriminator threshold voltages for both PMTs are closed to 5 mV. It is similar for all other PMTs. To be consistent, the discriminator threshold voltages for all PMTs are

chosen to be 5 mV.

Location	Scintillator	Lightguide location	Lightguides	PMTs	HV
TWO	#6003-01-07	South	#6003-02-07	RD7589	1500
		North	#6003-02-08	RD7693	1750(+50)
TWI	#6003-01-06	South	#6003-02-04	RD7703	1500
		North	#6003-02-03	RD7702	1500(+100)
TEI	#6003-01-05	South	#6003-02-16	RD7688	1450(-50)
		North	#6003-02-15	RD7574	1600(+100)
TEO	#6003-01-08	South	#6003-02-12	RD7697	1650(+50)
		North	#6003-02-11	RD7649	1450(-50)
BEO	#6003-01-04	South	#6003-02-01	RD7648	1600
		North	#6003-02-02	RD7677	1650(+50)
BEI	#6003-01-03	South	#6003-02-06	RD7639	1500
		North	#6003-02-05	RD7682	1550(+50)
BWI	#6003-01-02	South	#6003-02-09	RD7665	1500
		North	#6003-02-10	RD7692	1600
BWO	#6003-01-01	South	#6003-02-14	RD7651	1650(-50)
		North	#6003-02-13	RD7644	1450(+50)

Table 4.5: The setup of HVs for all PMTs. The names of the locations are abbreviations of the names from Table 4.4. The chosen HV for each PMT is shown in the table. The red color and green color numbers show the changes in HV from the preview setup (Table 4.4) to the new setup.

### 4.3.2 Efficiency vs. position measurements

Though the HV and threshold voltage measurements at two (or three) areas of the scintillator in subsection 4.2.2 roughly prove that efficiency is not influenced by position, it would be more convincing if we could obtain the same conclusion from more specific efficiency vs. position measurements.

Therefore, in this section, efficiency vs. position measurement is introduced. As mentioned in subsection 4.3.1, the efficiency vs position measurements and efficiency vs time measurements was done with LeCroy 623B discriminator. Two small PMTs (PMT A and PMT B) and the large PMTs NTWO (which we will refer to simply as N) and STWO (S) are used in those measurements. The measurement method is as follows. Firstly, the two small scintillators are placed at more location above the large scintillator with the same HV and threshold voltages setup. Secondly, the double coincidences, triple coincidences and quadruple coincidences are measured. Finally, the efficiencies are calculated. In the measurements, double coincidences refer to the coincidence signal of PMT A and B; similarly, quadruple coincidences mean that PMTs A, B, S, and N all give a signal. There are three kinds of triple coincidences PMTs A, B, and N; PMTs A, B, and S; and PMT A, B, and either N

or S. The efficiency in the measurement is defined as

$$\text{Efficiency} = \frac{\# \text{ of triple (or quadruple) coincidences}}{\# \text{ of double coincidences}} \quad (4.3)$$

It is similar to Eq. 4.2 with additional definition of quadruple coincidences over double coincidences.

At the beginning, only a quick study of the relation between position and efficiency is required. Therefore, 7 areas are chosen on the middle band from the south edge to the north edge of the scintillator in Figure 4.17.

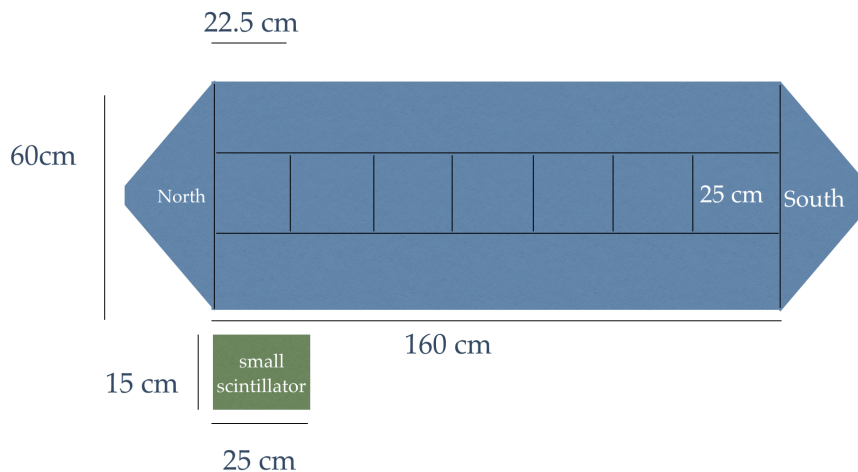


Figure 4.17: The top view about how scintillator is divided.

For each area, the quadruple coincidence, the triple coincidences and the double coincidence are measured. The result is shown in Figure 4.18.

In all figures shown in this subsection 4.3.2, the abscissa axis refers to the position of the south edge of PMTs A and B with respect to the south edge of the scintillator.

The triple coincidences have consistent high efficiency along the different areas. However, the result shows an unexpected dip in the curve for the quadruple coincidence efficiency.

To better understand this behaviour, we repeat this measurement with more positions.

As shown in Figure 4.19, the large scintillator is divided equally into 12 areas along the middle band. At five-inch intervals, the quadruple, triple, and double coincidences are measured.

As shown in Figure 4.20, The triple coincidences, PMT A and PMT B and PMT (either N or S), is not measured in this case. The efficiency of quadruple coincidence still show a dip in the curve.

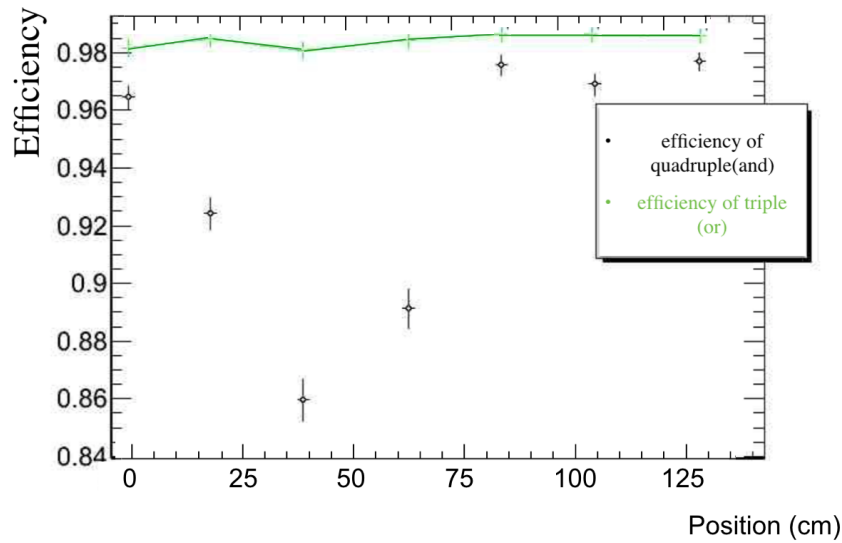


Figure 4.18: The efficiency of quadruple and triple coincidences vs. position measurements. The "AND" and the "OR" describes the logic relations between PMT N and PMT S. A large scale offset was put in the ordinate.

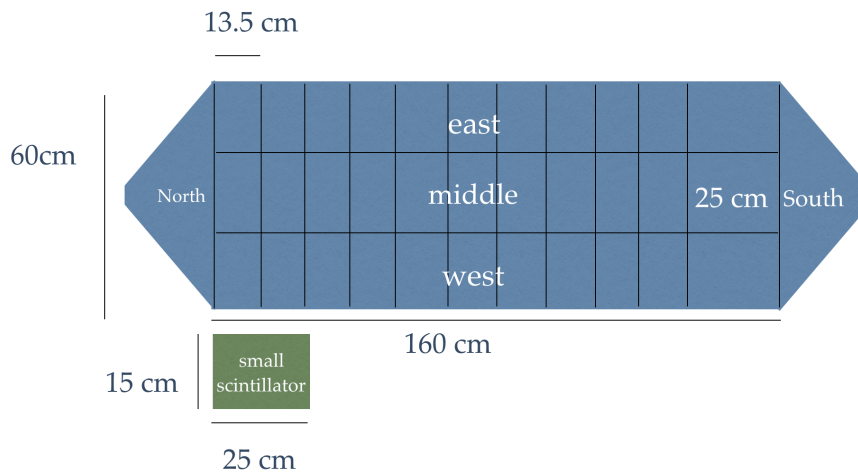


Figure 4.19: The top view about how scintillator is divided.

Careful analysis of the shapes in Figure 4.18 and 4.20 yield approximately the same minimum position.

In Figure 4.21, the behavior of PMT S is reasonable with high and stable efficiency. But PMT N produces a similar concave curve as before. Therefore, lower efficiency of PMT N at the center of the scintillator is the source of the dip.

Therefore, one assumption is that the chosen HV of PMT S is not accurate, since those measurement were only done in two positions at each end of the scintillator (Figure 4.14). HV curves were made for

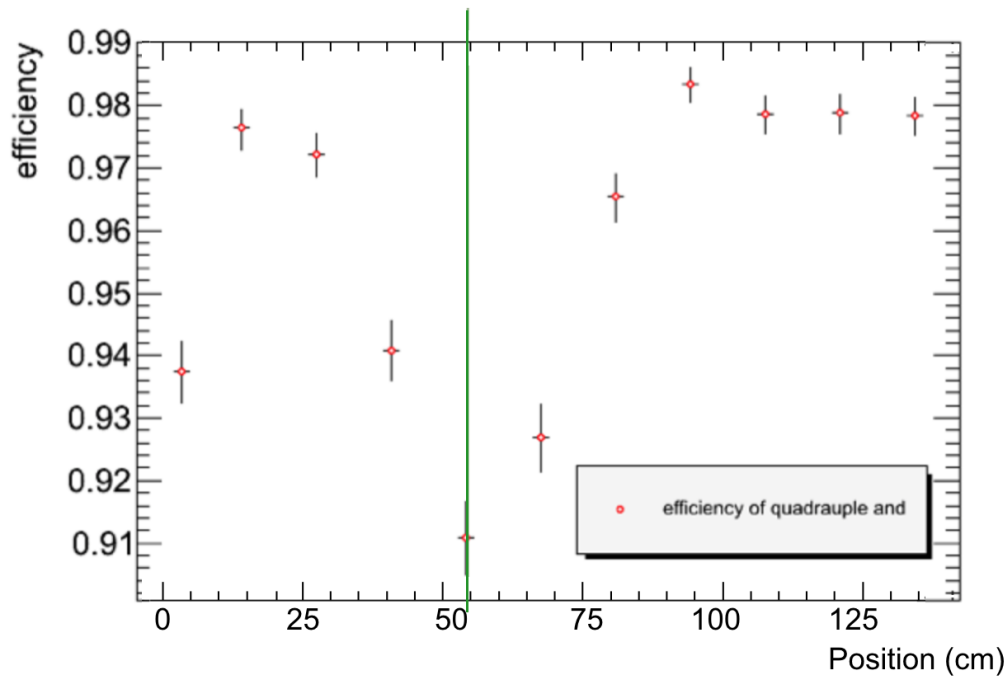


Figure 4.20: The efficiency of quadruple coincidence for PMTs A $\wedge$ B $\wedge$ S $\wedge$ N.

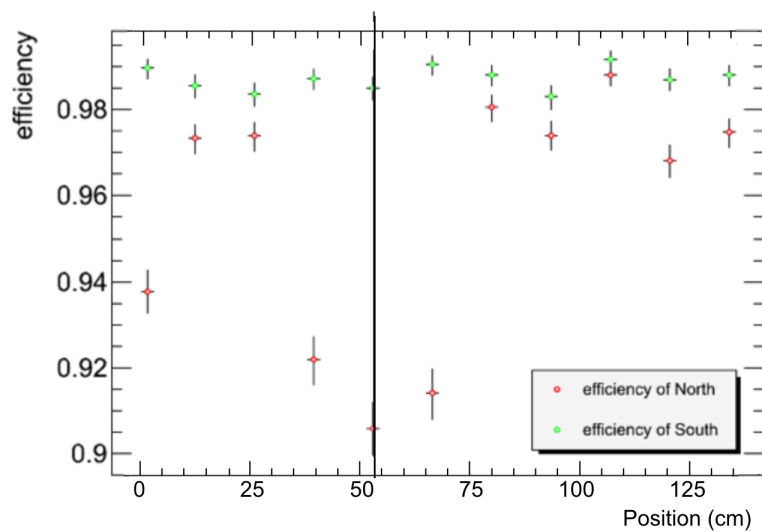


Figure 4.21: The efficiencies from triple coincidences of PMTs A $\wedge$ B $\wedge$ S and PMTs A $\wedge$ B $\wedge$ N.

PMTs S and N when the small PMTs were placed at three different positions (north, middle and south). The results are shown in Figure 4.22.

In Figure 4.22, for PMT S, all three curves behaved consistently. However, when the small PMTs are placed in the middle, the PMT N curve does not reach a plateau when the HV is 1700 V as the

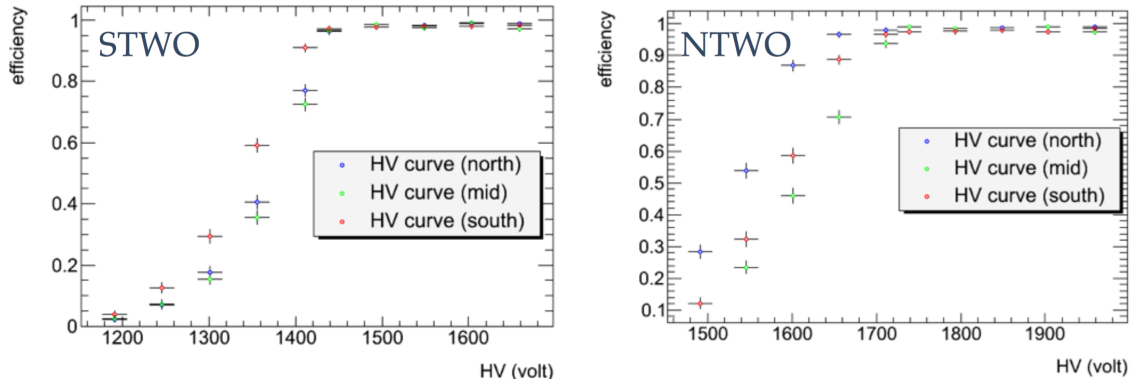


Figure 4.22: The efficiency vs. HV when PMT S and PMT N are powered on different HVs.

north and south curves do. As mentioned in section 4.2. The chosen value of HV for PMT should be on the plateau, therefore, one solution is raising the setting of HV from 1700 V to 1750 V.

After increasing the HV of PMT N, efficiencies are satisfying for both quadruple and triple coincidences shown as Figure 4.23 and 4.24 respectively. The triple coincidences result for PMT STWO is in the Appendix A.5.

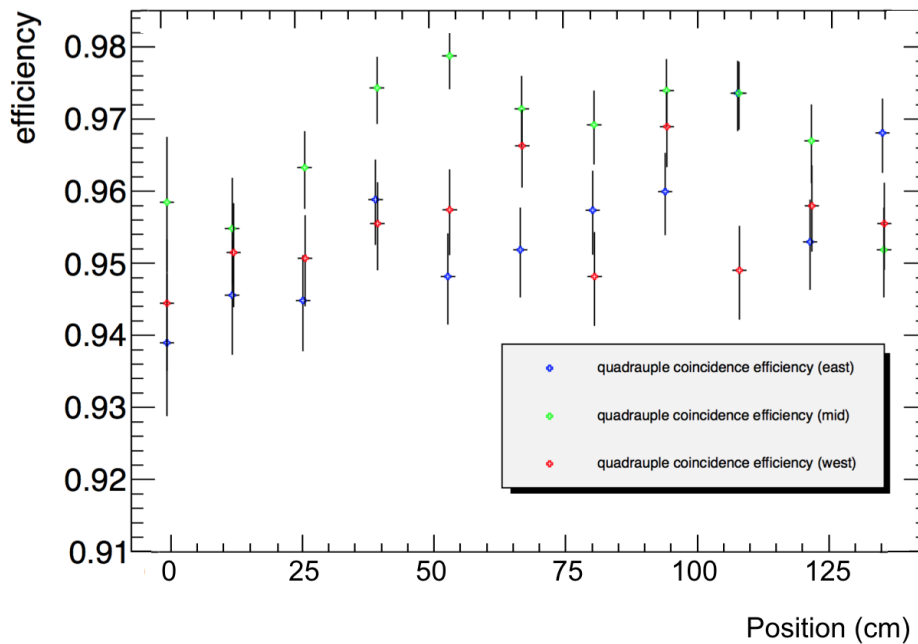


Figure 4.23: The efficiency of quadruple coincidences for PMTs  $A \wedge B \wedge S \wedge N$  at different positions along the large scintillator .

However, an explanation for the curve dip is still required. It appears that the farther away from a PMT a muon hits the scintillator, the lower the efficiency of the triple coincidence (PMTs  $A \wedge B \wedge S$  or

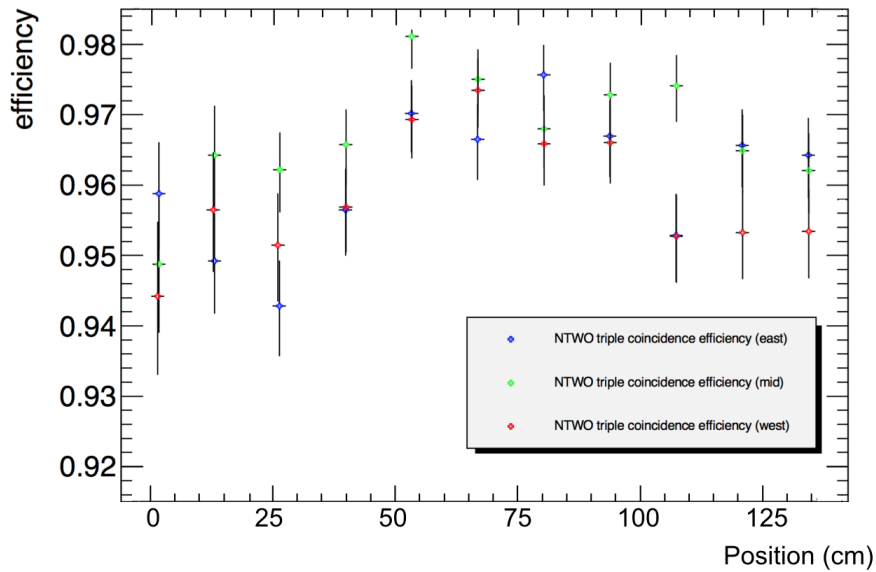


Figure 4.24: The efficiency of triple coincidences for PMTs A $\wedge$ B $\wedge$ N.

PMTs A $\wedge$ B $\wedge$ N) related to this PMT is. As a conclusion, ideally, the quadruple coincidences should have higher efficiency at the middle of the scintillator than close to a PMT. But it is not in accord with the observations. Since the time difference between the signals from PMTs N and S is short, the quadruple efficiency is not reduced [65]. The one explanation might be that due to the reflection angle inside the scintillator, muons of a given energy will produce a higher amplitude electrical signal at the edge than at the middle. This requires that we simulate the response of the scintillator and PMTs when a muon crosses the scintillator, as will be explained in Chapter 5. A low energy muon crossing the middle of the scintillator cannot lead to an electric signal above the threshold voltage, whereas it might have been able to if it had crossed the edge of the scintillator along the lightguide. The amplitude is influenced by the high voltage. Therefore, when the HV of the PMT is not high enough, the differences of amplitudes between PMTs S and N might be significant.

Due to time and space limits, HV vs. position curves for every PMTs were not done. However, quadruple and triple coincidence efficiencies for each scintillator are measured where the two small PMTs are placed in the middle (which is the area of lowest efficiency from Figure 4.22). The results are shown in Table 4.6. The time window is 10 minutes. All efficiencies are above 95%.

Scintillator	Quadruple coincidence	Double coincidence (AB)	Efficiency	Triple coincidence	Double coincidence (AB)	Efficiency
TWO	2334	2420	96.45±0.38%	2373	2418	98.14±0.28%
TEO	2632	2705	97.4±0.31%	2549	2596	98.19±0.26%
TEI	2569	2623	97.94±0.28%	2551	2603	98±0.28%
TWI	2518	2559	98.4±0.25%	2536	2567	98.8±0.22%
BWO	2426	2470	98.22±0.27%	2468	2502	98.64±0.23%
BWI	2334	2446	95.43±0.42%	2443	2478	98.59±0.24%
BEI	2366	2394	98.83±0.22%	2262	2293	98.65±0.24%
BEO	2516	2551	98.62±0.23%	2479	2509	98.8±0.22%

Table 4.6: The table for the quadruple and triple coincidence efficiencies (PMTs  $A \wedge B \wedge (S \vee N)$ ) for each scintillator. The uncertainty is calculated by Eq. 4.1.

### 4.3.3 Efficiency vs. recording time measurement

When turned on, a PMT needs some time (called start-up time in this subsection) to stabilize to its setting. To be specific, each time we reset the HV of the PMT, it requires some time for the PMT to stabilize under the new HV setting. Therefore, if we start our measurement, results may not be accurate. A simple measurement is designed to test if the start-up time is significant enough to influence our measurements.

PMTs A, B, and NTWO are used in this measurement. The two small PMTs are placed on the north side of the scintillator (near PMT NTWO). The definition of efficiency is same as the equation 4.2.

$$\text{The efficiency} = \frac{\text{The triple coincidences signal (ABN)}}{\text{The double coincidence signal (AB)}} \quad (4.4)$$

According to Table 4.5, the setting HV of NTWO is 1750V. The efficiency is recorded as a function of time, starting from the moment the HV reaches 1750 V after ramp-up and ending one hour after. The time duration for each data point is 2 minutes and data is taken every 5 minutes.

As shown in Table 4.7, all the efficiencies are high (close to 100 %) throughout. Therefore, the relax time of the PMT is relatively short. The measurement results are not influenced by the time interval between the moment data is collected and the moment when the PMT is fully powered at 1750 V from 0 V.

Time (minute)	Double coincidence	Triple coincidence	Efficiency
0	453	453	$100_{-0.22}^{+0} \%$
5	443	443	$100_{-0.22}^{+0} \%$
10	438	440	$99.55 \pm 0.39 \%$
15	480	481	$99.79 \pm 0.21 \%$
20	422	423	$99.76_{-0.33}^{+0.24} \%$
25	432	433	$99.76_{-0.32}^{+0.24} \%$
30	475	477	$99.58 \pm 0.36 \%$
60	435	435	$100_{-0.22}^{+0} \%$

Table 4.7: The table of double and triple coincidence vs. waiting time.

## 4.4 Time Difference Measurements

To complete the work of a summer student [65], two measurements related to the time difference in the trigger system are performed. The time difference is defined as the time interval for two PMTs in our trigger system to respond to one muon event. The first one is the time resolution of measurements with two small PMTs (PMT A and B). Two small scintillators were firstly placed, one on the middle of the TWO scintillator (PMT A) and the other on the middle of the BWO scintillator (PMT B) as shown in Figure 4.25.

The time difference between TWO (NTWO  $\vee$  STWO) and BWO (NBWO  $\vee$  SBWO) are measured. Four different trigger systems are set as follow.

1. The signal of TWO (NTWO  $\vee$  STWO)  $\wedge$  BWO (NBWO  $\vee$  SBWO)  $\wedge$  PMT A  $\wedge$  PMT B as trigger signal.
2. The signal of TWO (NTWO  $\vee$  STWO)  $\wedge$  BWO (NBWO  $\vee$  SBWO)  $\wedge$  PMT A as trigger signal.
3. The signal of TWO (NTWO  $\vee$  STWO)  $\wedge$  BWO (NBWO  $\vee$  SBWO)  $\wedge$  PMT B as trigger signal.
4. The signal of TWO (NTWO  $\vee$  STWO)  $\wedge$  BWO (NBWO  $\vee$  SBWO) as trigger signal.

For each group, we take 500 data points. The different setup controls the range of traces of muons. For example, since two small scintillators are both placed on the middle of the scintillators, the first group

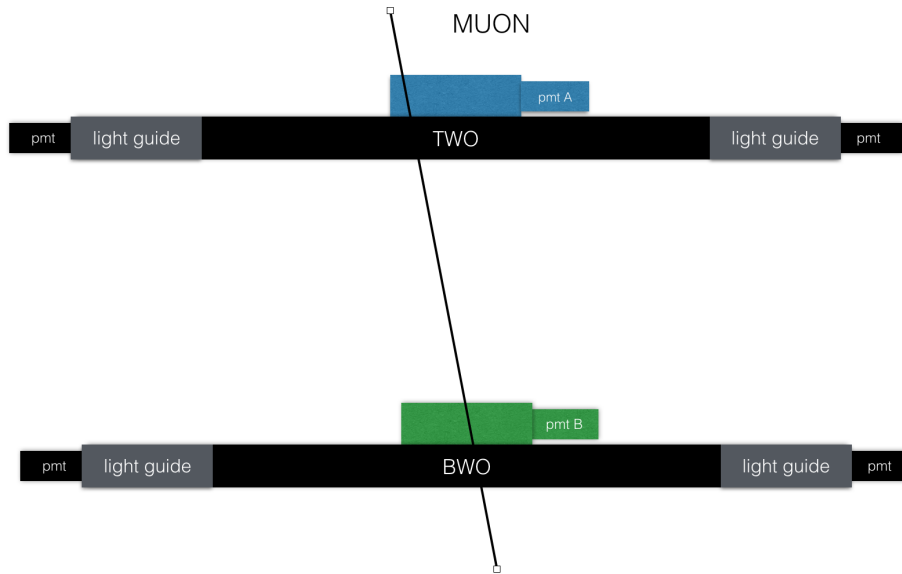


Figure 4.25: The setting up for the time difference for WO. The block diagram for the measurement is the same as in Figure 4.12.

of measurements provides the time difference of Top and Bottom when muon crosses the middle of the scintillators. If the range of tracks is narrower, the result for the range of time differences is also narrower. The results are shown in Figure 4.26.

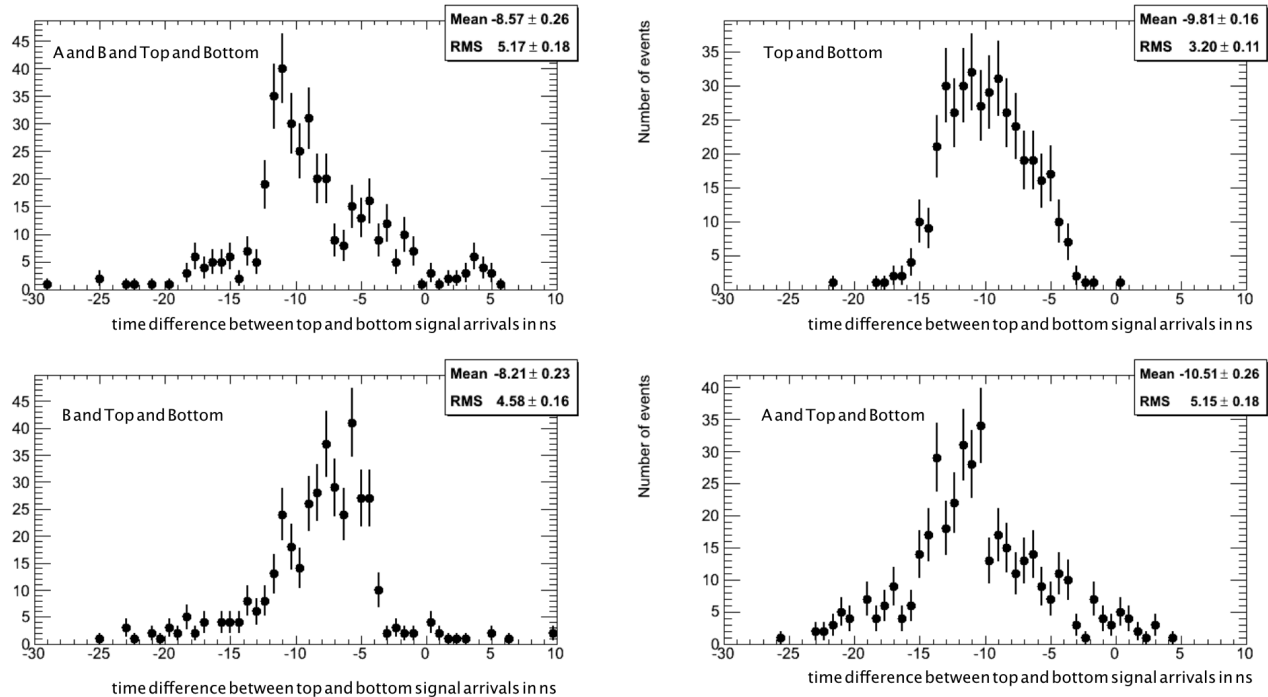


Figure 4.26: The results for time differences between top and bottom signal arrivals under 4 different kinds of angle constraint.

As shown in Figure 4.26, if the range of traces is narrower, the result for the range of time different is also narrower. In other words, the result proves that we got more precise time resolution results in measurements which two small PMTs were involved. Therefore, the time resolution for TWO and BWO is about  $8.57 \pm 5.17\text{ns}$ .

The second measurement is the time difference between any PMT from any four Top scintillators (TWO, TWI, TEI, TEO) and any PMT from any four Bot scintillators (BWO, BWI, BEI, BEO). Using logic units, the trigger is set to give a signal when at least one Top and one Bot scintillator give signals.

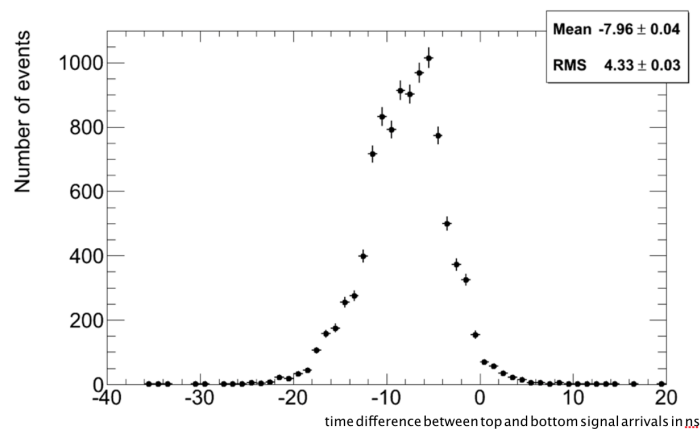


Figure 4.27: The time difference between all four Top scintillators and all four Bottom 4 scintillators.

In the Figure 4.27, the results gives the mean of time resolution for our trigger system ( $7.96 \pm 4.33$  ns).

## Chapter 5

---

# Crosstalk Measurements

---

Crosstalk occurs when a signal transmitted on one channel of a system induces a inductive signal in another channel. Crosstalk is a source of background in our trigger system, since it may register false events in the data acquisition (DAQ) system. Therefore, the real efficiency is lower than the measured efficiency if crosstalk does exist in our system. To lower the uncertainty of the results and increase the efficiency of the system, crosstalk needs to be minimized as much as possible.

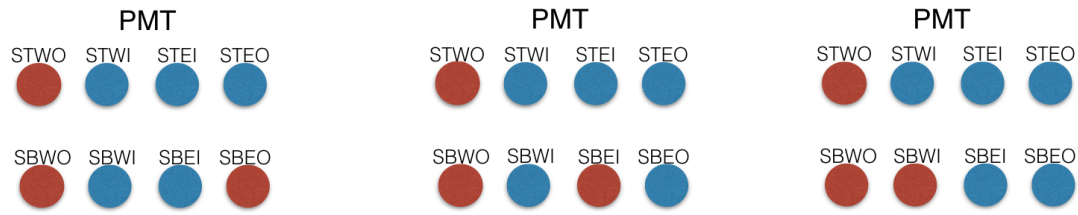
### 5.1 The Observation of Triple Coincidences

The first step is to set up measurements to record the rate of triple coincidences of PMTs which geometrically are unable to be provided by the same muon event. If the rate of triple coincidence is zero, crosstalk could be considered as negligible in the trigger system. Therefore, three groups of triple coincidences measurements are done. As shown in Figure 5.1, the first group of data comes from the triple coincidence of STWO, SBWO, and SBEO. The second comes from that of STWO, SBWO, and SBEI. The third comes from that of STWO, SBWO, and SBWI. The time scale for each data point is 2 minutes. Each measurement is repeated 6 times.

The double coincidences of PMTs STEO and SBEO are also measured for each point to calculate the ratio of triple coincidences.

The measurements results are shown in Figure 5.1.

In all three groups, the efficiencies were all low. It means that the triple coincidence happens rarely compared to double coincidence. Therefore, even if those triple coincidences are crosstalk signals.



	Double Coincidence	Triple Coincidence	Efficiency(%)	Double Coincidence	Triple Coincidence	Efficiency(%)	Double Coincidence	Triple Coincidence	Efficiency(%)
	1529	12	0.78±0.23	1519	9	0.59±0.21	1597	20	1.25±0.28
	1572	8	0.51±0.19	1641	12	0.73±0.22	1535	24	1.56±0.32
	1558	18	1.12±0.28	1618	11	0.67±0.21	1514	19	1.25±0.29
	1597	11	0.69±0.22	1667	13	0.77±0.22	1537	20	1.3±0.30
	1605	15	0.93±0.25	1540	10	0.64±0.21	1636	17	1.04±0.26
	1501	3	0.20±0.13	1607	15	0.93±0.25	1580	14	0.89±0.24
<b>Mean</b>	1560.3±16.3	11.2±2.2	0.71±0.14	1598.7±23.6	11.7±0.9	0.72±0.05	1566.5±16.8	19±1.4	1.22±0.1

Figure 5.1: The results of crosstalk checking measurement. The round dots identify the all PMTs on the north side of the trigger system. The red ones identify the PMTs related to the measurements, the blue ones identify the other PMTs(turn off). The double coincidences and triple coincidences were measured. The efficiencies defined as Equation 4.2 were calculated. The definition of uncertainties follows Equation 4.1.

They won't cause huge influence on the efficiency of our system. However, it is still important to identify the source of those triple coincidence. The rates of triple coincidences are  $5.51 \pm 1.08$  per minute for the first group,  $5.83 \pm 0.44$  per minute for the second group,  $9.5 \pm 0.68$  per minute for the third group. For the third group, because the two bot scintillators are placed besides each other, the source of the triple coincidence could be the same muon crossing the scintillators at a special angle since PMTs SBWO and SBWI are next to each other (shown in Figure 5.1). Therefore, the rate of the triple coincidence is higher for the other two groups. However, even for the triple coincidence rates of the first and second groups are not zero. Though the ratio of the triple coincidence to the double coincidence is too low to justify changing our settings, it is still necessary to understand the source of the triple coincidences.

## 5.2 Calculation of Number of Double Muons Events

Since the triple coincidences are measured, they could be two muons crossing scintillators at the same time, apparently as crosstalk events. Before the crosstalk measurements are done, the number of double

muon events should be calculated and be used to compare with the measurement results of the triple coincidence later. The times when a muon crosses two scintillators attached to the PMTs STWO and SBWO while another muon crosses the scintillator attached to PMT STEO in 10 minutes are measured. The set up is shown in Figure 5.2. The three scintillators involved in triple coincidence calculation are marked as blue in the Figure. To be concise, the scintillator will have the same labels as the PMT they are attached to in this section. The steps are as follow:

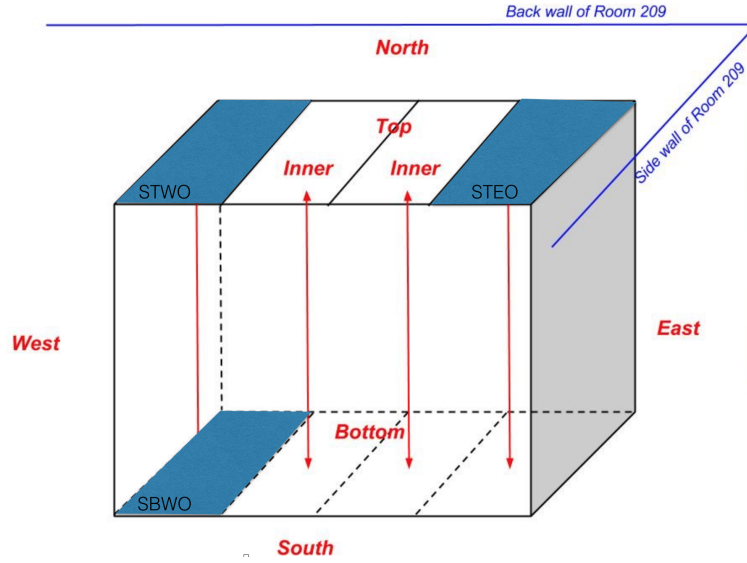


Figure 5.2: The set up of triple coincidence. The blue parts identify the scintillators related to the measurements. PMTs on the south of those scintillators were turned on.

1. Firstly, a muon "a" crosses scintillator STEO at  $t = 0$ ns.
2. Secondly, to produce a triple coincidence, another muon B need to crosses both STWO and SBWO in a time period  $T_w$ ,  $T_w$  is calculated from the width of output signal from the discriminator  $T_d$  (37ns) minus the minimum overlap time  $T_m$  (3 ns) required for "and" logic unit [58].

$$T_w = T_d - T_m = 37 - 3 = 34\text{ns}$$

The probability that muon B crosses both STWO and SBWO in  $0 \text{ ns} < t < T_w = 34 \text{ ns}$  is  $P_{ab}$ .

3. By the definition, the probability of triple coincidence which is caused by double muon events is

$$P_{abx} \equiv \frac{R_{abx}}{R_x} \quad (5.1)$$

$R_{abx}$  is the triple coincidence rate.  $R_x$  is the rate of the muons crossing STEO.

4. According to the book "Radiation detection and measurement" (Gleen, F) [66], the probability of double events which follows the Poisson distribution is calculated as follow,

$$\frac{dP_{abx}}{dt} = R_{ab}e^{-R_{ab}t} \quad (5.2)$$

where  $R_{ab}$  is the rate of the muons cross in STWO and SBWO.

5. Therefore, after combining equation 5.1 and equation 5.2, the rate of the double event is calculated as

$$P_{abx} \equiv \frac{R_{abx}}{R_x} = \int_0^{T_w} \frac{dP_{abx}}{dt} dt = 1 - e^{-R_{ab}T_w} \quad (5.3)$$

$$R_{abx} = R_x(1 - e^{-R_{ab}T_w}) \quad (5.4)$$

6. Finally, the expected number of the double event is  $N = TR_{abx} = TR_x(1 - e^{-R_{ab}T_w})$ .  $T$  is the time window. Since  $R_{ab}T_w = 34 \times \frac{10^3}{6 \times 10^{11}ns}$  is close to 0. Therefore,

$$N = T(1 - e^{-R_{ab}T_w}) = TR_{ab}T_w.$$

$$T = 10\text{min} = 6 \times 10^{11}ns$$

$$R_x = \frac{5 \times 10^4}{6 \times 10^{11}ns}$$

$$R_{ab} = \frac{10^3}{6 \times 10^{11}ns}$$

$$T_w = 34ns$$

$$N \approx 2.5 \times 10^{-3}$$

Technically, other situations which are not included in the calculation, such as the one in which one muon crosses STEO and SBWO while another crosses STWO, will also influent the results of number of double muon event  $N$  in the data taking time interval (10 minutes). However, due to the angular distribution of the muons [55], the possibility that those situations will happen is even lower. Therefore, other situations are negligible. The calculation results shows that the rate of the double muon events

is very small. In conclusion, double muon events should be rarely observed. As mentioned before, the source of the triple coincidences is either double events or crosstalk. However, compared with the rate of triple coincidences (5.5/min from previous section 5.1), the rate of double muon events ( $2.5 \times 10^{-4}/\text{min}$ ) is found to be low from the calculation. Therefore, crosstalk was believed to be the source of the triple coincidence. To verify the real crosstalk, the following measurements are done in the next section.

### 5.3 Crosstalk Measurement

The amplitude of a crosstalk signal should be inverse proportional to the distance between the signal cable and the trigger cable and the distance between the grounded wire and the signal wire, meanwhile it should be proportional to the intensity of the original signal [67]. Inside the signal cable in our lab, a signal wire is encased by coaxial cable. This design uses the principle of the Faraday Cage to reduce crosstalk.

The following four methods were used to test the crosstalk in our system.

#### 5.3.1 Method one: wire position

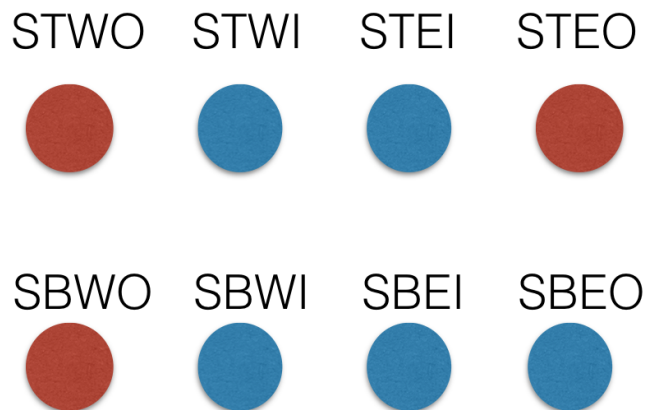


Figure 5.3: The set up of triple coincidence. The red ones identify the PMTs related to the triple coincidences measurements, the blue ones identify the other PMTs.

The triple coincidences of the three PMTs (STWO, STEO, and SBEO) were tested (shown in Figure 5.2 and Figure 5.3), while their signal cables were arranged in three different ways. If there is

crosstalk, the amount of triple coincidences would be significantly different between the three layouts.

The cable tray was placed on the east wall of the lab. The length of our lab (from east to west) is about 5.08 meters. The first set of data was taken when all three cables are placed in the cable tray. The second set of data was taken when one cable (STEO) was placed far away from the cable tray (4.06 meters from the east wall), while the other two remain in the cable tray. The third set of data was taken when two of the cables (STWO and STEO) were placed outside the cable tray, far away from each other (2.03 meters and 4.06 meters from the wall, respectively), while the last one remained in the cable tray. It is shown in Figure 5.4

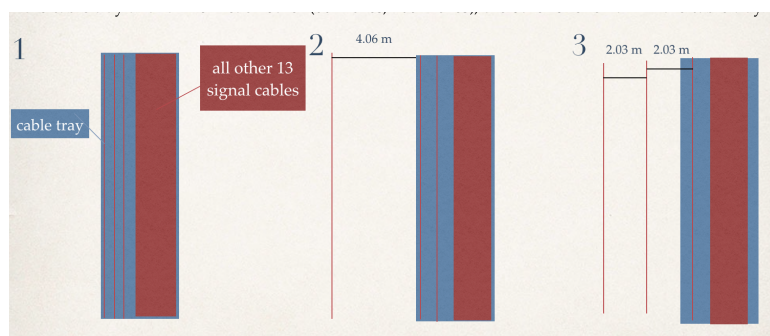


Figure 5.4: The set up of wire position measurements. The each red line identifies one cable, the blue area identifies the cable tray, the red area identifies the remaining thirteen cables.

All data were taken when only the three tested PMTs were turned on. The time window is 10 mins. Each measurement was repeated 3 times. All the coincidence tests were taken individually. The normal muon rate per one scintillator is about 100 Hz; the measurement below corresponds to 0.08 Hz. The measurements results are shown in Table 5.1.

Test Configuration	3 lines together	2 lines together	All 3 lines separated
Triple coincidences test No. 1	47	55	33
Triple coincidences test No. 2	45	49	52
Triple coincidences test No. 3	42	44	40
The mean of three tests	44.7±2.5	49.3±5.5	41.7±9.6

Table 5.1: The results of triple coincidence tests under different setting up. The mean of three tests for each group were also calculated.

As shown in Table 5.1, there is no significant difference among these data under different set ups. The rates of the triple coincidences are fairly consistent. Since the amplitude of crosstalk signal is

inverse proportional to the distance between the signal cable and the trigger cable, those signals do not match the behavior of the crosstalk.

### 5.3.2 Method two: HV on/off

Since the crosstalk is an inductance phenomenon, the state of the triggered cable (the one under crosstalk investigation) should have no influence on the crosstalk. In other words, even if the PMT is powered off or set to a low HV to avoid responding to real muon event, the rate of crosstalk should be influenced if it does exist. As before, the three PMTs (STWO, STEO, and SBEO) were tested (shown in Figure 5.3), the amount of triple coincidence in 10 minutes were recorded for each data point. Each group of measurement was repeated three times. Group 1: all three cables were put inside the cable tray, and all 16 PMTS were turned on. Group 2: one of the three PMTs whose cables are in the tray was turned off and the fifteen other PMTs were turned on . Group 3: the HV of one of the three PMTs whose cables are in the tray was set to 200 V, and all other PMTs were turned on. The measurements results are shown in Table 5.2.

Test configuration	group 1	group 2	group 3
Triple coincidences test No. 1	50	0	0
Triple coincidences test No. 2	33	0	0
Triple coincidences test No. 3	35	0	0
The mean of three tests	39.3±5.4	0	0

Table 5.2: Triple coincidence test when HV on/off.

There were no triple coincidences observed in last two groups of measurements. Therefore, the signals do not match the behavior of the crosstalk.

The previous measurement cannot determine the source of crosstalk (Top or Bottom PMTs). Because of the way of testing the sTGC, it is important to avoid crosstalk between the top and bottom signals. Therefore, two further measurements were set up to test this kind of crosstalk with all signal cables in the cable tray. The results are shown in Table 5.3.

On the left of the table the results with the HV are shown: the four top PMTs were connected using the “OR” logic unit; the four bottom PMTs were connected with the “AND” logic unit. On the right of

the table the result with the reduced HV are shown: when all top PMTs were on but at reduced high voltages (about 1000V), which is equivalent to turning them off.

Test configuration	With HV			With reduced HV		
	bottom	top and bottom	top	bottom	top and bottom	top
Test No. 1	52	36	331308	60	0	0
Test No. 2	63	40	301130	51	0	0
Test No. 3	63	39	300741	57	0	0
The mean of tests	59.3	38.3	311060	56	0	0
Error	$\pm 3.7$	$\pm 1.2$	$\pm 10125$	$\pm 2.7$	0	0

Table 5.3: The 5-fold coincidences test results. On the left of the table, the rate of the 5-fold coincidences is small compared with the rate of top signal. On the right of the table, no 5-fold coincidences was found.

As shown on the left of the table, since the rate of the 5-fold coincidences is very small compared with the rate of signals from top pmt (about 0.012%), even if those 5-fold coincidences were cross talk, they should not influent the result of sTGC testing significantly. On the right of the table, there were no 5-fold coincidences when all top PMTs were on but at reduced high voltages. Therefore, the signals don't match the behavior of the crosstalk.

### 5.3.3 Method three: amplitude correlation study

Using the oscilloscope MSO-X 4054A as a logic unit, 500 groups of data triggered by triple coincidences (PMTs STWO, STEO and SBEO) were recorded. Each group contains the wavedata of the signals for all three triggered PMTs as well as PMT SBWO. The set up of triple coincidence is shown on Figure 5.5

Each signal plot contains 1250 data points, each encoding the time and the voltage. MATLAB was used to display all the signals and wavedata in the computers. Based on the angular distribution of the muons, if crosstalk does exist, it most likely happens in the PMT STEO. For each muon event, the output signal of a PMT depends on how far from the PMT the muon crossed the scintillator. Therefore,

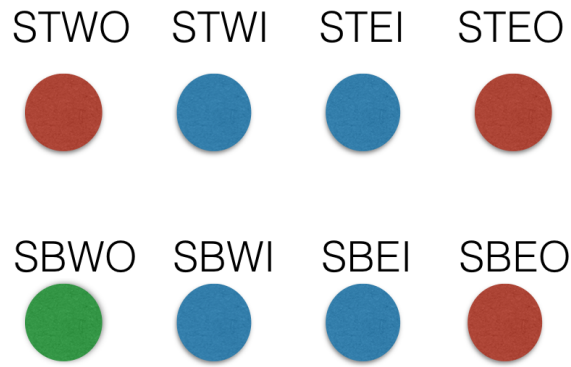


Figure 5.5: The set up of triple coincidence. The red ones identify the triggered PMTs in measurements, the green one identifies SBWO. the blue ones identify the other PMTs.

in the case of two upright parallel scintillators (TWO, BWO), the incidence angle of the muon has an influence on the amplitude of the PMT signal. However, assuming that the signals from STWO and SBWO are from the same muon event, the correlation of the signal amplitudes between STWO and SBWO is not strong since the position where the muon crossed the scintillator is unknown.

Since 500 groups of data were triggered by triple coincidences, there are only 312 groups of data containing the signals of SBWO. The ratio of quadruple coincidences to triple coincidences is 62.4%. Crosstalk signals are accidental. The chance that two crosstalk signals occur simultaneously is quite small. If quadruple coincidences are not due to crosstalk but that triple coincidences are, the correlation plots should not be similar in the two cases.

The first plot (Figure 5.6) shows the voltage amplitudes correlations of  $SBEO \wedge STWO$  and  $STEO \wedge STWO$  when there were signals for SBWO.

The second plot (Figure 5.7) shows the voltage amplitudes correlations of  $SBEO \wedge STWO$  and  $STEO \wedge STWO$  when there were no signal for SBWO.

All plots show random points. No amplitude correlation was found in both cases. The data on the edges of plots is due to the limit voltage unit on the oscilloscope.

In conclusion, the triple coincidences do not fit the behavior of the crosstalk.

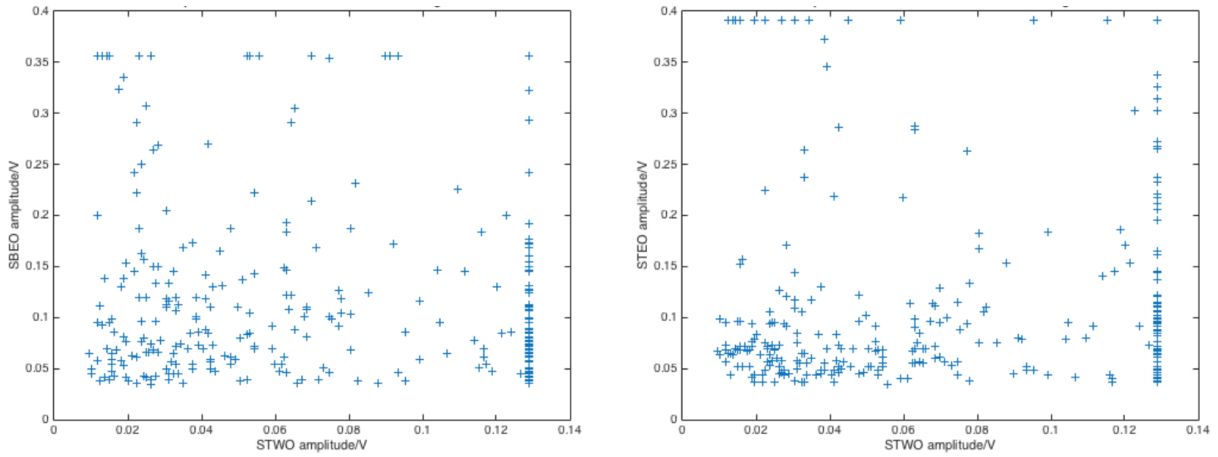


Figure 5.6: Data on both plots shows the voltage amplitude correlations when there are signals for SBWO. On the left is the voltage amplitudes correlations of  $SBE0 \wedge STWO$ , On the right is the voltage amplitudes correlations of  $STEO \wedge STWO$ . The limit voltage unit on the oscilloscope for the signal of SBE0 and STEO is 0.36 V. The limit voltage unit for the signal of STWO is 0.13 V.

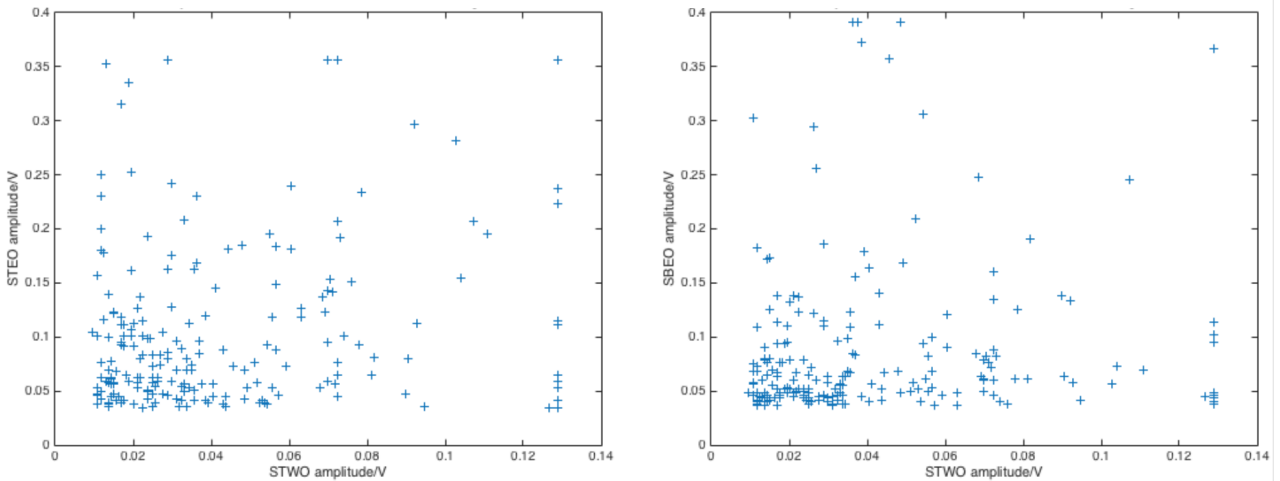


Figure 5.7: Data on both plots shows the voltage amplitude correlations when there are no signal for SBWO. On the left is the voltage amplitudes correlations of  $SBE0 \wedge STWO$ , On the right is the voltage amplitudes correlations of  $SBE0 \wedge STWO$ . The limit voltage unit on the oscilloscope for the signal of SBE0 and STEO is 0.36 V. The limit voltage unit for the signal of STWO is 0.13 V.

### 5.3.4 Method four: quadruple coincidence/triple coincidence

The original purpose of the method is to observe crosstalk. However, the result provides another piece of evidence which shows there is no significant crosstalk signal in our system. As mentioned above, the possibility that the original signal triggers two crosstalk signals is small. In this measurement, STEO, STWO and SBE0 are triggered using the CAEN discriminator with threshold voltages –1

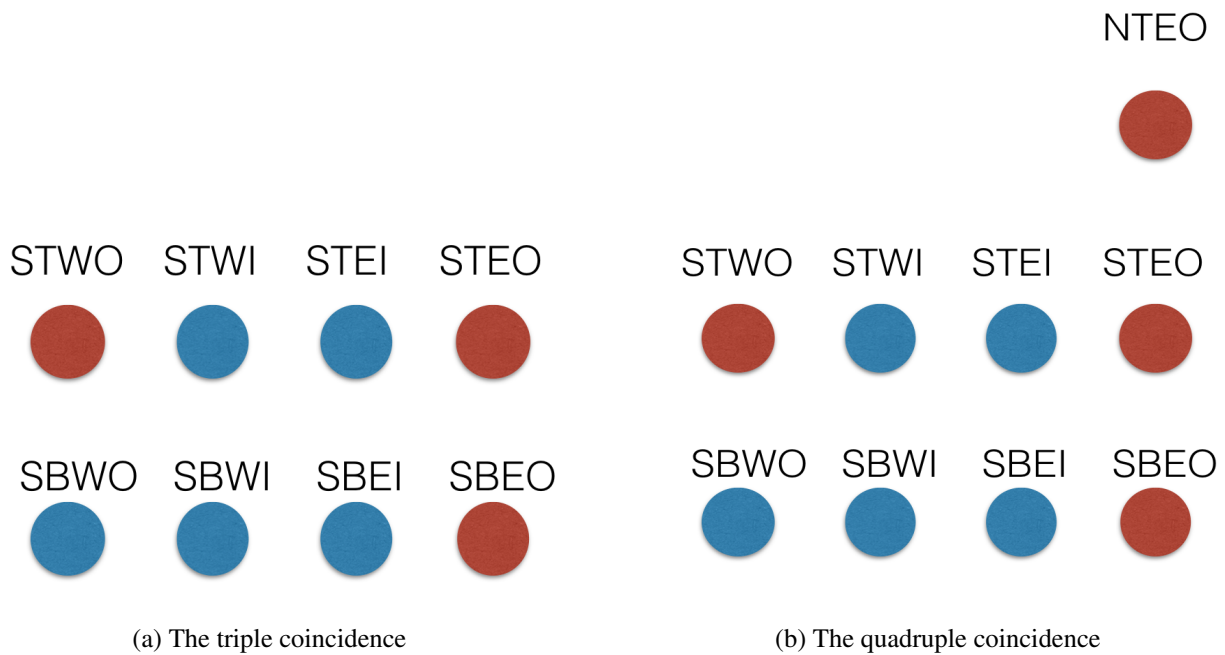


Figure 5.8: The set up of quadruple coincidence and triple coincidence measurements

mV,  $-5$  mV, and  $-5$  mV. The threshold voltage of STEO is set at a low value, because the crosstalk signal is assumed to have a lower amplitude than the primary signal. If the threshold voltage is zero, almost all double coincidences will be recorded. Since the rate of the triple coincidence over the double coincidence is low (1% in Figure 5.1), it requires some amount of time to distinguish triple coincidences from double coincidences. When the threshold voltage is at  $-1$  mV, it is high enough to register the crosstalk, but low enough to avoid many types of noise. This simplifies the later work. Since threshold voltage of STEO is  $-1$  mV, some of signal from STEO are just noise. Therefore, only 196 triple coincidence signals with effective STEO signals, as well as the status of the PMT NTEO, are selected from 500 groups of triple coincidence. The NTEO cable is placed outside of the cable tray to minimize the influence of crosstalk. The set up is shown in Figure 5.8. As shown in Figure 5.9, the signal pulse is reconstructed by MATLAB from the wavedata collected by the oscilloscope.

The results show that the ratio of quadruple coincidence (STEO, STWO, SBEO and NTEO) over triple coincidence (STEO, STWO and SBEO) is 100%.

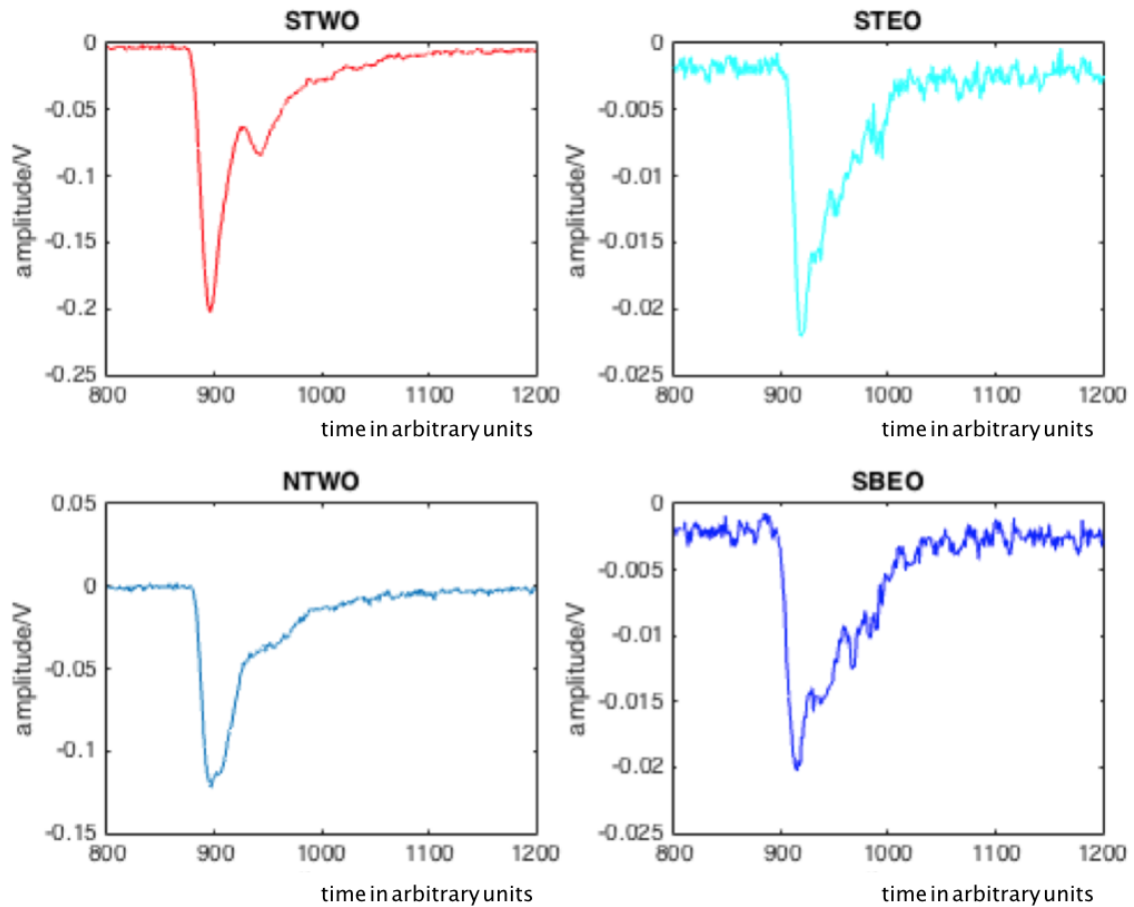


Figure 5.9: The signal pulses reconstructed by MATLAB with 0.2ns per point.

### 5.3.5 Conclusion

In conclusion, there was no significant difference in the triple coincidence rate no matter whether any of the signal cables are placed in or out of the tray or whether any of the PMTs (other than the ones that give the triple coincidence signal) are on or off. The maximum crosstalk probability in one PMT is about 2% (estimated from Table 5.2), which is too low to influence the efficiency test results of the sTGC significantly. The amplitude correlation study shows no correlation between SBEO  $\wedge$  STWO and between SBEO  $\wedge$  STEO.

All evidence indicates that the signals recorded were not crosstalk signals. From the theoretical calculation in section 5.2, the amount of coincidence signals is not expected to be as large as measured, but it is still very small(5.5/min) compared with the muon signals ( $\approx 37000$ /min) recorded in the trigger system . It will not significantly influence our cosmic data quality for sTGC detector testing. Therefore,

it is unnecessary to re-adjust the trigger system.

## 5.4 Potential Sources of Triple Coincidences

As the conclusion from the previous measurements in section 5.2 and section 5.3, the main source of the triple coincidences come from neither double muon events or crosstalk. Though the main source of the triple coincidences is verified strictly, there is one assumption which could help to explain it. The measured rate of triple coincidences was about 5.5/min (Figure 5.1). The expected number of double muon events, as calculated before, is about  $2.5 \times 10^{-4}$ /min. However, the calculation is based on the assumption that the two events are two independent muon events. What if they are not? Recall that muons at sea level mostly come from cosmic rays at a rate of about 1/min/cm<sup>2</sup> [55]. There are also protons (at a rate of 0.015/min/cm<sup>2</sup>), electrons (0.003/min/cm<sup>2</sup>), and other particles that come from cosmic rays at sea level [55]. Like muons, proton follow an angular distribution of  $\cos^2(\theta)$ . Protons and pions are products of the interaction between primary cosmic radiation and atmosphere, they could be assumed to be produced at same vertex. Since the decay time of the pion is negligible compared with decay time of the muon. Therefore, muons and protons can be produced at the same vertex. Each proton at sea level is correlated with one muon event. The triple coincidences are due to a proton and a muon crossing two scintillators at almost the same time. Firstly, because of their high energy, protons and muons have almost the same speed. Secondly, those protons and muons are assumed to be produced at one vertex. Lastly, the longest distance between scintillator TWO and BWO is about 3 m (recall Figure 5.2). Our time window for the “and” logic unit is 37 ns, which allows a distance of about 10 m.

Maple 16 is used to do a calculation about the number of triple coincidences happening in 10 minutes under the assumptions. Assume that 1500 protons crossed scintillator BWO in 10 minutes. This value comes from the rate of proton at sea level: 0.015/min/cm<sup>2</sup> x 9600cm<sup>2</sup> x 10 min. 9600cm<sup>2</sup> is the area of one scintillator. First, we find that for all protons crossing scintillator TWO, the probability of them also crossing scintillator BWO is about 13%. If the two points are connected on scintillators BWO and TWO through which one of the protons crossed, we get a line. this line was extended until the end is 20 km above the height of scintillator TWO. The line was divided into intervals such that the vertical height of each is 10 m, and keep only the endpoints of these intervals. It is assumed

that the proton was produced at one of these points. From the assumptions above, a muon must have been emitted from the same point. The probability that the muon crossed scintillator TEO is calculated assuming that it was produced at one of the above-mentioned endpoints. After that, all these probabilities are simply averaged and the probability that a muon crosses scintillator was found to be about 15%. The number of triple coincidences happening in 10 minutes is  $2 \times 1500 \times 13\% \times 15\% \approx 60$ .

The calculation result (60/10 min) roughly fits the measurement result ( $55.1 \pm 10.8$  /10 min from section 5.1). It is therefore reasonable to consider that the sources of the triple coincidences are protons and muons (or two time-correlated particles).

## Chapter 6

---

# Simulation

---

In efficiency vs. position measurements (subsection 4.3.2), a "mystery" that lower efficiencies near the middle of the scintillator compared to the edge has been left. There are two PMTs on one scintillator. Ideally, when a muon crosses a scintillator, each PMT will present a digital signal. The assumption for the "mystery" is that, compared with the situation when a muon cross the edge of the scintillator, when a muon crosses the middle of the scintillator, the signals produced from PMTs are weaker. Therefore, when some muons with low energy cross the middle of the scintillator, they may not be able to induce PMTs to produce strong enough signals to reach the discriminator threshold voltage. In this case, this muon event would not be recorded, which would reduce the efficiency.

The best way to determine this assumption is to simulate the whole progress of how a muon event leads to digital signals. And then, by comparing the amplitude of those digital signals when a muon crosses the edge of the scintillator and when a muon crosses the middle, the assumption could be determined.

The simulation is modified from a summer student's code [65]. It is a three dimensional simulation. Each simulation is for one muon crossing one specific area of the scintillator. In the simulation, when one muon crosses the scintillator, 40000 photons are emitted sequentially from four different points along the muon's track, which is simulated as a straight line, through the scintillator. The scintillator does not emit all the photons immediately. Since the number of photons  $N$  is proportional to the light intensity, the number of photons emitted from the scintillator is described by the equation [68].

$$N(t) = N_0(e^{-t/\tau_f} - e^{-t/\tau_r}) \quad (6.1)$$

where  $t$  is the elapsed time since the muon hit the scintillator,  $N_0$  is a constant that depends on the material of the scintillator,  $\tau_f$  is the decay time of the scintillator (2.1 ns) [56], and  $\tau_r$  is the rise time of the scintillator (0.9 ns) [56]. The time step of the simulation is chosen to be 0.05 ns. Photons will be reflected at the edge of the scintillator until they are absorbed in the scintillator or in the PMTs; the rate of absorption in the scintillator depends on the attenuation length (3.8m) [56]. Once they hit the PMTs, they will be absorbed and recorded. The number of photons reaching PMTs is recorded along the time with minimum time step 0.05ns. The numbers of electrons produced in the PMT is proportional to the number of photons reaching PMT multiplied by  $e^{-t/\tau}$ . Here  $\tau$  is the decay time of the PMT signal, which is not only defined by the inner impedance but which also depends on the outer impedance [68]. Therefore, its value could not be in the manual. Instead, trial and error method is used to estimate the value as 2.4 ns. Since the output signal is proportional to the number of electrons produced inside of the PMT, we plot the number of electrons as a function of time and compare the result with the real signal.

The simulation refers only one muon event at the time. A muon event is characterized by one trace of energy deposition in the scintillators. Therefore, in the measurement which is used to compare with the results of the simulation, the relevant trace for a muon event needs to be confirmed at the same approximate location, namely in this case where the muon crosses vertically the middle of the scintillators south edge.

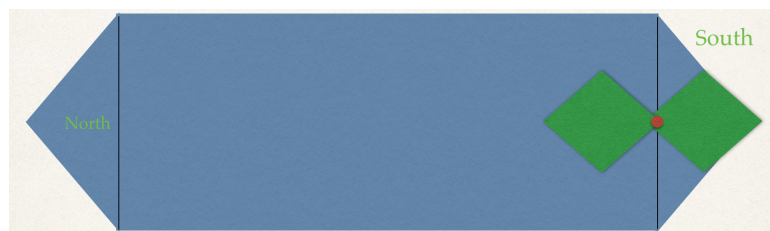
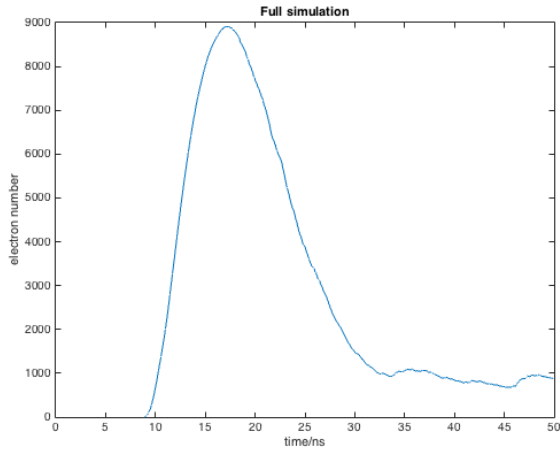
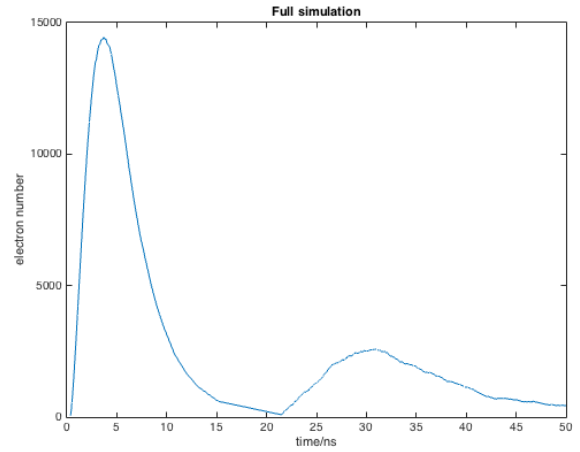


Figure 6.1: The setup of the simulation measurement. The red point is the overlap area. The green squares present two small PMTs. The right one (PMT) is placed on the top of the left one. The left one is placed on the lightguide with  $1 \text{ cm} \times 1 \text{ cm}$  overlap with large scintillator.

To specify a trace on the big scintillator, two small scintillators of equal size are used to provide the triple coincidence as a trigger signal. In this case, due to the space resolution of the simulation (the muon speed multiplied by the time step), a  $1 \text{ cm} \times 1 \text{ cm}$  area need to be focused on the large scintillator. However, There is no such small scintillators in our lab. Therefore, we design a measurement using our current equipment, two small scintillators with same sizes ( $25 \text{ cm} \times 12.5 \text{ cm} \times 2 \text{ cm}$ ). First, two

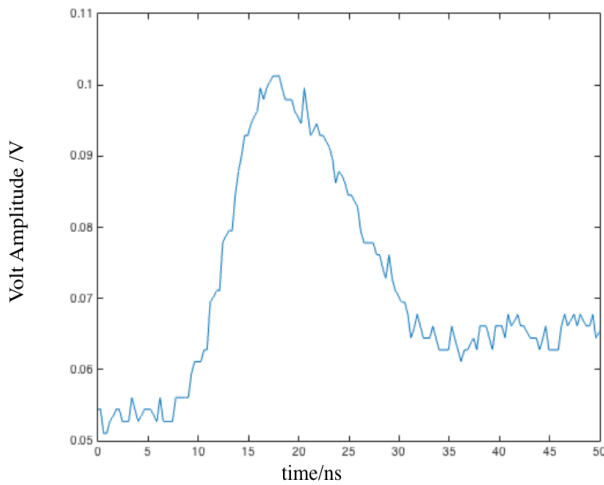


(a) The NTWO signal simulation

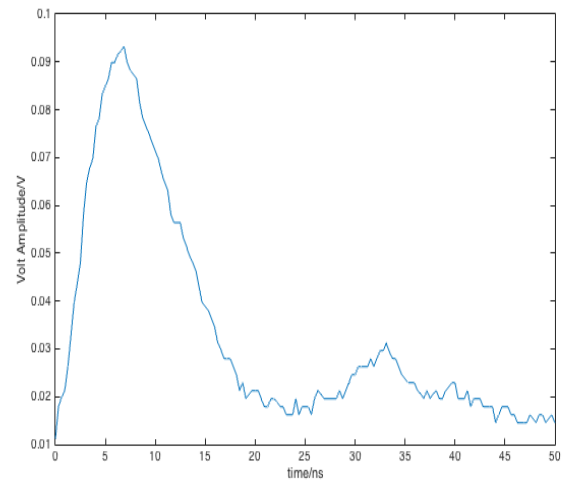


(b) The STWO signal simulation

Figure 6.2: The simulation result.



(a) The NTWO signal



(b) The STWO signal

Figure 6.3: The real datawave result.

small scintillators are placed so that their overlap is about  $1 \text{ cm} \times 1 \text{ cm}$ . The overlapping with the large scintillator covers an area shaped like an isosceles right triangle (long side  $\sqrt{2} \text{ cm}$ ). The remaining part of the small scintillator on the bottom touches the lightguide. Both small scintillators are on the south side of large scintillator. The setup of the measurement is shown in Figure 6.1.

And then, quadruple coincidences between PMTs NTWO, STWO, and the two small PMTs are triggered, and 200 groups of datawave are collected by the oscilloscope. It takes about three and half hours to collect all the data.

When the moun crosses the south edge of the scintillator, The STWO responses before the NTWO.

Compared to NTWO, the STWO produces a stronger signal. As shown in Figures 6.2 and 6.3, in both simulation and measurements results, there are two significant peaks shown in the plots for STWO, and there is only one significant peak for NTWO. The second peak for STWO is mostly due to the reflecting of photons from the north edge of the scintillator, however, the reflection is not strong enough to produce a second peak on the NTWO. As shown in the figure, the shapes of simulation results and experimental results are roughly similar. The time difference (12ns) between the two first peaks is close to the measurement results (11ns). After calculation, the mean amplitude ratio of measurement signals from 200 groups of data(STWO/NTWO) is  $1.5365 \pm 0.0490$ , the amplitude ratio of simulation pulse (STWO/NTWO)=  $14143/8980 = 1.57$ . In the measurement, the first peak does not decrease to zero like the simulation. Therefore, if we move the residual voltage of the first peak, the simulation fits the experimental results (experimental ratio of second peak over first peak was  $0.2336 \pm 0.0246$ , while that of the simulation was 0.2142). Notice that the simulation results can not exactly match the measurement result, because in the measurement, there are factors, such as dark current and shot noise, causing the uncertainty of results. However, from the consistency of amplitude ratio and the time difference between measurement results and simulation results, We could conclude that the simulation is ready to use to solve the "mystery".

After the simulation when a muon crosses the edge is done, the next step is to simulate when a muon crosses the middle of the scintillation. In this situation, the two PMTs (NTWO and STWO) have same result due to the symmetry, therefore, only one plot (Figure 6.4) is shown as result.

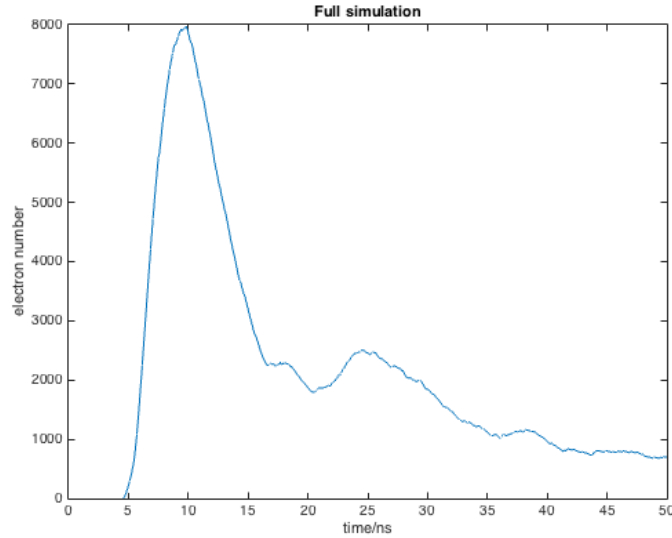


Figure 6.4: The simulation of signal when a muon cross the middle of the scintillator.

Compared to the amplitudes of signals from NTWO and STWO in Figure 6.3, when a muon crosses the south edge of the scintillator, the amplitude of signal when a muon crosses the middle has a lower amplitude. The difference of amplitudes is not large in the simulation, since we assumed that the PMTs functioned properly in the simulation. However, in previous measurement (subsection 4.3.2), where the dip was observed (Figure 4.23), the PMT was not yet fully powered. Since the number of electrons produced in the PMT is proportional to the HV [68]. Therefore, when the PMT is not fully powered, the difference between the two amplitudes will increase. This explains the "mystery" of why efficiency is significantly lower in the middle compared to the edge. In later measurements the HV was brought up to repair this deficiency.



## Chapter 7

---

# Summary and Conclusion

---

In this thesis, what work was done to improve the efficiency of the trigger system which will be used to test the small thin gap chamber (sTGC) detector has been presented. Two groups of setups for the high voltages and discriminator threshold voltages were determined for two different discriminators. The proper high voltages and discriminator threshold voltages have been applied on the sixteen PMTs individually with the CAEN N843. Factors which could influence the efficiency, such as muons hitting different areas of scintillators, time differences and crosstalk, have been thoroughly studied. A simulation was performed of all the processes that lead to an electrical signal in the PMT when a muon hits the scintillator.

In Chapter 4, all the measurements we performed to study the efficiency of the trigger system are described in detail. For each performed measurement, the motivation for it is described, as well as the method and the results. The proper high voltages and threshold voltages for the CAEN N843 were set up using two methods (rate and efficiency); the same efficiency measurement method is also used for LeCroy 623B. The efficiency vs. position efficiency vs. PMT powering time, and HV curve vs. position results for all PMTs prove that the all parts of the scintillator behave the same way. In Chapter 5, measurements related to crosstalk show that our crosstalk rates are not high enough to significantly influence the efficiency of the trigger system. Two calculations related to the crosstalk rate, as well as the rate of correlated proton-muon events, were presented in detail to provide insight into the unexpected triple coincidences observed during the crosstalk measurements.

As a conclusion, all PMTs in the trigger system has the proper high voltages and threshold voltages and there is rare cross talk signal found in the measurements. Therefore, the efficiency results are

reliable. All scintillators in the trigger system has consistently high efficiency above 98% (Table 4.6). With such high efficiency, once a muon crosses the trigger system, in 98% chance it will be recorded and triggered with sTGC. Therefore, conclusively, the trigger system is ready to be used.

Chapter 6 shows how the process is simulated by which an digital signal is produced from a muon event. The physical principles behind the code and the experimental setup is described in detail. The simulation results match the experimental results, so it was used to explain the dip in plots for efficiency vs. position in Figure 4.23. It could be also used to compare with the results of other measurements in the future, such time difference between two PMTs on one scintillator vs. position.

The results and conclusions of the thesis will be useful for the quality testing and performance assessment of the new sTGC detector. With the installation on ATLAS of the new small wheel(NSW), which is built from sTGCs and the MM, we will have better explanations of many unsolved questions in high energy physics. It is hoped that this work, and similar work by others, will contribute to a deeper understanding of our world's foundational structure.

---

# Glossary

---

**ALICE** A Large Ion Collider Experiment. 15, 16

**ATLAS** A Toroidal LHC ApparatuS. 15–17, 20, 21

**CFD** The constant fraction discriminator. 34, 35

**CMS** Compact Muon Solenoid. 15–18

**CSC** Cathode Strip Chambers. 21, 22

**DAQ** Data Acquisition. 63

**LAr** The Liquid Argon Calorimeter. 20

**LHC** Large Hadron Collider . 5, 12, 15, 17

**LHCb** The Large Hadron Collider beauty. 15, 17

**MDT** Monitored Drift Tubes. 21

**MM** Micromegas. 24, 25, 84

**MUON** Muon Spectrometer. 21, 23

**NSERC** The Natural Sciences and Engineering Research Council of Canada. 26

**NSW** New Small Wheel. 2, 24, 84

**PMT** Photomultiplier tube. 21, 39–41

**QCD** quantum chromodynamics. 9, 16

**RPC** Resistive Plate Chamber. 21, 23

**sTGC** the small-strip thin gap chambers. 2, 24–26, 30, 83, 84

**TGC** Thin Gap Chambers. 21, 25

**TILE** The Tile Hadronic Calorimeter. 20, 21

## Appendix A

---

# Additional plots

---

This appendix is relevant to the Chapter 4.

### A.1 The HV curve and signal threshold voltage curve for PMT A and B

In this section, those plots about the HV curve and signal threshold voltage curve for PMT A and B are shown.

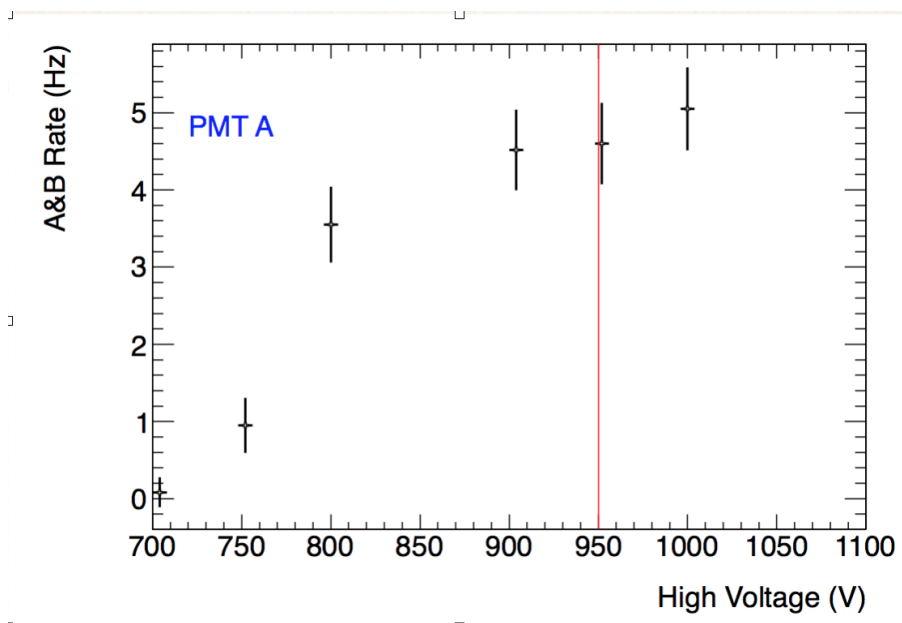


Figure A.1.1: The HV curve for PMT A.

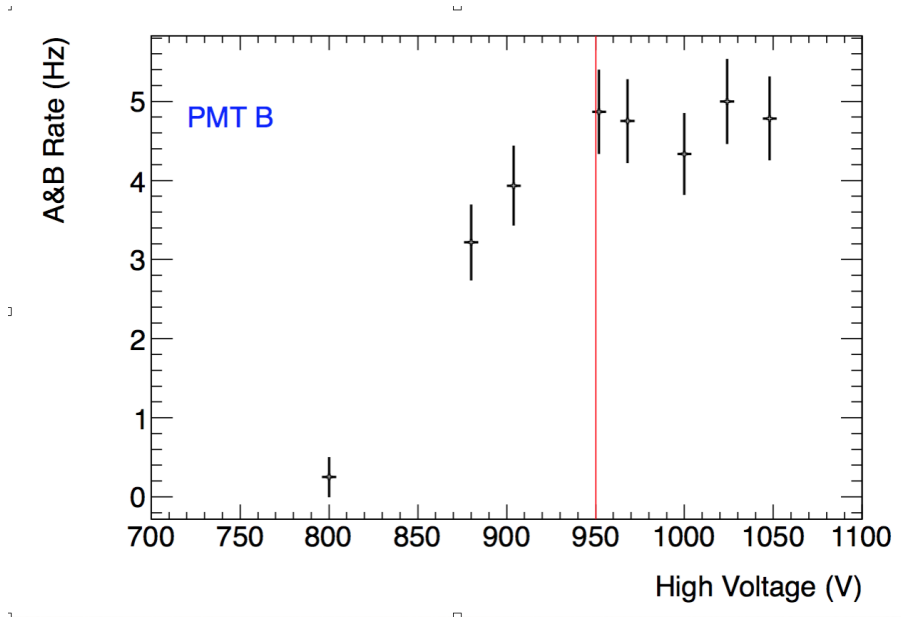


Figure A.1.2: The HV curve for PMT B.

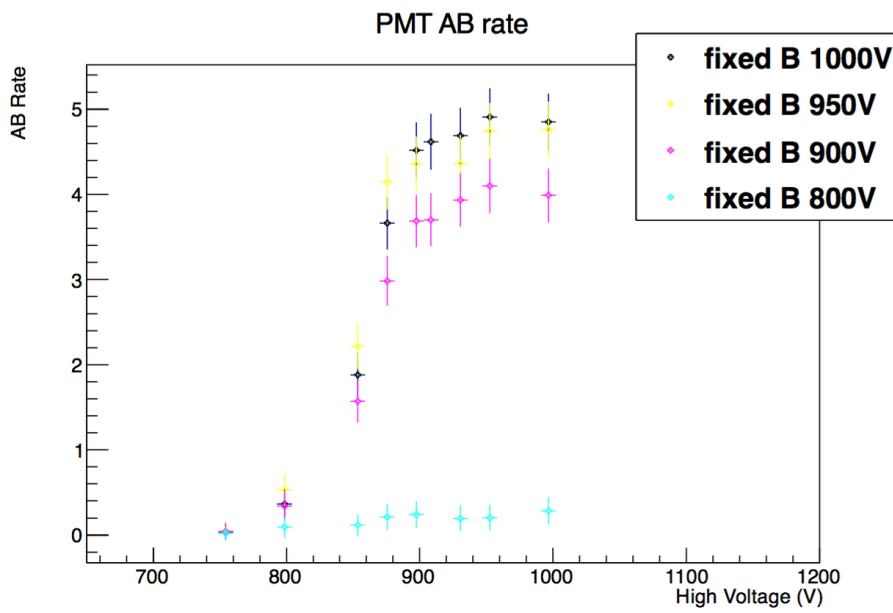


Figure A.1.3: The HV curve for PMT A at different HV for PMT B.

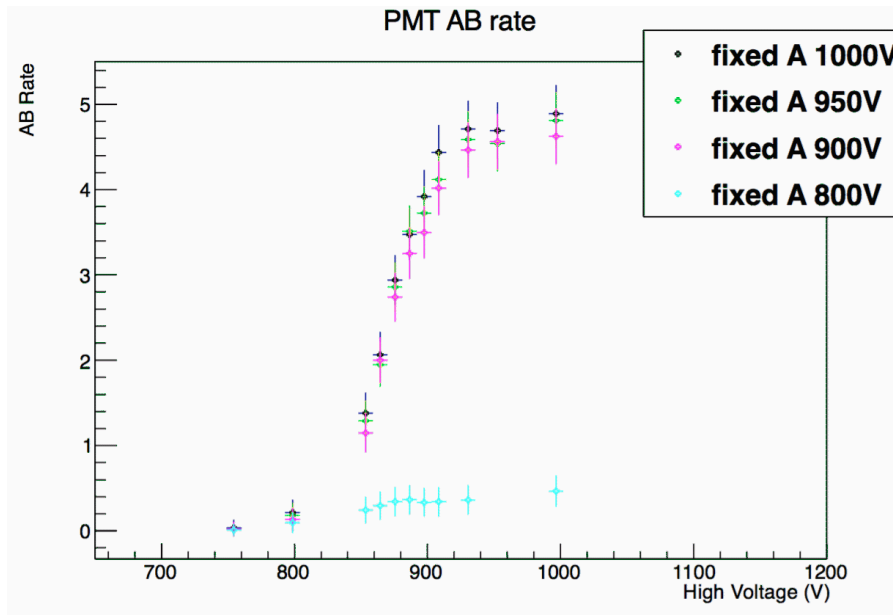


Figure A.1.4: The HV curve for PMT B at different HV for PMT A.

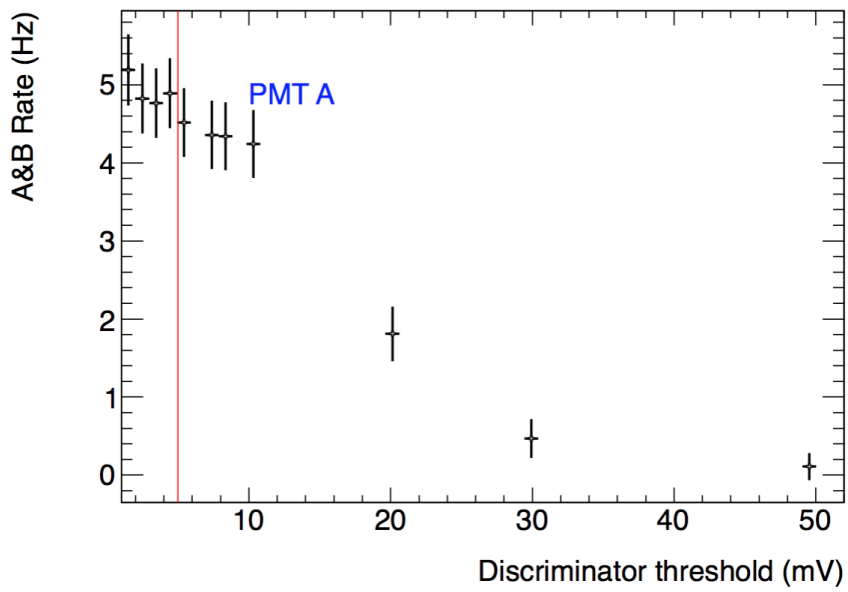


Figure A.1.5: The threshold voltage curve for PMT A.

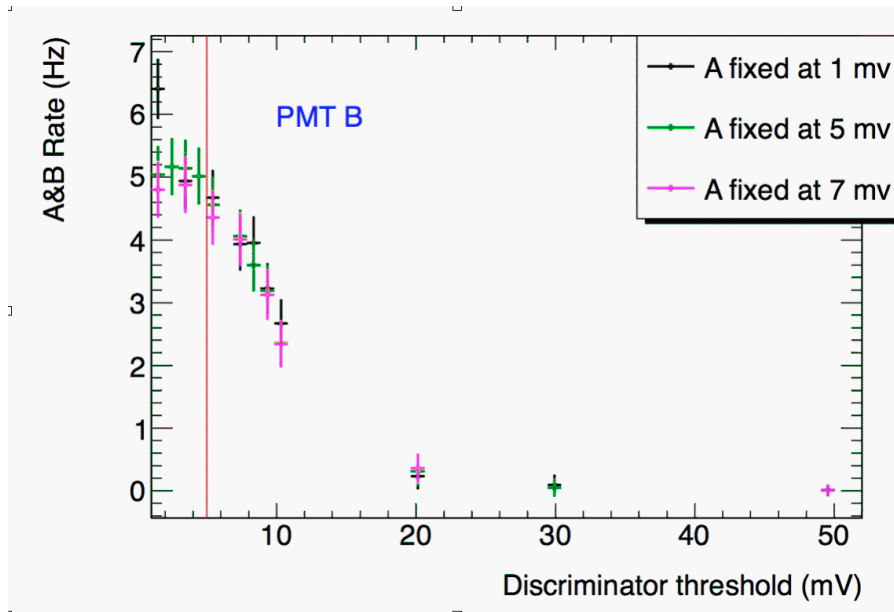


Figure A.1.6: The threshold voltage curve for PMT B at different threshold voltages for PMT A.

## A.2 The HV curve for all PMTs

In this section, those plots about the HV curve for all PMTs are shown.

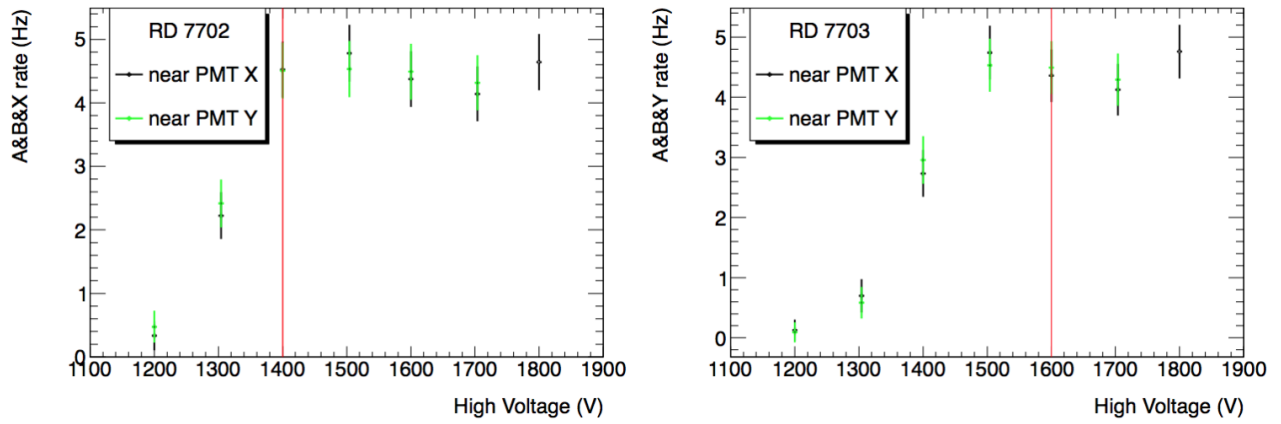


Figure A.2.1

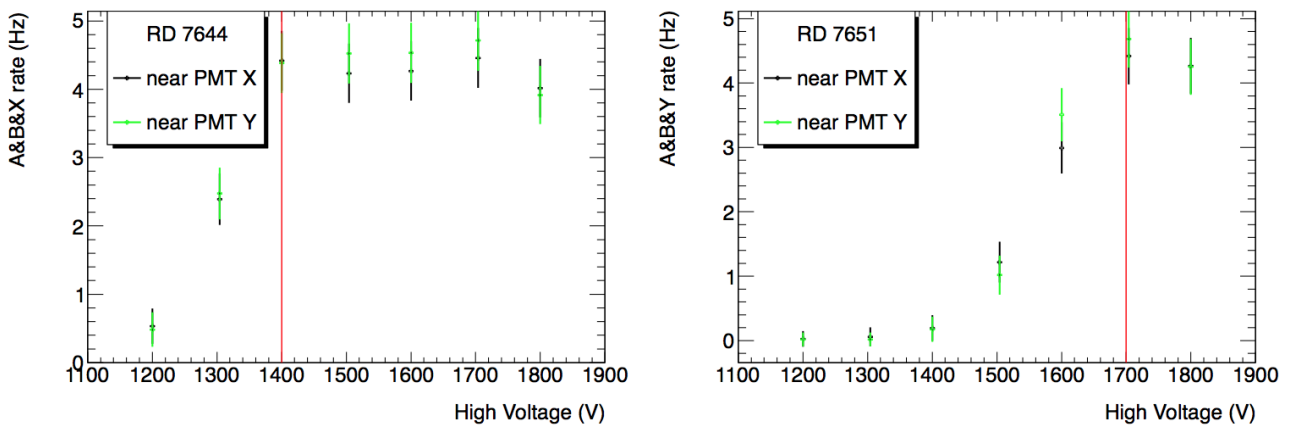


Figure A.2.2

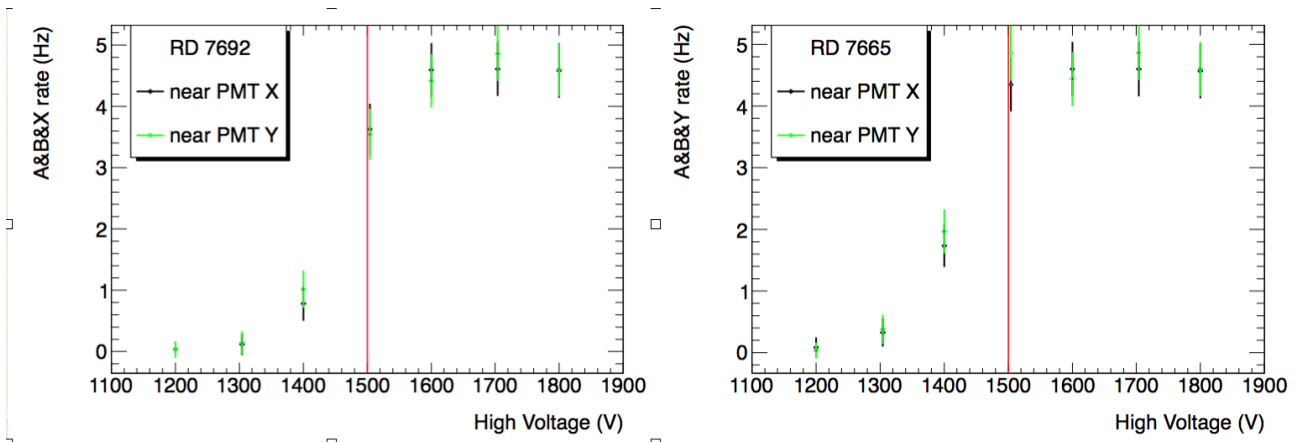


Figure A.2.3

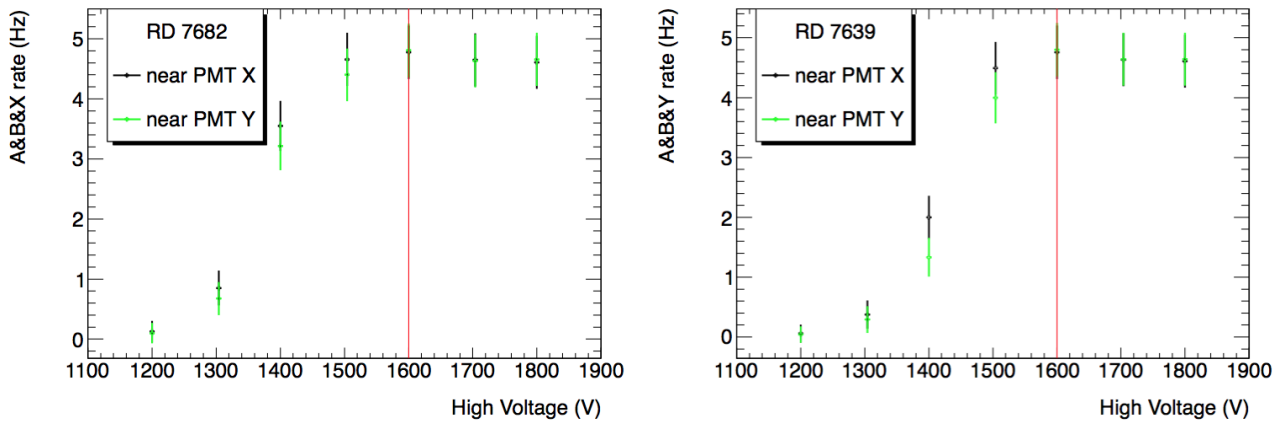


Figure A.2.4

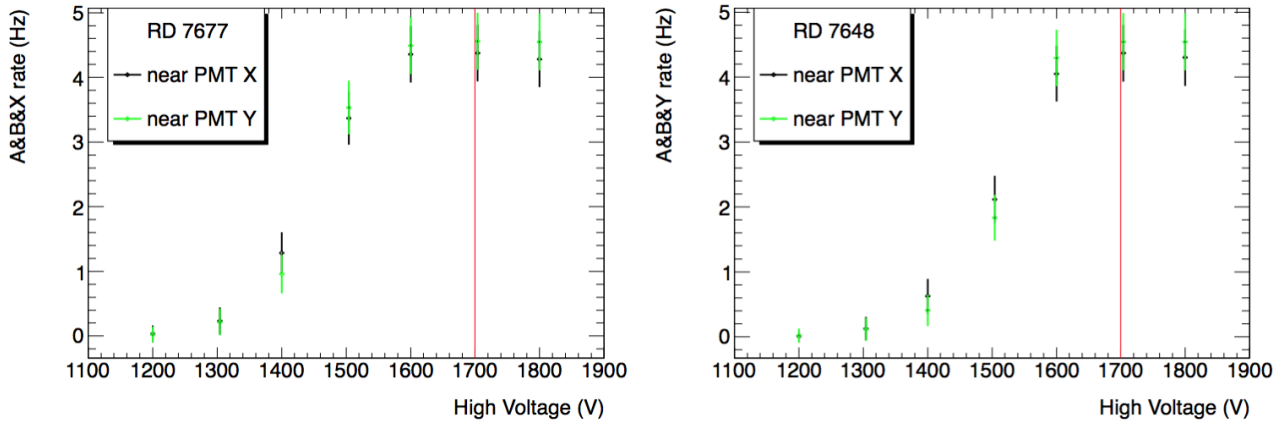


Figure A.2.5

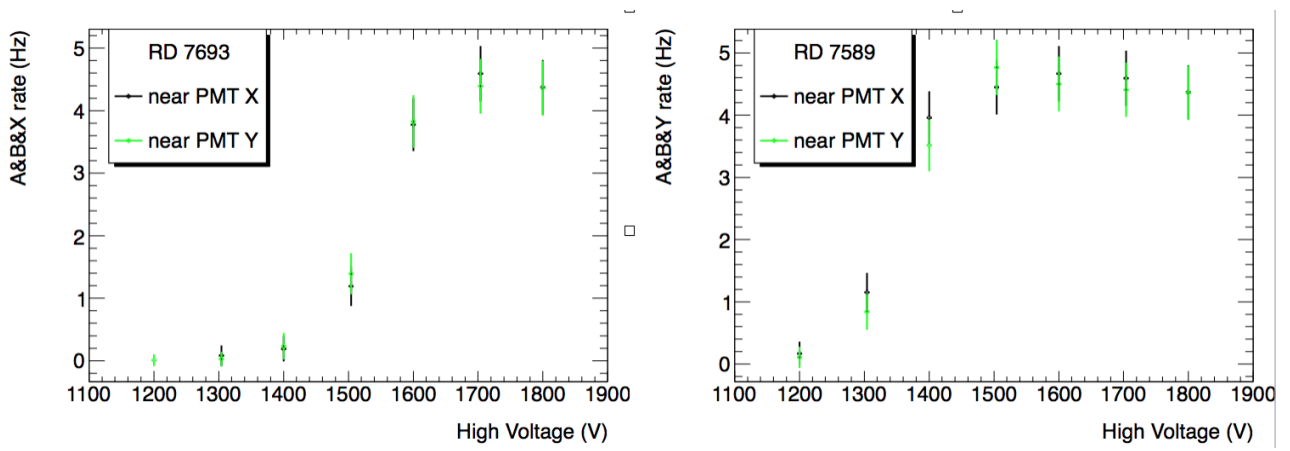


Figure A.2.6

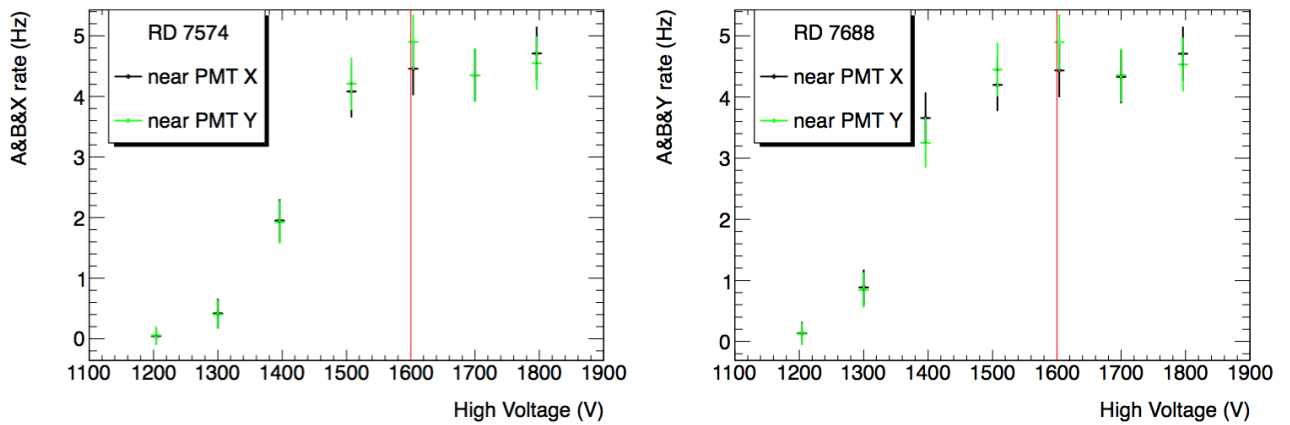


Figure A.2.7

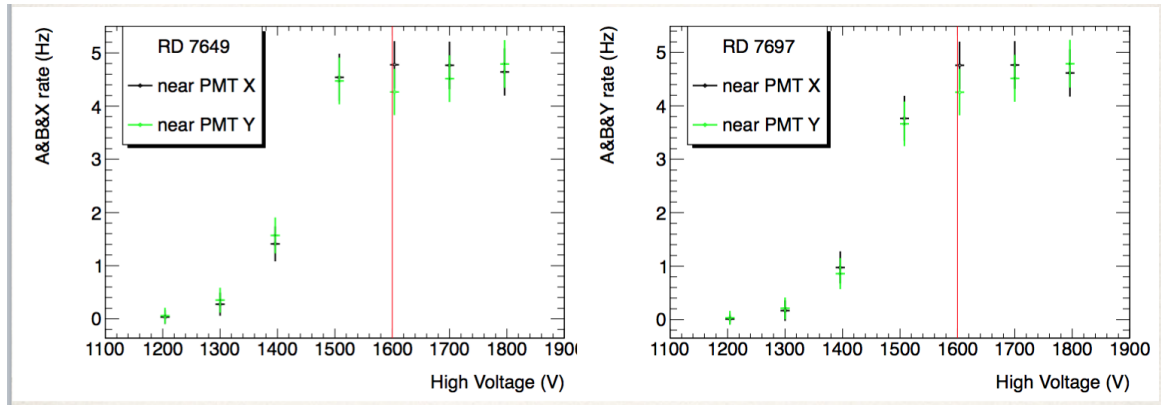


Figure A.2.8

### A.3 The signal threshold voltage curve for all PMTs.

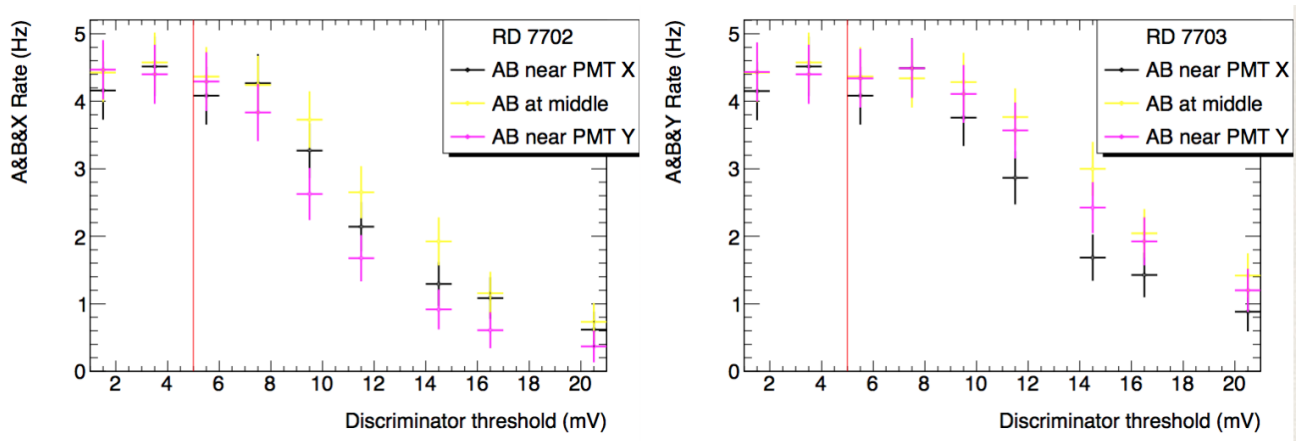


Figure A.3.1

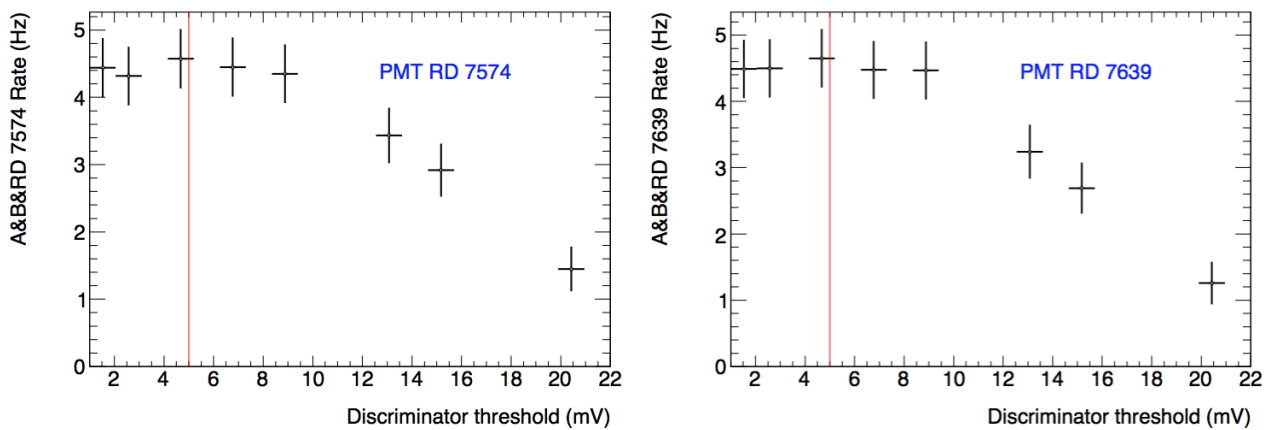


Figure A.3.2

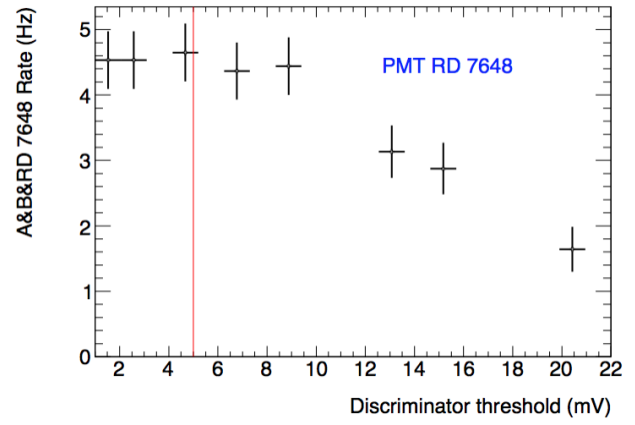
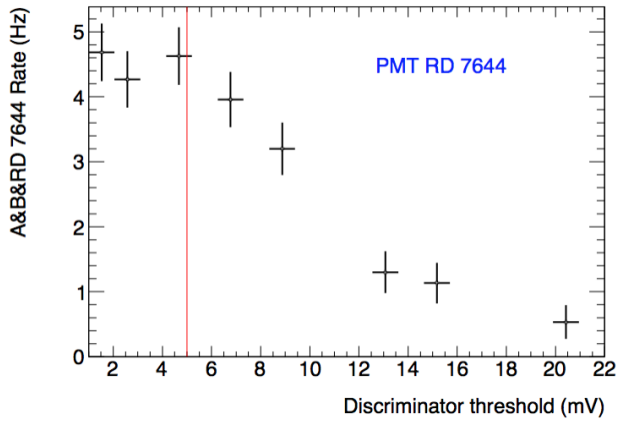


Figure A.3.3

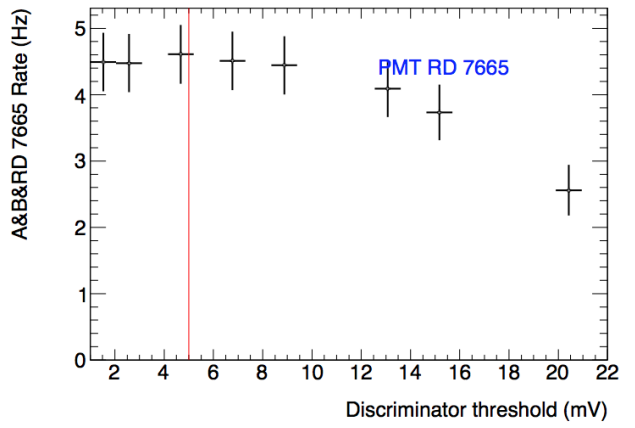
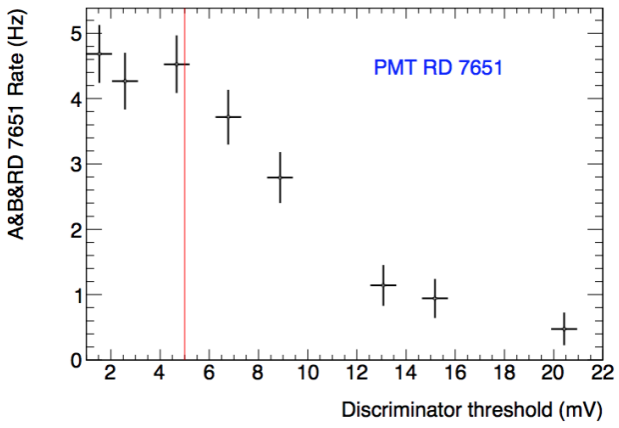


Figure A.3.4

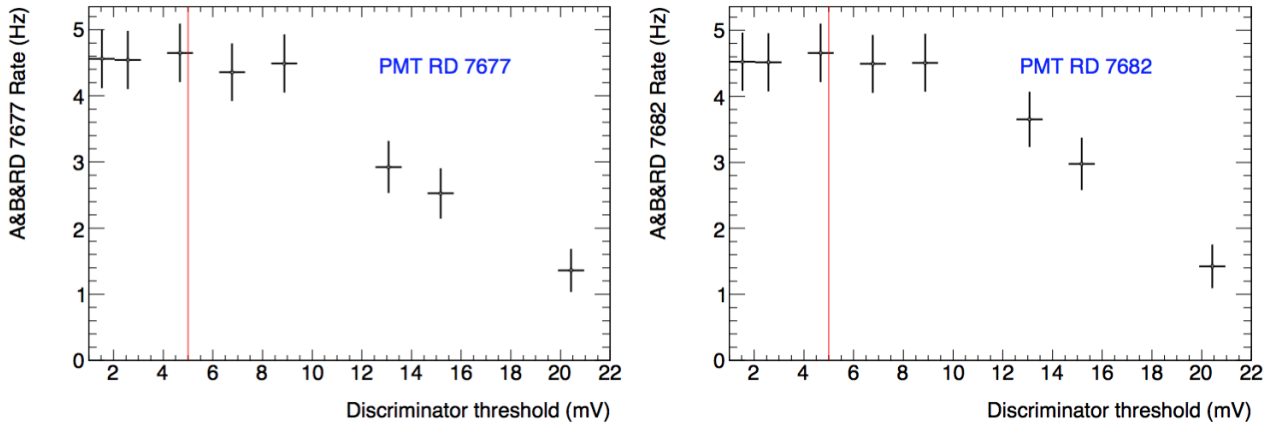


Figure A.3.5

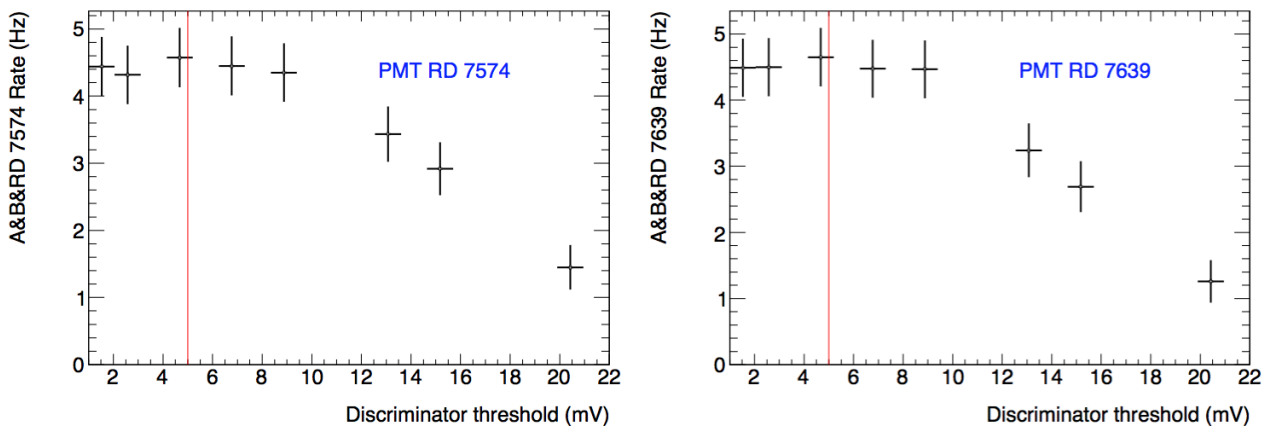


Figure A.3.6

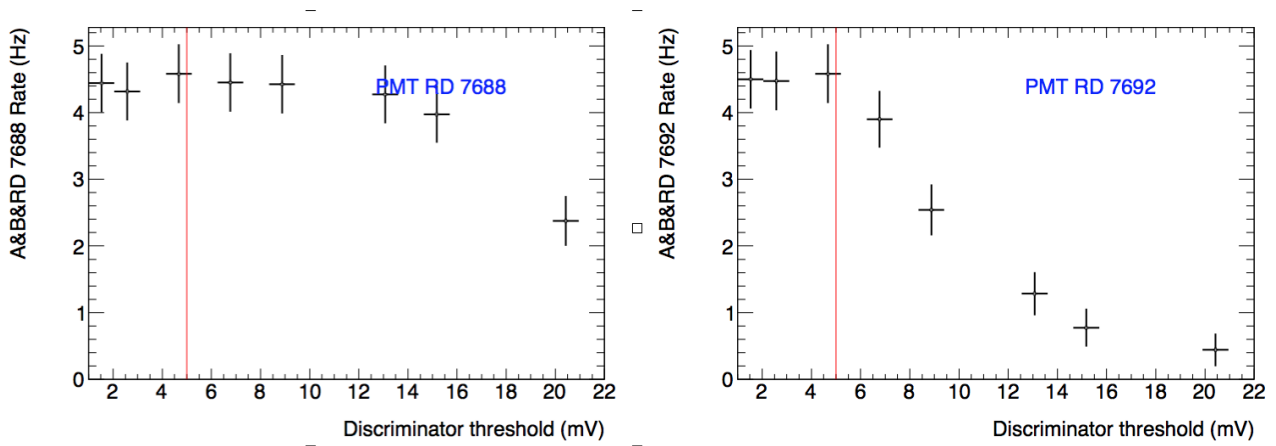


Figure A.3.7

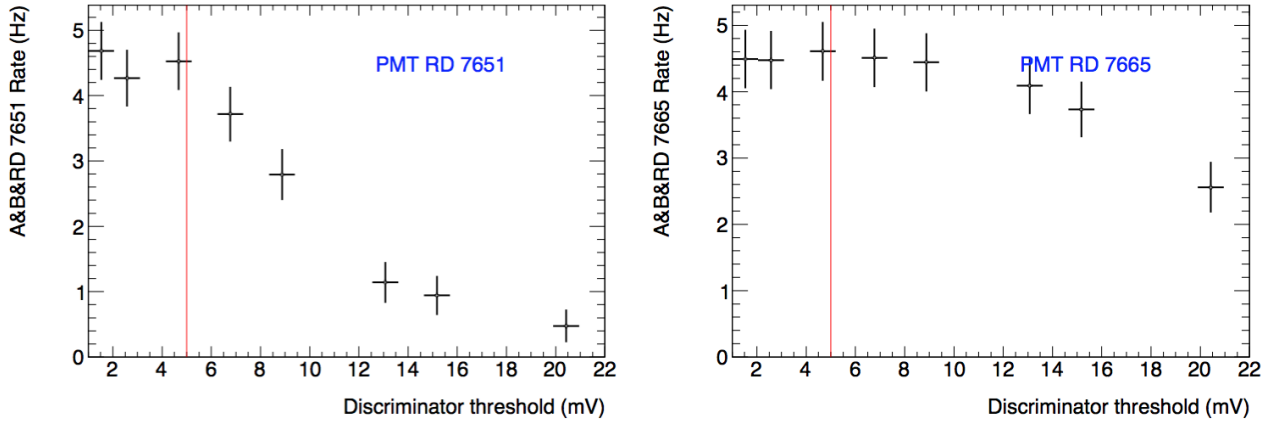


Figure A.3.8

## A.4 Table for the HV setting up using LeCroy

Location	Scintillator	Lightguide location	Lightguides	PMTs	HV
TWO	#6003-01-07	South	#6003-02-07	RD7589	1500
		North	#6003-02-08	RD7693	1700
TWI	#6003-01-06	South	#6003-02-04	RD7703	1500
		North	#6003-02-03	RD7702	1500
TEI	#6003-01-05	South	#6003-02-16	RD7688	1500
		North	#6003-02-15	RD7574	1600
TEO	#6003-01-08	South	#6003-02-12	RD7697	1550
		North	#6003-02-11	RD7649	1550
BEO	#6003-01-04	South	#6003-02-01	RD7648	1650
		North	#6003-02-02	RD7677	1650
BEI	#6003-01-03	South	#6003-02-06	RD7639	1550
		North	#6003-02-05	RD7682	1550
BWI	#6003-01-02	South	#6003-02-09	RD7665	1600
		North	#6003-02-10	RD7692	1600
BWO	#6003-01-01	South	#6003-02-14	RD7651	1700
		North	#6003-02-13	RD7644	1400

Table A.1: LeCroy: the signal threshold voltage at -30 mV.

## A.5 The efficiency vs. position measurements for NTWO.

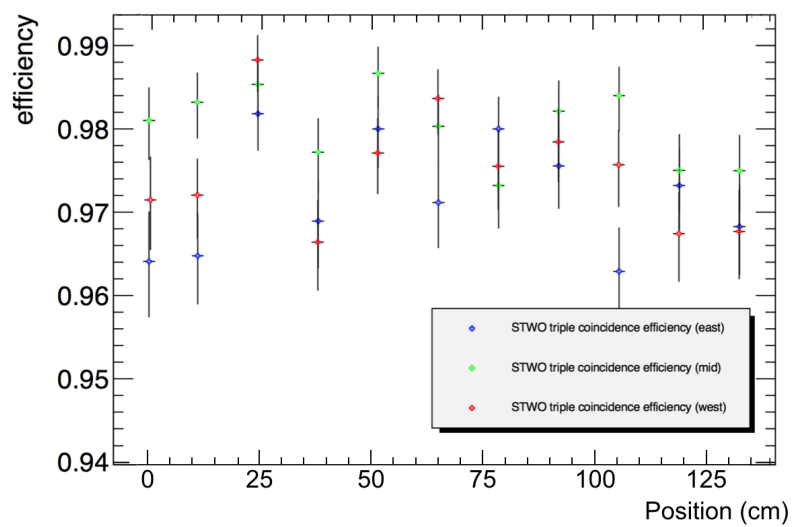


Figure A.5.1: The efficiency vs. position measurements for STWO.

## Appendix *B*

# Calculation

This appendix describes the calculation for uncertainty of the efficiency in detail in Section 4.2.2.

### B.1 The calculation of uncertainty of the efficiency

If  $N_A$  stands for the counts of double coincidence "PMT A and PMT B" events (or triple coincidence "PMT A, PMT B and large scintillator PMT" events) and  $N_B$  stands for the counts of single hit "PMT A or PMT B" (or double hits "PMT A and PMT B") and in the case that  $t_A$  refers to the time interval, the uncertainty on the efficiency ratio is calculated as follows:

$$Rate = \frac{N_A}{t_A} \quad (B.1)$$

$$\sigma^2(Rate) = \left(\frac{\partial Rate}{\partial N}\right)^2 + \left(\frac{\partial Rate}{\partial t}\right)^2 \quad (B.2)$$

$$= \left(\frac{\partial N_A}{t_A}\right)^2 + \left(-\frac{N_A}{t_A^2} \partial t_A\right)^2. \quad (B.3)$$

$$\sigma(Rate) = \frac{\partial Rate}{\partial N} = \frac{\sqrt{N_A}}{t_A} \quad (B.4)$$

$$\sigma^2\left(\frac{Rate_A}{Rate_B}\right) = \frac{N_A}{N_B} \times \left(\left(\frac{\sigma N_A}{N_A}\right)^2 + \left(\frac{\sigma N_B}{N_B}\right)^2\right) \quad (B.5)$$

$$= \frac{N_A^2}{N_B^2} \times \left(1 + \frac{N_A}{N_B}\right) \quad (B.6)$$

$$\sigma\left(\frac{Rate_A}{Rate_B}\right) = \sqrt{\frac{N_A^2}{N_B^2} + \frac{N_A^3}{N_B^3}} \quad (B.7)$$



---

# Bibliography

---

- [1] Crespigny and R. R. C. De, “A Biographical Dictionary of Later Han to the Three Kingdoms (23-220 AD) (Handbook of Oriental Studies, Section 4),” Jan 2007.
- [2] A. W. Thackray, “The origin of dalton’s chemical atomic theory: Daltonian doubts resolved,” *Isis*, vol. 57, no. 1, pp. 35–55, 1966. [Online]. Available: <http://www.jstor.org/stable/228689>
- [3] S. L. Glashow, “Towards a unified theory: Threads in a tapestry,” *Rev. Mod. Phys.*, vol. 52, pp. 539–543, Jul 1980. [Online]. Available: <http://link.aps.org/doi/10.1103/RevModPhys.52.539>
- [4] P. W. Higgs, “Broken symmetries and the masses of gauge bosons,” *Phys. Rev. Lett.*, vol. 13, pp. 508–509, Oct 1964. [Online]. Available: <http://link.aps.org/doi/10.1103/PhysRevLett.13.508>
- [5] A. N. P. in Physics, “Nobelprize.org.” [Online]. Available: [https://www.nobelprize.org/nobel\\_prizes/physics/laureates/](https://www.nobelprize.org/nobel_prizes/physics/laureates/)
- [6] J. Daniels, “Latest theory of everything to hit the physics shelves.” [Online]. Available: <http://www.united-academics.org/space-physics/>
- [7] “CERN Rapport annuel 2014,” CERN, Geneva, Tech. Rep., 2015. [Online]. Available: <https://cds.cern.ch/record/2026820>
- [8] R. Saban, B. Bellesia, M. P. Casas Lino, C. Fernandez Robles, M. Pojer, R. Schmidt, M. Solfaroli Camillocci, and A. Vergara Fernandez, “Coordination of the commissioning of the LHC technical systems,” no. CERN-TS-2008-009, p. 5 p, Jun 2008. [Online]. Available: <https://cds.cern.ch/record/1151309>

- [9] C. O’Luanaigh, “The Large Hadron Collider,” Jan 2014. [Online]. Available: <https://cds.cern.ch/record/1998498>
- [10] T. S. Virdee, “The experiments: particle detection at the LHC: an introduction,” p. 10 p, 2009. [Online]. Available: <https://cds.cern.ch/record/1193083>
- [11] A. Apollonio, M. Benedikt, and R. Schmidt, “Machine Protection: Availability for Particle Accelerators,” Ph.D. dissertation, TU Vienna, Vienna, Mar 2015, presented 16 Mar 2015. [Online]. Available: <https://cds.cern.ch/record/2002820>
- [12] J. Engelen, “The large hadron collider project: organizational and financial matters (of physics at the terascale),” *Philosophical Transactions of the Royal Society of London A: Mathematical, Physical and Engineering Sciences*, vol. 370, no. 1961, pp. 978–985, 2012. [Online]. Available: <http://rsta.royalsocietypublishing.org/content/370/1961/978>
- [13] M. Brice, “Aerial View of the CERN taken in 2008.” Jul 2008. [Online]. Available: <https://cds.cern.ch/record/1295244>
- [14] L. Taylor, “CMS detector design,” Nov 2011. [Online]. Available: <http://cms.web.cern.ch/news/cms-detector-design>
- [15] C. O’Luanaigh, “ CMS: The Compact Muon Solenoid ,” Feb 2012. [Online]. Available: <https://cds.cern.ch/record/1997263>
- [16] —, “ALICE: A Large Ion Collider Experiment ,” Feb 2012. [Online]. Available: <https://cds.cern.ch/record/1997265>
- [17] —, “ALICE precisely compares light nuclei and antinuclei,” Aug 2015. [Online]. Available: <https://cds.cern.ch/record/2051990>
- [18] Stefan, “ALICE detection system,” Jul 2012. [Online]. Available: [http://alicematters.web.cern.ch/?q=tiziano\\_virgili](http://alicematters.web.cern.ch/?q=tiziano_virgili)
- [19] C. O’Luanaigh, “LHCb: The Large Hadron Collider beauty experiment ,” Feb 2012. [Online]. Available: <https://cds.cern.ch/record/1997262>

- [20] R. Aaij *et al.*, “Measurement of the  $CP$  asymmetry in  $B_s^0 - \bar{B}_s^0$  mixing,” 2016.
- [21] L. Experiment, “LHCb detector design,” 2008. [Online]. Available: <http://lhcb-public.web.cern.ch/lhcb-public/en/Detector/Detector-en.html>
- [22] C. O’Luanaigh, “ATLAS.  $\text{lt;div class=}$ “field-headline” $\text{gt;}$  ATLAS: The largest volume particle detector ever built  $\text{lt;/divgt;}$ ,” Feb 2012. [Online]. Available: <https://cds.cern.ch/record/1997264>
- [23] A. Experiment, “The Cut-away view of the ATLAS detector,” 2008. [Online]. Available: <https://twiki.cern.ch/twiki/bin/viewauth/AtlasPublic/AtlasTechnicalPaperListOfFigures?t=1465325808>
- [24] G. Aad, B. Abbott, J. Abdallah, and *etal*, “The atlas inner detector commissioning and calibration,” *The European Physical Journal C*, vol. 70, no. 3, pp. 787–821, 2010. [Online]. Available: <http://dx.doi.org/10.1140/epjc/s10052-010-1366-7>
- [25] A. Experiment, “The inner detector design,” 2008. [Online]. Available: <https://twiki.cern.ch/twiki/bin/viewauth/AtlasPublic/AtlasTechnicalPaperListOfFigures?t=1465325808>
- [26] N. Wermes and G. Hallewel, *ATLAS pixel detector: Technical Design Report*, ser. Technical Design Report ATLAS. Geneva: CERN, 1998. [Online]. Available: <https://cds.cern.ch/record/381263>
- [27] A. Experiment, “The Inner Detector,” 2016. [Online]. Available: <http://atlas.cern/discover/detector/inner-detector>
- [28] G. Aad *et al.*, “Operation and performance of the ATLAS semiconductor tracker,” *JINST*, vol. 9, p. P08009, 2014.
- [29] I. M. Gregor, A. R. Weidberg, S. C. Lee, M. L. Chu, and P. K. Teng, “Optical data links for the ATLAS SCT and pixel detector,” *Nucl. Instrum. Methods Phys. Res., A*, vol. 465, no. 1, pp. 131–4, 2001. [Online]. Available: <https://cds.cern.ch/record/516878>
- [30] V. A. Mitsou, “The ATLAS Transition Radiation Tracker,” CERN, Geneva, Tech. Rep. ATL-CONF-2003-012. hep-ex/0311058, Nov 2003, comments: 5 pages LaTeX, 8 figures, presented at the 8th ICATPP conference on Astroparticle, Particle, Space Physics, Detectors and

Medical Physics Applications, Como, Italy, 6-10 October 2003, proceedings to be published by World Scientific. [Online]. Available: <https://cds.cern.ch/record/686973>

- [31] A. Experiment, “Cut-away view of the ATLAS calorimeter system.” 2008. [Online]. Available: <https://twiki.cern.ch/twiki/bin/viewauth/AtlasPublic/AtlasTechnicalPaperListOfFigures?t=1465325808>
- [32] ———, “Calorimeter,” 2016. [Online]. Available: <http://atlas.cern/discover/detector/calorimeter>
- [33] “ATLAS liquid argon calorimeter: Technical design report,” 1996.
- [34] H. Wilkens and the ATLAS LArg Collaboration, “The atlas liquid argon calorimeter: An overview,” *Journal of Physics: Conference Series*, vol. 160, no. 1, p. 012043, 2009. [Online]. Available: <http://stacks.iop.org/1742-6596/160/i=1/a=012043>
- [35] E. Rezaie, “Commissioning of the ATLAS liquid argon calorimeters,” Ph.D. dissertation, Simon Fraser U., 2008. [Online]. Available: <https://inspirehep.net/record/886690/files/Thesis-2005-Rezaie.pdf>
- [36] B. Sotto-Maior Peralva, “Calibration and Performance of the ATLAS Tile Calorimeter,” in *Proceedings, International School on High Energy Physics : Workshop on High Energy Physics in the near Future. (LISHEP 2013)*, 2013. [Online]. Available: <https://inspirehep.net/record/1231740/files/arXiv:1305.0550.pdf>
- [37] S. Palestini, “The muon spectrometer of the ATLAS experiment,” *Nuclear Physics B Proceedings Supplements*, vol. 125, pp. 337–345, Sep. 2003.
- [38] A. Experiment, “Cut-away view of the ATLAS muon system,” 2008. [Online]. Available: <https://twiki.cern.ch/twiki/bin/viewauth/AtlasPublic/AtlasTechnicalPaperListOfFigures?t=1465325808>
- [39] ———, “Muon Spectrometer,” 2016. [Online]. Available: <http://atlas.cern/discover/detector/muon-spectrometer>

- [40] “Monitored Drift Tubes Chambers for Muon Spectroscopy in ATLAS,” CERN, Geneva, Tech. Rep. ATL-MUON-94-044. ATL-M-PN-44, Jun 1994. [Online]. Available: <https://cds.cern.ch/record/685844>
- [41] “ATLAS muon spectrometer: Technical design report,” 1997.
- [42] G. Cattani and the RPC group, “The resistive plate chambers of the atlas experiment: performance studies,” *Journal of Physics: Conference Series*, vol. 280, no. 1, p. 012001, 2011. [Online]. Available: <http://stacks.iop.org/1742-6596/280/i=1/a=012001>
- [43] N. Amram *et al.*, “Position resolution and efficiency measurements with large scale Thin Gap Chambers for the super LHC,” *Nucl. Instrum. Meth.*, vol. A628, pp. 177–181, 2011.
- [44] A. Experiment, “Magnet System,” 2016. [Online]. Available: <http://atlas.cern/discover/detector/magnet-system>
- [45] T. Kawamoto, S. Vlachos, L. Pontecorvo, J. Dubbert, G. Mikenberg, P. Iengo, C. Dallapiccola, C. Amelung, L. Levinson, R. Richter, and D. Lellouch, “New Small Wheel Technical Design Report,” CERN, Geneva, Tech. Rep. CERN-LHCC-2013-006. ATLAS-TDR-020, Jun 2013, aTLAS New Small Wheel Technical Design Report. [Online]. Available: <https://cds.cern.ch/record/1552862>
- [46] B. Stelzer, “The New Small Wheel Upgrade Project of the ATLAS Experiment,” CERN, Geneva, Tech. Rep. ATL-MUON-PROC-2014-008, Oct 2014. [Online]. Available: <https://cds.cern.ch/record/1958265>
- [47] K. Ntekas and S. Leontsinis, “Performance Studies of Micromegas Chambers for the New Small Wheel Upgrade Project,” CERN, Geneva, Tech. Rep. ATL-MUON-PROC-2015-013, Nov 2015. [Online]. Available: <https://cds.cern.ch/record/2103998>
- [48] I. Roth, A. Klier, and E. Duchovni, “Testing sTGC with small angle wire edges for the ATLAS New Small Wheel Muon Detector Upgrade,” in *Proceedings, 4th International Conference on Advancements in Nuclear Instrumentation Measurement Methods and their Applications (ANIMMA 2015)*, 2015, pp. 1–6. [Online]. Available: <https://inspirehep.net/record/1374492/files/arXiv:1506.01277.pdf>

- [49] A. Zibell, “Micromegas detectors for the upgrade of the ATLAS Muon Spectrometer,” Feb 2014. [Online]. Available: <https://cds.cern.ch/record/1664515>
- [50] A. Canada, “Atlas canada.” [Online]. Available: <http://www.atlas-canada.ca/canconatlas.html>
- [51] TRIUMF, “STUDENT JOB PROGRAM Summer 2014 job posting,” March 2014. [Online]. Available: <http://admin.triumf.ca/d2w-pub/coopjob/jobd?jobno=TR14-2-21>
- [52] R. Mewaldt, “Comis rays.” [Online]. Available: [http://www.srl.caltech.edu/personnel/dick/cos\\_encyc.html](http://www.srl.caltech.edu/personnel/dick/cos_encyc.html)
- [53] C. O’Luanaigh, “Cosmic rays: particles from outer space,” Sep 2012. [Online]. Available: <http://cds.cern.ch/record/1997421>
- [54] V. S. Berezinskii, S. V. Bulanov, V. L. Ginzburg, V. A. Dogel, and V. S. Ptuskin, *The astrophysics of cosmic rays*, 1984.
- [55] K. A. Olive *et al.*, “Review of Particle Physics,” *Chin. Phys.*, vol. C38, p. 090001, 2014.
- [56] E. Technology, “EJ-200 PLASTIC SCINTILLATOR Datasheet,” 2016. [Online]. Available: <http://fcomp.ist.utl.pt/LRC.web/equipamento/EJ200-datasheet.pdf>
- [57] ———, “Light guides and acrylic plastic,” 2016. [Online]. Available: <http://eljentechnology.com/index.php/products/light-guides-and-acrylic-plastic>
- [58] CAEN, “N842 N843 User Manual,” 2011. [Online]. Available: <http://www.caen.it/csite/LibrarySearch.jsp>
- [59] Fermilab, “NIM Model 623B Octal Updating Discriminator,” Sep 2011. [Online]. Available: <http://www.fnal.gov/projects/ckm/jlab/623b-spec.htm>
- [60] K. Carnes, “Constant Fraction Discriminators,” 2003. [Online]. Available: <https://jrm.phys.ksu.edu/Resource/Pubs/CFD/CFD.html>
- [61] Dschwen, “Comparison of threshold triggering (left) and constant fraction triggering (right),” 2006. [Online]. Available: [https://en.wikipedia.org/wiki/Constant\\_fraction\\_discriminator#/media/File:Constant\\_fraction\\_1.svg](https://en.wikipedia.org/wiki/Constant_fraction_discriminator#/media/File:Constant_fraction_1.svg)

- [62] CAEN, “N405 User Manual,” 2011. [Online]. Available: <http://www.caen.it/csite/LibrarySearch.jsp>
- [63] H. P. K.K, “R329-02Photomultiplier tube data sheet,” 2016. [Online]. Available: <https://www.hamamatsu.com/jp/en/R329-02.html>
- [64] M. Paterno, “Calculating efficiencies and their uncertainties,” 2004, fERMILAB-TM-2286-CD.
- [65] L. Adamek, “The time difference measurment of the trigger system,” Tech. Rep., July 2015.
- [66] G. F. Knoll, *Radiation detection and measurement; 4th ed.* New York, NY: Wiley, 2010. [Online]. Available: <https://cds.cern.ch/record/1300754>
- [67] K. Takenaga, Y. Arakawa, S. Tanigawa, N. Guan, S. Matsuo, K. Saitoh, and M. Koshiba, “Reduction of crosstalk by trench-assisted multi-core fiber,” in *Optical Fiber Communication Conference/National Fiber Optic Engineers Conference 2011*. Optical Society of America, 2011. [Online]. Available: <http://www.osapublishing.org/abstract.cfm?URI=OFC-2011-OWJ4>
- [68] K. D. Ianakiev, B. S. Alexandrov, P. B. Littlewood, and M. C. Browne, “Temperature behavior of NaI(Tl) scintillation detectors,” *Nuclear Instruments and Methods in Physics Research A*, vol. 607, pp. 432–438, Aug. 2009.